

Novel Perspectives in Non-Invasive Diagnosis of Ailments through Analysis of Mechanical Wave Motion

By

HARISH PALNITKAR

M. Tech., Indian Institute of Technology Madras, 2011

THESIS

Submitted in partial fulfilment of the requirements for the degree of
Doctor of Philosophy in Mechanical Engineering in the Graduate College of
University of Illinois at Chicago, 2021

Chicago, Illinois

Defense committee:

Professor Thomas J. Royston, Chair and Advisor, *Bioengineering and Mechanical Engineering*

Professor Dieter Klatt, Co-advisor, *Bioengineering*

Professor Richard Magin, *Bioengineering and Neuroscience*

Professor Michael Brown, *Mechanical Engineering*

Professor Craig Foster, External member, *Civil and Materials Engineering*

Dedicated to my parents Dr. Ravindra Palnitkar and Mrs. Aparna Palnitkar

Acknowledgements

At the outset, I would like to sincerely thank my Grandparents, whose keen interest in science and an inclination towards academia helped shaped my dream of pursuing a career in mechanical engineering. I would like to thank my Father, Dr. Ravindra Palnitkar for sowing the seeds of interest, curiosity and passion towards railway locomotives of the Indian Railways during our outings each evening in my childhood, which motivated me to pursue a career in Mechanical Engineering. It is his discipline, ardent support and motivation that helped me realize my dream of becoming a mechanical engineer. I would like to convey Special Thanks to my Mother Mrs. Aparna Palnitkar for always being so kind and loving, and for ensuring that all the necessities in life were taken care of without having me to worry about them, so that I could focus on my studies and lead a carefree childhood sans worries and insecurities. Thank you to my brother Jai for being a source of support, wit-and-wisdom and energy throughout my life.

It would not be an exaggeration to say that my doctoral research and this thesis would not be possible without the continual support, motivation and mentoring of my advisor Professor Thomas J. Royston. Over the past 6 years, Professor Royston has not only helped me develop my scientific temperament and my approach to problem-solving, he has also helped nurture my interpersonal and communication skills through his unique, warm and friendly style of leadership. One key change in my life that I completely credit with due respect to Professor Royston is developing patience (a key attribute for research), coupled with my positive transformation from earlier apprehensive mannerism to my current peaceful and confident demeanor. Over these 6 years, through the numerous interactions and one-on-one meetings with him I have learnt the importance of being poised while at the same time not losing the sight of my goal. Thank you for being the primary source of motivation and for bringing such a positive change in my personal and

professional life. During these 6 years, coming to lab every morning in order to perform research has been a pleasant and memorable experience to me owing to the friendly and peaceful research environment nurtured by him. Of course, some of my best memories have been our lab group meetings which were always so friendly, and open, and our research trip to Gainesville, Florida for the RF-coil training workshop. Thank you, Professor Royston, for facilitating a positive, friendly and a secure learning environment that has fostered creativity through informal interaction between lab members.

Simultaneously, I would like to thank my co-advisor Professor Klatt, who not only taught me the science and mathematics involving Magnetic Resonance Elastography (MRE), but he also inspired me to be meticulous and accurate in my research. Over the last 3 years, Professor Klatt facilitated my learning and the development of my MRE experimentation skills, as well as my technical writing skills, by teaching me how to answer various types of questions (both easy, and the not-so-easy ones), raised by the reviewers of a journal. Professor Klatt is one of the friendly and considerate teachers I have ever had. I shall always fondly remember the pre-covid days of having a nice conversation over a cup of coffee at his office while having a discussion about my research.

I would like to cordially Thank the members of my Defense Committee, Professor Richard Magin (who I shall always admire as my best teacher, so full of energy and hands-on examples and experiences related to Biomedical Imaging. Thank you so much for being a great teacher and Professor of Biomedical Imaging); Professor Foster for teaching me Finite Element Analysis using his unique style of teaching interactively, through real-life assignments, iClicker quizzes and application oriented projects; and Professor Brown for kindly teaching me how to be a good, patient Teaching Assistant to undergraduate students.

I would like to profusely thank my good friend and colleague Dr. Rolf Reiter without whose help and continual support, my MRE experiments would not be possible. I shall always remember the good days of meeting him in the lab to perform dissection of various biological tissues in order to study their anatomical structure and prepare them for MRE experimentation, and our numerous trips to our favorite Peoria Schlachthof (Slaughterhouse) to procure biological samples (special thanks to the floor manager Mr. Jerry who always ensured that our samples were neatly packaged and ready for pick-up, so as to minimize our waiting time inside the slaughterhouse).

Special thanks to my good friends and former lab mates Dr. Zoujun Dai, Dr. Ying Peng and Dr. Brian Henry, for always being so friendly, easy-to-approach and for helping me learn Comsol, Matlab and the scanning laser doppler vibrometer (SLDV) during my initial years of research related to the Audible Human Project (AHP). I shall always cherish and remember the informal afternoon conversations with Dr. Dai about research and non-research related aspects of life.

I would like to thank my labmates Dr. Shreyan Majumdar, Joseph Crutison, Shujun Lin and my former labmate Dr. Steven Kearney for helping me learn and implement image and data processing techniques necessary for our research related to Elastography. I would also like to extend my gratitude to my labmates Joshua Smejkal, Lorenzo Aliboni, Andrea Carmignotto, Luca Leoni, Aime Luna, Melika Salehabadi and Federica Dibbernardo for being so nice and supportive at all times.

I would like to extend my Thankfulness and sincere appreciation to the staff of Bioengineering (especially to Ms. Jessica Mejia and Mr. Lukasz Zientara) and the staff of Mechanical Engineering (Ms. Veronica Rodriguez and Mr. Alan Wilmington) for always being so friendly and resourceful, and for making the life of international students a lot easier.

I would like to sincerely Thank my bestfriends at UIC: Amirreza, Adit and Abhilash, for having my back, for supporting me emotionally during each stage of my research and personal life, and for helping me by providing an environment of home-away-from-home. I would especially like to thank Amirreza for helping me during the difficult months of shelter-at-home in 2020, and during my busy days of experimentation. Thank you for teaching me the importance of patience and calmness in life. I would also like to Thank my bestfriends in India (Dileep and Sunil), for their best wishes and moral support althroughout my research.

Last but not the least, financial assistance and support of NIH grant R01 AR071162 and NSF grant 1852691 is kindly acknowledged.

Contribution of Authors

Chapter 2 is based on our published work [1] of which I am the primary author. Co-authors Dr. Ying Peng and Dr. Brian M. Henry taught me Comsol Multiphysics and helped me in the computational modeling of sound propagation in healthy and diseased lung parenchyma. Co-author Zoujun Dai and PI Prof. Thomas J. Royston mentored and advised me on the constitutive equations of mechanical wave propagation and in interpreting data collected by former students during human insonification experiments. Prof. Thomas J. Royston mentored me in writing the manuscript and is my thesis advisor.

Chapter 3 is based on our prior work [2] published in 2019 of which I am the primary author. Co-authors Dr. Rolf Reiter and Dr. Shreyan Majumdar helped me in performing experimentation using Agilent 9.4 T MRI system, and in preparing ex vivo tissue samples for MRE experimentation. The vibration set-up (holder) was originally designed by Dr. Shreyan Majumdar and Dr. Steven Kearney. Co-Authors Ms. Margaret Hammersley, Dr. Phillip Lewis and Dr. Ramille Shah (PI) provided us with 3D printed fiber phantoms carefully manufactured to meet our requirements of fiber dimensions. PIs Prof. Thomas J. Royston and Prof. Dieter Klatt mentored me in writing the manuscript and in presenting my results in a coherent manner. Prof. Dieter Klatt taught and mentored me on MRE data processing and in the development of the 1-Norm technique.

Chapter 4 is based on our recent work which is yet to be published, of which I am the primary author. Co-authors Dr. Rolf Reiter and Dr. Shreyan Majumdar helped me by allowing me to observe their experimentation on excised biological tissues, and subsequently by sharing the raw unprocessed data of their experiments on excised biological tissues and ex vivo mouse brains (control and 5xFAD species). Co-author Joseph Crutison helped me with statistical analysis of the

experimental data (analysis of variance). Co-author Shujun Lin helped me in phase unwrapping of the phase images obtained for the excised porcine kidney samples. PIs Prof. Thomas J. Royston and Prof. Dieter Klatt mentored me in writing the manuscript and in presenting my results. Prof. Dieter Klatt mentored me on MRE data processing and in fine-tuning the concept of 1-Norm.

TABLE OF CONTENTS

<u>CHAPTER</u>	<u>PAGE</u>
1. INTRODUCTION	1
1.1 Background and Motivation.....	1
1.2 Dissertation Organization.....	3
1.3 Dissertation Aims	4
1.4 Innovation.....	6
1.5 Intellectual Merit and Broader Impacts.....	7
2. DIAGNOSTIC APPLICATIONS OF MECHANICAL WAVE PROPAGATION IN HUMAN THORAX: A COMPUTATIONAL AND EXPERIMENTAL INVESTIGATION	8
2.1 Background: Challenges involved in lung imaging	8
2.2 Literature Review	9
2.3 Objective	10
2.3.1 Rationale for the present choice of pulmonary pathologies	11
2.3.2 Notable improvements over past studies	13
2.4 Theory	13
2.4.1 Airway acoustics: Impedance	13
2.4.2 Calculation of acoustical impedance using modified Horsfield model	14
2.4.3 Parenchymal acoustics.....	15
2.4.4 Geometrical modeling of the airways.....	17
2.4.5 Lung parenchyma: material model	18
2.5 Experimentation on Healthy Human Subjects	18
2.6 Development of Computational Models	20
2.6.1 Modeling healthy human lung parenchyma	20
2.6.2 Material properties of bone and soft tissue.....	22
2.6.3 Computational modeling of Pneumothorax (PTX)	23
2.6.3.1 Material properties of healthy and PTX lung	25
2.6.3.2 Mode of excitation to investigate PTX	26
2.6.4 Computational modeling of Tumor	26
2.6.4.1 Material properties of Tumors	27

2.6.5 Computational modeling of Fibrosis	27
2.6.5.1 Material properties of lung with fibrosis	27
2.6.5.2 Mode of mechanical excitation for investigating Fibrosis: Side shear	28
2.6.6 Computational modeling of Pneumonia	29
2.7 Results and Discussion.....	30
2.7.1 Insonification experiments on healthy human subjects	30
2.7.2 Computational simulation of PTX.....	34
2.7.3 Computational simulation of Fibrosis	37
2.7.3.1 Simulation of Fibrosis using Insonification	37
2.7.3.2 Simulation of Fibrosis using Side Shear	38
2.7.4 Computational simulation of Tumor	40
2.7.5 Computational simulation of Pneumonia	41
2.8 Limitation of current study.....	43
3. 1-NORM: A NOVEL WAVEFORM ANALYSIS TECHNIQUE TO QUANTIFY THE DEGREE OF MECHANICAL INHOMOGENEITY OF VISCOELASTIC MATERIALS	45
3.1 Introduction	45
3.1.2 Literature review.....	46
3.1.3 Objective of the investigation.....	47
3.1.4 Significance of the investigation	48
3.1.5 Clinical relevance of 1-Norm	49
3.2 Theory	49
3.2.1 Wave propagation in a viscoelastic continuum	49
3.2.2 Magnetic Resonance Elastography (MRE)	51
3.2.3 Introduction to 1-Norm.....	52
3.3 Method	54
3.3.1 MRE on 3D printed fiber phantom.....	55
3.3.2 Finite element phantom model	59
3.3.3 MRE on excised porcine lumbus muscle (Agilent 9.4 T preclinical MRI system).....	62
3.3.4 MRE on excised bovine liver sample (Agilent 9.4 T preclinical MRI system)	66
3.4 Results	67
3.4.1 MRE experiments on 3D printed fiber phantom	67
3.4.2 FEA on phantoms with uniformly spaced scatterers	69
3.4.3 MRE experiments on excised porcine lumbus muscle	72

3.4.4 MRE on excised bovine liver tissue	73
3.5 Discussion	73
3.5.1 Coupled anisotropy and scattering effects.....	73
3.5.2 Interpretation of 1-Norm Variations.....	75
3.5.3 Limitations.....	77
3.5.4 Outlook	78
4. 1-NORM TO CHARACTERIZE CHANGES IN MECHANICAL INHOMOGENEITY IN FREEZE-THAWED TISSUES AND IN MOUSE BRAIN DUE TO NEURODEGENERATIVE DISEASE	81
4.1 Introduction	81
4.1.1 Hypotheses.....	81
4.1.2 Approach	82
4.1.3 Frozen Tissue Samples	82
4.1.4 Alzheimer’s Disease	83
4.1.5 Significance of the current investigation	84
4.2 Method	85
4.2.1 Experimentation set-up.....	85
4.2.2 MRE experimentation on excised porcine kidneys, liver and lumbus muscle tissues .	85
4.2.3 MRE experimentation on Control and Alzheimer’s Mouse Brain Samples	86
4.2.4 Data processing.....	87
4.3 Results	88
4.3.1 MRE experimentation on fresh and freeze-thawed excised porcine kidneys.....	88
4.3.2 MRE experimentation on fresh and freeze-thawed excised porcine liver.....	90
4.3.3 MRE experimentation on fresh and freeze-thawed excised porcine lumbus muscle ...	91
4.3.4 MRE experimentation on excised control and Alzheimer’s disease mouse model brain	93
4.4 Discussion	94
4.4.1 Influence of Freezing and Thawing on the bulk material inhomogeneity of excised tissues.....	94
4.4.2 Alzheimer’s disease and brain tissue inhomogeneity.....	96
4.4.3 1-Norm as a quantifier of tissue inhomogeneity	98
4.4.4 Correlating mechanical inhomogeneity (1-Norm) with tissue stiffness	99
4.4.5 Limitation of current study	99

5. CONCLUSION AND SCOPE FOR FUTURE WORK	101
5.1 Key achievements of the dissertation.....	101
5.2 Prospects for future research	103
APPENDIX A: Copyright clearance and permission to use all the content from our published journal article on human airway insonification (Chapter 2)	105
APPENDIX B: Comparison of results of insonification experimentation on 3 healthy human subjects versus computational simulation.....	107
APPENDIX C: Copyright clearance and permission to use all the content from our published journal article on 1-Norm (Chapter 3)	108
CITED LITERATURE	109
VITA	115

LIST OF TABLES

Table 1. Sample values of the material properties used in the computational study using finite element analysis.	26
Table 2. Compression and shear wave speeds used in the computational study of a lung with tumor.	27
Table 3. Material properties used in Finite Element Analysis	61
Table 4. Comparison of rapidness of decay of peaks on frequency spectra in terms of ratio of harmonics for:	65
Table 5. Summary of values of 1-Norm across various experiments (all computed using $n = 108$ points on the delineated contour).....	68
Table 6. MRE Experimentation Parameters for fresh and frozen kidney, liver and muscle samples.....	86
Table 7. MRE Experimentation Parameters for investigating 3 ex vivo control brains and 3 ex vivo 5xFAD Mouse Brains of AD model	87
Table 8. Variation of group-averaged values of 1-Norm as a function of mechanical frequency of excitation for excised porcine kidneys before and after freeze-thawing, with standard deviation (for $n = 3$ kidney samples) presented in parenthesis.....	89
Table 9. Variation of group-averaged values of stiffness of excised porcine kidneys as a function of mechanical frequency of excitation, before and after freeze-thawing, with standard deviation (for $n = 3$ kidney samples) presented in parenthesis.....	89
Table 10. Variation of group-averaged values of 1-Norm as a function of mechanical frequency of excitation for excised porcine liver tissue before and after freeze-thawing, with standard deviation (for $n = 3$ liver samples) presented in parenthesis.	90
Table 11. Variation of group-averaged values of stiffness of excised porcine liver tissue as a function of mechanical frequency of excitation, before and after freeze-thawing, with standard deviation (for $n = 3$ liver samples) presented in parenthesis.	91
Table 12. Variation of group-averaged values of 1-Norm as a function of mechanical frequency of excitation for excised porcine lumbus muscle sample before and after freeze-thawing, with standard deviation (for $n = 3$ muscle samples) presented in parenthesis.....	92
Table 13. Variation of group-averaged values of stiffness of excised porcine lumbus muscle sample as a function of mechanical frequency of excitation, before and after freeze-thawing, with standard deviation (for $n = 3$ muscle samples) presented in parenthesis.....	92
Table 14. Variation of group-averaged values of 1-Norm as a function of mechanical frequency of excitation for excised mouse brain (control) and 5xFAD mouse model of AD, with standard deviation (for $n = 3$ control and AD brain samples) presented in parenthesis.....	93
Table 15. Group-averaged values of stiffness (real part of complex modulus) for 3 Control Mouse Brains and 3 Mouse models of AD (5xFAD). Standard deviation values are given inside the brackets.	94

LIST OF FIGURES

Figure 1. (a) Schematic diagram of the experimental setup; (b) The grid of measurement points on the dorsal side of torso of the human subject.....	19
Figure 2. (a) Three dimensional modeling; (b) and (c): generation of finite element mesh.	21
Figure 3. Computational simulation of PTX (collapsed lung): (a) Finite element model of lungs (healthy left lung and right lung affected with PTX) and (b) 3-dimensional model of airways...	24
Figure 4. Finite element modelling of tumor.	26
Figure 5. Application of a “shear” excitation on the side of the torso to investigate fibrosis.	29
Figure 6. Computational modeling and simulation of pneumonia: (a) Three dimensional model showing the circular region on the chest surface where mechanical motion (percussion) is applied; (b) orientation of the global coordinate system, with the y-axis pointing along the direction of mechanical motion and (c) three dimensional model of the lung tissue, with the lobe highlighted in indigo color representing the condition of pneumonia.	30
Figure 7. A comparison of results of FRFs for in-vivo experiments involving 3 Human Subjects, with results presented in terms of the Average FRF (blue dashed curve) and Average Plus One Standard Deviation (green dashed curve), both compared against the FRF values obtained from finite element simulation (red dashed curve). (a,c,e): comparison of FRF (experiment versus FEA) for points #31, #47 and #52 on the left side of the dorsal side of torso (figure 1(b)); (b,d,f): comparison of FRF (experiment versus FEA) for points #31, #47, and #52 on the right side of the dorsal side of torso (Figure 1(b)).	31
Figure 8. A comparison of the lung normal surface velocity amplitude (in dB m/s per 1 Pa of input acoustic pressure) at 500 Hz for a healthy human torso, computed using (a) simulation and (b) experiment. The rectangle in (a) represents the region of interest for the same areas corresponding to the measurements performed in the experiment as shown in (b).....	33
Figure 9. Contour plots of acoustic velocity (in y-direction) shown at a cross section taken in the middle of the torso, as a function of frequency.....	35
Figure 10. Contour plots of surface velocity in absolute scale (in y-direction) at the dorsal side of the torso as a function of frequency. Note: y-direction is normal to the zx -plane, pointing outwards from the plane of the image.....	36
Figure 11. Contour plots of amplitude of displacement (in absolute scale, dB), at two frequencies of 500 Hz ((a), (b), (e), (f), (i), (j)) and 800 Hz ((c), (d), (g), (h), (k), (l)).	38
Figure 12. Contour plots of curl of displacement in z-direction (in m) showing propagation of shear waves in normal lung ((a), (c), (e)) and a lung with fibrosis ((b), (d), (f)) at frequencies of 100 Hz, 200 Hz and 300 Hz.....	39
Figure 13. Contour plots of amplitude of velocity (in y-direction), at 300 Hz, 500 Hz and 800 Hz for a healthy lung ((a), (c), (e)) and lung containing tumor ((b), (d), (f)).	41
Figure 14. Results of Finite Element Simulation: (a) – (d): Plots of y-directional velocity amplitude (in dB scale) shown on the posterior surface of the torso; (e): selection of a cross-sectional slice at the middle of the torso to enable visualization of mechanical wave motion inside the chest; (f) – (i): plots of velocity amplitude in y-direction for the slice chosen at the middle of the chest region. At higher mechanical frequencies, the preferred path of propagation of mechanical waves is through the infected lung (pneumonia), as is evident from the regions of	

“zero wave motion” at the posterior of the torso region that is behind the healthy lung (contours in dark blue color, as highlighted in (i)).	42
Figure 15. Schematic diagram depicting the technique of 1-Norm being applied to: Case 1: A homogeneous isotropic medium; Case 2: A homogeneous isotropic medium with a center mismatch; Case 3: A homogeneous anisotropic medium; Case 4: Wavefront from MRE experimental data on 3D printed anisotropic fiber phantom and Case 5: Quadratic wavefront from MRE experiments on ex vivo porcine lumbus muscle.	52
Figure 16. The 3-D printed anisotropic fiber phantom (placed inside a borosilicate glass test tube) and surrounded by gel medium b. Microstructure of the 3-D printed anisotropic fiber phantom.	56
Figure 17. Schematic diagram of the experimental set-up used in Magnetic Resonance Elastography experiments on the 3D printed fiber phantom (representational diagram; not to scale) b. Picture of the piezoelectric actuator (on left) and test-tube sample (on the right) c. Orientation of the coordinate system	57
Figure 18. Finite Element Analysis (a) Three-dimensional modeling and orientation of spherical inclusions; (b) FE model with interstitial gap of $d = 2.5$ mm between neighboring spherical inclusions; (c) and (d): FE models used in additional investigations using reduced distance ($d = 1.65$ mm and $d = 1.25$ mm) between neighboring spherical inclusions	60
Figure 19. Dimensions of the ex-vivo porcine lumbus muscle used in Magnetic Resonance Elastography experiments. Muscle fibers are oriented in the direction perpendicular to the plane of the image, which is also the direction of mechanical vibration.	62
Figure 20. Apparatus used in MRE experimentation of an ex-vivo Porcine Lumbus muscle. (a) Cylindrical excitation cup used as sample holder with an outer diameter of 6.4 cm and a height of 8.5 cm; (b) connecting rod made of Delrin, with a diameter of 1 cm and a length of 6.2 cm; (c) Pre-loaded piezo electric actuator and (d) inertial coupling of the rear end of the piezo to the supporting structure	63
Figure 21. A comparison of (a) elliptical and (b) square shaped wave fronts along with the corresponding frequency spectra for (c) elliptical wavefront and (d) square wavefront. Both elliptical and square wavefronts exhibit rapidly decaying peaks at lower harmonics.	65
Figure 22. MRE on excised bovine liver sample. (A) Sample preparation: the bovine liver tissue was surrounded by 10% w/v water based gelatin medium in order to enable propagation of mechanical shear waves from the excitation cup into the sample. (B) Sample holder and excitation cup and (C) Dimensions of the liver sample used in the MRE study.	66
Figure 23. Results of MRE experiments on 3D printed fiber phantom.	67
Figure 24. Contours of real part of shear wave displacement profiles for FE simulation. Snapshots of the shear wave at frequencies of 1 kHz (a-d), 2 kHz (e-h), 3 kHz (i-l), 4 kHz (m-p) and 5 kHz (q-t) for a homogeneous 5% w/v water based gelatin finite element phantom (first column) versus inhomogeneous finite element phantoms (columns 2 through 4) containing uniformly distributed spherical inclusions of spacing d (2 nd column: $d=2.5$ mm; 3 rd column: $d=1.65$ mm; 4 th column: $d=1.25$ mm) that cause scattering of wave fronts.	70
Figure 25. Frequency spectra for delineated contours of zero shear wave displacement in Finite Element Simulations: Frequency spectra obtained using spatial Fourier Transform of the delineated wave fronts at mechanical frequencies of 1 kHz (a-d), 2 kHz (e-h), 3 kHz (i-l), 4 kHz	

(m-p) and 5 kHz (q-t). From Left: Column 1: Wave spectra for a homogeneous 5% w/v water-based gelatin Finite Element phantom; Columns 2 through 4: Wave spectra for Finite Element phantoms containing spherical inclusions (of diameter 0.5 mm) with a spacing of $d = 2.5$ mm, $d = 1.65$ mm and $d = 1.25$ mm, respectively.	71
Figure 26. Results of MRE experimentation on excised porcine lumbus muscle sample. (a-d) Plots of real part of complex-valued shear wave displacement along with delineated profile of zero displacement (highlighted in white color) observed in the MRE experiments on ex-vivo porcine lumbus muscle at frequencies of a) 500 Hz, b) 600 Hz, c) 800 Hz and d) 1000 Hz. (e-h) The corresponding frequency spectra for the delineated profile of zero wave displacement at frequencies of e) 500 Hz, f) 600 Hz, g) 800 Hz and h) 1000 Hz, along with the 1-Norm values. Note: The direction of muscle fibers is normal to the plane of the image.	72
Figure 27. Results of MRE experimentation on excised bovine liver tissue. (a-b) Shear wave images and zero displacement contour lines (highlighted in white color) observed in the MRE experiments on ex-vivo porcine lumbus muscle at frequencies of a) 200 Hz and b) 300 Hz. (c-d) The corresponding frequency spectra for the surrounding medium (gel) at frequencies of c) 200Hz and d) 300 Hz. (e-f) Frequency spectra for the delineated contour of zero displacement for the liver at e) 200 Hz and f) 300 Hz.....	73
Figure 28. Snapshots of shear waves propagating in the 3D printed inhomogeneous fiber phantom for varying mechanical phases at frequencies of (a) through (d): 2000 Hz; (e) through (h): 3000 Hz and (i) through (l): 5000 Hz. The wave fronts exhibit both elongation (due to directional anisotropy) accompanied with scattering (at fiber intersections) due to inhomogeneities. Fibers are highlighted in white color.....	74
Figure 29. Plot of variation of 1-Norm with respect to the ratio (λ/d) , where λ is the wavelength of propagating shear waves and d is the spacing between neighboring spherical inclusions. (b) Plot of variation of 1-Norm with respect to the spacing (d) between the neighboring spherical inclusions, at frequencies of 1 kHz, 2 kHz, 3 kHz, 4 kHz and 5 kHz.....	76
Figure 30. Contours of shear wave displacement, along with delineated profile of equal (zero) displacement (white color), for freshly excised kidney sample no. 1 (a-d) and for the same kidney sample after freezing and thawing (e-h).	89
Figure 31. Contours of shear wave displacement, along with delineated profile of equal (zero) displacement (white color), for freshly excised porcine liver sample (a-d) and for the same sample after freezing and thawing (e-h).	90
Figure 32. Contours of shear wave displacement, along with delineated profile of equal (zero) displacement (white color), for freshly excised (a-d) porcine lumbus muscle sample and for the same sample after freezing and thawing (e-h).	92
Figure 33. Contours of real part of complex displacement (sample no. 2) obtained after MRE experimentation on excised control (a-c) and Alzheimer's disease (d-f) mouse brains. A total of 3 samples were analyzed.....	93
Figure 34. Group-averaged values of 1-Norm and stiffness as a function of mechanical frequency for porcine kidneys (a, b), porcine liver (c, d) and porcine lumbus muscle (e, f) under fresh condition (green) versus after freezing and thawing (red). The error bars indicate the standard deviation over the 3 samples in each group.	95

Figure 35. Group-averaged values of (a) 1-Norm and (b) stiffness as a function of mechanical frequency of excitation for 3 Control brains (green) and 3 5xFAD mouse brains with Alzheimer’s disease (red). The error bars indicate the standard deviation over the 3 samples in each group.	97
Figure 36. A comparison of group averaged 1-Norm values for ex vivo porcine kidneys (green), porcine liver (cyan) and porcine lumbus muscle (red) (a) in fresh condition and (b) after freezing and thawing.	99
Figure 37. Plot showing the variation of frequency response function (FRF) with mechanical frequency for the three healthy human subjects (dashed curves) versus computational simulation (red curve).	107

LIST OF ABBREVIATIONS

AD	Alzheimer's disease
FRF	Frequency Response Function
MEG	Motion Encoding Gradient
MRE	Magnetic Resonance Elastography
MRI	Magnetic Resonance Imaging
PSC	Primary Sclerosing Cholangitis
ROI	Region of Interest
SLDV	Scanning Laser Doppler Vibrometer
SNR	Signal to Noise Ratio
TE	Echo Time
TR	Repetition Time

SUMMARY

The central theme of this dissertation is the observation that mechanical waves propagate and scatter at different velocities in biological tissues due to a difference in local material properties (such as viscosity and stiffness), due to the presence of inhomogeneities such as a blood vessel, an axon or a muscle filament. These scattered waves contain information about the characteristic stiffness, viscosity and the mechanical property inhomogeneity of the tissues through which they propagate; this information can aid in non-invasive diagnosis of disease and injury using novel quantitative techniques such as *Insonification*, *Percussion* and *I-Norm* using Magnetic Resonance Elastography (MRE). The goal of the current work is to lay a foundation for non-invasive, wave-propagation based diagnosis of disease and injury in human organs, by demonstrating the validity and relevance of these aforementioned techniques to be able to detect and quantify the influence of a particular disease/ pathology on biological tissues. Chapter 2 encompasses the development and validation of computational model (in silico) of healthy human lung parenchyma using insonification (generation and transmission of controlled mechanical waves into the human lungs through application of pressure pulse at the trachea) and validating this computational model through performing experiments on healthy human subjects. This experimentally validated comprehensive computational model is then extended to simulate mechanical wave propagation in the airways, parenchyma, and chest wall under normal and pathological conditions that create distributed structural changes (e.g., pneumothoraces) and diffuse material changes (e.g., fibrosis), as well as a localized structural and material changes as may be seen with a neoplasm/ tumor. The computational model predictions of a frequency-dependent decreased sound transmission due to PTX were consistent with experimental measurements reported in previous work. Predictions for the case of fibrosis show that while shear wave motion is altered, changes to compression wave

propagation are negligible, and thus insonification, which primarily drives compression waves, is not ideal to detect the presence of fibrosis. Results from the numerical simulation of a tumor show an increase in the wavelength of propagating waves in the immediate vicinity of the tumor region.

Chapter 2 then focuses on the extension of a comprehensive computational model of mechanical wave motion in healthy human lung parenchyma, developed and experimentally validated by previous members of our research group using percussion, which involves application of mechanical vibration at the sternum to induce wave motion, and the measurements of surface velocity are performed by a scanning laser Doppler vibrometer (SLDV) or a digital stethoscope on the torso posterior. The current work extends this in-silico model to simulate the pathological condition of pneumonia. It is demonstrated that at higher mechanical frequencies of excitation (300-600 Hz) the path of mechanical wave propagation is primarily through the lobe (region) of the lung affected by pneumonia, which is observed in the form of an increased amplitude of wave motion on posterior surface of torso immediately behind the diseased lung. This finding has inspired the design and development of *Tabla*, a novel, compact and easy to use device that uses percussion to induce mechanical waves into human lung parenchyma, in order to aid in non-invasive, early-stage diagnosis of pneumonia using a digital stethoscope placed at the torso posterior, enabling a wider access to healthcare for individuals living in remote global locations without the necessity of complex medical examinations such as x-ray computed tomography (CT).

Of particular emphasis is the fact that the current work utilizes finite element analysis (FEA) to materialize unique “live visualizations” of propagation of mechanical waves in a cross-sectional slice taken along the chest surface, such a visualization would not have been possible in conventional medical examinations using a stethoscope or CT.

The dissertation then dwells on the development, testing and experimental validation of a novel technique, called the *1-Norm*, which is a novel waveform analysis technique that can be used to analyze contours of mechanical wave displacement. In this dissertation, the validity and relevance of the 1-Norm technique is demonstrated on data obtained from Magnetic Resonance Elastography (MRE) experiments. The technique of MRE involves 3 steps: excite → measure → compute. To elaborate, (i) firstly, mechanical wave motion is applied to the biological tissue of interest. This can be done in-vivo using a pillow-like actuator placed in contact with the desired region on the body of the human/ animal subject, or it can be done on excised biological tissues placed inside test tubes, using geometric-focusing technique [3] to generate concentric wavefronts as in this dissertation; (ii) in the second step, imaging of time-resolved snapshots of mechanical wave motion is performed using MRI (the mechanical motion is encoded into the phase component of the complex-valued wave displacement); (iii) finally, in the third step, inversion of the wave equation is performed to determine the stiffness of the imaged tissue by incorporating the boundary conditions of the applied mechanical vibration. This technique is known as inversion (as derived from “inverse problem”) as this is opposite to the conventional approach (also known as “forward problem” in which the mechanical properties of the tissue/ specimen are already known from rheology, and the wave equation is used to compute the displacement field resulting from an applied mechanical excitation). The inversion process represents an ill-posed problem and poses a challenge for the demarcation of tissue boundaries in heterogeneous tissues. Therefore, the current investigation proposes 1-Norm alternative MRE-based biomarker to stiffness, which relies on ill-posed wave inversion.

As a first step, 3D printed fiber phantom with a controlled and pre-determined stiffness and fiber-spacing is used to investigate the effect of fiber spacing on the scattering and elongation of

mechanical wavefronts. This is followed by computational analysis (using FEA) to model finite element phantoms containing spherical inclusions (scatterers) instead of crisscrossing fibers, to de-couple the effects of anisotropy from those of inhomogeneity, and to better understand the influence of geometrical shape of the specimen on the values of 1-Norm. It is shown using computational modeling that the effects of anisotropy and shape (geometry), as well as center mismatch fall on the lower harmonics (up to 6). 1-Norm is then defined as the summation of absolute values of harmonics from no. 7 and higher, so as to only include contributions of inhomogeneities. This is followed by a demonstration of the validity and relevance of the 1-Norm technique to be able to quantify changes in the stiffness and mechanical homogeneity due to freezing and thawing of biological tissues. It is observed that freezing and thawing leads to a reduction in the stiffness and in the degree of mechanical property inhomogeneity of biological tissues. The results are validated by comparison to a prior work by other research groups who have reported a reduction in tissue stiffness as a result of freezing and thawing. The next part of the dissertation demonstrates the validity and relevance of the 1-Norm technique to be able to quantify the changes in the brain tissue inhomogeneity of a mouse brain due to the presence of neurodegenerative disease (Alzheimer's disease). Our results show an increase in the degree of brain mechanical inhomogeneity in 5xFAD species female mouse model, along with a reduction in the overall brain stiffness (which is in line with the findings of research published by other groups). This preliminary investigation on mouse brain proves the capability of 1-Norm to be able to non-invasively quantify the degree of mechanical inhomogeneity of brain due to AD, while at the same time proving to be a prospective alternative to the traditional wave inversion techniques (computation of stiffness) which are ill-posed. It is concluded that further work, including investigation of additional number of mouse brains, as well as histopathology are needed to shed

light on the microscale causes of mechanical property inhomogenization in neurodegenerative disease. In conclusion, the current work lays a computational and experimental foundation by extending the applications of two already existing techniques (insonification and percussion) and by developing a novel waveform analysis technique of *I-Norm*, which has the potential to be developed as a biomarker for non-invasive detection of disease and injury that lead to heterogeneous changes in tissue mechanical properties such as Alzheimer's disease and primary sclerosing cholangitis (PSC) of the liver.

1. INTRODUCTION

1.1 Background and Motivation

Trying to diagnose disease or injury by how it changes mechanical stiffness of biological tissue – measured directly via palpation or indirectly by measuring changes in mechanical wave motion via auscultation or visualization – has been practiced for centuries. Although these non-invasive means as practiced are often the first step in a diagnostic strategy, they are limited due to subjective inter-user variability coupled with non-availability of quantitative assessment metrics. The current work aims to address these limitations through the development and/or advancement of three techniques: insonification, percussion, and 1-Norm. In our study the first two are applied to the pulmonary system, and the latter to other soft tissue organs or regions in the body.

Insonification [4] and Percussion [5] are two techniques which have been developed and validated on porcine lung parenchyma by investigators of our research group in the past. This included the development of three dimensional models followed by computational simulation using FEA [6] of experimentally validated patient specific computer models of the healthy human torso, including modeling of the airways [7]. The present study [1] suitably modified these computational models to simulate the conditions of four pulmonary disease conditions, namely PTX (collapsed lung), fibrosis, tumor and pneumonia. Each of these pathologies has a substantially different effect on the sound transmission inside the lungs and chest cavity. For example, PTX involves an alteration in lung parenchymal geometry and density, as well as the introduction of trapped air between the parenchyma and chest wall. This should have a substantial effect on sound transmission. Fibrosis results in a distributed change in shear viscoelastic properties in the parenchyma with no significant change in geometry. A tumor results in a localized change in both tissue shear

viscoelastic properties and density. Pneumonia involves a partial or complete filling of the airways in the lobe/s of a lung with fluid, known as pleural effusion. The presence of this fluid affects the propagation of mechanical waves leading to the diseased lung having a higher amplitude of wave motion than the normal lung at higher mechanical frequencies.

Soft biological tissues such as the skeletal muscle and brain white matter can be inhomogeneous and anisotropic due to the presence of fibers. The present work proposes 1-Norm [2] as a novel quantitative parameter that can be used to determine the influence of inhomogeneities (such as a local tumor) on the nature of propagation of mechanical waves inside biological tissue. 1-Norm also serves as an alternative MRE-based biomarker to stiffness, which relies on ill-posed wave inversion. As a first step to prove the capability of 1-Norm to be able to visually distinguish homogeneous medium from an inhomogeneous medium, the investigators used a 3D printed fiber phantom having a pre-determined distribution (spacing) of fibers. An application of the 1-Norm technique to the mechanical wave fronts generated within such an anisotropic fiber phantom reveals a combination of anisotropy and inhomogeneity. The investigators therefore use FEA to model idealized phantoms containing uniformly distributed spherical inclusions (that act as inhomogeneities), without the added complexity of fibers (anisotropy). This essentially shows how to “de-couple” the effects of anisotropy from those of inhomogeneity, thereby leading to an assessment of behavior of mechanical waves purely due to the presence of inhomogeneities. A correlation is then established between the values of 1-Norm derived from the wave front geometry, and the spacing (d) between neighboring spherical inclusions. Smaller values of 1-Norm indicate less wave scattering, indicating that the material is less inhomogeneous. This is followed by the application of 1-Norm technique on various real-life scenarios, for instance, to understand the effect of freezing and thawing on the mechanical inhomogeneity of excised biological tissues

(porcine liver, porcine kidneys and porcine lumbus muscle); and to investigate the influence of neurodegenerative disorder on the mechanical brain inhomogeneity in a mouse model (5xFAD species). In all of these cases, 1-Norm is successfully able to distinguish and numerically quantify the degree of mechanical inhomogeneity of the biological tissue under consideration. In the future, the 1-Norm may serve as a diagnostic marker for diseases that involve a change in the degree of mechanical inhomogeneity in biological tissues, such as Primary Sclerosing Cholangitis.

1.2 Dissertation Organization

The organization and the fulfilment of goals of this thesis is guided through the identification of four specific aims as listed below:

1. Development of a comprehensive, experimentally validated model of sound propagation in healthy and diseased human parenchyma using airway insonification.
2. A computational investigation into the nature of mechanical wave propagation inside a human lung affected by pneumonia, using the technique of percussion.
3. Development of a technique (1-Norm) to visually discern and numerically quantify the scattering effects of inhomogeneities on the scattering of mechanical waves using MRE and FEA.
4. Demonstration of validity and relevance of the technique of 1-Norm on excised biological tissues.

Experimentation as well as computational modeling (using FEA) shall be used to address these specific aims.

1.3 Dissertation Aims

Specific Aim 1: Develop a comprehensive, experimentally validated model of sound propagation in healthy and diseased human parenchyma using airway insonification.

Hypothesis 1: Presence of pulmonary ailments and injuries lead to a measurable change in the sound transmission inside the lung parenchyma and airways, leading to a different amplitude of measured signal (velocity) at the surface of the chest wall or torso. The current work builds upon a prior work developed by the research group that synthesized and experimentally validated a comprehensive model of sound propagation inside human thorax using airway insonification [1, 5].

Specific Aim 2: Computationally investigate the nature of mechanical wave propagation inside a human lung affected by pneumonia, using the technique of percussion.

Hypothesis 2: The pathological case of pneumonia involves filling up of one or more lobes of the lung with pleural fluid. Based on a pre-test using FEA [4], it was observed that the presence of such a fluid leads to a change in the acoustic impedance mismatch between the soft biological tissue of the lung and the surrounding chest cavity, thereby leading to a greater sound intensity at higher mechanical frequencies. Therefore, it is hypothesized that when a mechanical vibration is applied at the sternum, the lung lobe affected by pneumonia would exhibit a measurable difference in the amplitude of propagating mechanical wave due to the presence of the highly viscous fluid (purulent material), which can then be measured at the back of the torso using a digital stethoscope, leading to a quicker and cost effective way of diagnosing the disease while still at an early stage.

Specific Aim 3: Develop a technique (1-Norm) to visually discern and numerically quantify the scattering effects of inhomogeneities on the scattering of mechanical waves using magnetic resonance elastography (MRE) and FEA.

Hypothesis 3: It is observed that the presence of inhomogeneities in biological tissue causes a change in the path (scattering) of mechanical waves. Therefore, a technique based on a spatial Fourier transformation, that measures the variation of the scattered wave front from that of an idealized wave front is proposed [2] in order to quantify the effect of inhomogeneities on the propagation of mechanical waves. In the future, the 1-Norm technique may have the potential to be used as a novel biomarker to aid in non-invasive diagnosis of diseases such as neurodegenerative disorders (AD), localized tumor as well as injuries in soft biological tissues such as the brain, the liver and skeletal muscle.

Specific Aim 4: Demonstrate the validity and relevance of the technique of 1-Norm on biological tissues.

Hypothesis 4: Soft biological tissues such as skeletal muscle and brain white matter can be inhomogeneous as well as anisotropic. The robustness of the technique of 1-Norm is demonstrated in a hands-on application involving fresh and freeze-thawed tissue samples (namely, porcine kidneys, porcine liver and porcine lumbar muscle). Also, the 1-Norm technique is used to identify the degree of mechanical inhomogeneity of the mouse brain (5xFAD female mice) a widely used animal model for Alzheimer's disease (AD). The 1-Norm technique was able to identify a reduction in the mechanical inhomogeneity of the biological tissues due to freezing and thawing, and an increase in the mechanical inhomogeneity of the brain tissue due to AD.

1.4 Innovation

The current work represents a step forward towards non-invasive diagnosis and assessment of pulmonary ailments as well as neurodegenerative disorders (such as AD), which has been the primary motivation of research for our group. Utilizing FEA not only enables a non-invasive, subject-specific assessment and a quantitative comparison of wave propagation in healthy versus diseased tissues, but also enables a unique visualization of mechanical wave propagation along a cross-section of the chest/ torso that are impossible to obtain using conventional imaging modalities such as ultrasound, computed tomography or magnetic resonance imaging. Such visualizations, in conjunction with the use of non-invasive techniques such as MRE and Ultrasound Elastography (USE) may then be used to generate cross-section “maps” of tissue stiffness. These maps could potentially be used as a first step in the diagnosis, localization and staging of disease and/ or injury. The technique of 1-Norm, developed and experimentally validated as a part of this dissertation, provides a unique method of visualization and quantification of mechanical wave scattering phenomenon in biological tissues due to the presence of inclusions (or inhomogeneities). We were able to successfully demonstrate the capability of 1-Norm in being able to numerically quantify a reduction in tissue inhomogeneity due to freezing and thawing, and an increase in brain tissue inhomogeneity due to the presence of neurodegenerative disease (AD) in 5xFAD female mice. In the future, such a quantitative parameter could potentially serve as a biomarker for detecting disease and injury in soft biological tissues such as the skeletal muscle, the brain and the liver. At the same time, 1-Norm has the potential to serve as a more accurate alternate biomarker to the traditional wave inversion techniques (to compute tissue stiffness), which are ill-posed.

1.5 Intellectual Merit and Broader Impacts

The techniques of *insonification* and *percussion*, as well as the mechanical wave-front analysis technique of *1-Norm* [2], provide a means to visually assess and numerically quantify the effect of change in tissue stiffness and geometry on the nature of propagation of mechanical waves, which could potentially be used in conjunction with “stiffness maps” generated from MRE/ USE as a first step towards non-invasive diagnosis and staging of disease and injury. The computational models developed in this study could potentially then be used in conjunction with stiffness maps obtained from MRE, which could aid in non-invasive diagnosis, localization and staging of disease and injury. The technique of 1-Norm, in the current stage of development, holds a potential to become a non-invasive diagnosis tool that could aid in detection of musculoskeletal damage and brain disease/ injury based on the scattering phenomenon of mechanical waves due to the presence of an inhomogeneity/ obstruction such as a localized tumor or an injured/ discontinuous tissue.

2. DIAGNOSTIC APPLICATIONS OF MECHANICAL WAVE PROPAGATION IN HUMAN THORAX: A COMPUTATIONAL AND EXPERIMENTAL INVESTIGATION

Note: This chapter includes my work [1] which was originally published in the journal *Medical and Biological Engineering and Computing* (Springer Publication). Text, figures and results have been used from this journal article after obtaining a permission from the publisher (Appendix A).

2.1 Background: Challenges involved in lung imaging

The lungs are comprised of soft tissue, airways, alveoli and vasculature structures, acoustically behaving as a poroviscoelastic material over a broad frequency range [8]. Due to this fine-structure heterogeneity, conventional imaging modalities such as magnetic resonance imaging (MRI), ultrasound (US) and X-ray computed tomography (CT) have limited resolution to detect and quantify changes in the anatomy and properties in vivo that may be indicative of many pulmonary pathologies, including subtle fibrosis, inflammation, tumors, pneumonia and PTX [9]. For instance, US is limited to detecting anomalies on the periphery of the lung due to the acoustic impedance mismatch between the lung parenchyma and chest wall. CT has the disadvantage of ionizing radiation risk, while both CT and MRI are costly and provide limited soft tissue contrast for subtle or small changes.

Nonetheless, a phase-contrast based MRI technique, known as Magnetic Resonance Elastography (MRE), which involves simultaneous application of harmonic excitation to the organ/ tissue under consideration in the presence of a radio frequency (RF) pulse (at the same frequency as that of the mechanical excitation), has demonstrated utility in the assessment of pulmonary pathology [10]–[12]. That said, MRE of the lungs is challenging since the pulmonary system is a complex poroviscoelastic structure with a significant amount of air, unlike other biological structures such

as heart [13], brain [14] and muscles [2]. A better understanding of propagation of mechanical waves inside the pulmonary structures may help improve the utility of MRE for diagnosis and monitoring of disease states. This understanding can be achieved through the development of an experimentally validated comprehensive computational model of sound propagation inside the human torso, as described in this article.

2.2 Literature Review

Prior research from this group has involved computational modeling (FEA) and experimental validation of sound propagation in human and porcine subjects using the excitation techniques of insonification [4] and percussion[5]. Insonification refers to introducing sound into the airways via an external acoustic source. This sound in turn leads to propagation of mechanical waves throughout the torso of the subject. Percussion involves introduction of mechanical wave motion on the torso surface, such as at the sternum. For both of these techniques, the resulting wave motion can be measured at the torso posterior surface by using a digital stethoscope or a scanning laser Doppler vibrometer (SLDV) [15].

Dai et al [16] performed a range of experiments on porcine lungs to determine key attributes of mechanical wave propagation in lungs, namely, compression and surface wave speed and attenuation, and used them to compare against the values predicted by an adaptation of Biot theory and an “effective medium” theory. It was concluded that the predictions made by Biot theory were closer to the experimental measurements. The same authors [17] developed an analytical technique to compute airway acoustic transmission in bifurcating airway segments and validated the technique through experimentation on a viscoelastic phantom containing a network of branching airways. Henry et al [7] extended this analytical approach to more complex and realistic airway models with an emphasis on investigating the influence of respiratory pathologies such as

pulmonary fibrosis, bronchoconstriction and pulmonary infiltrate on mechanical and geometrical properties of the complex airway tree models. Peng et al applied these modeling and analytical techniques and experimentally and computationally investigated sound transmission in the porcine thorax using airway “insonification” [4] and percussion applied at the sternum [5]. Mathematical models of sound transmission inside the pulmonary system have been also developed by subdividing the system into airways and lung parenchyma [6]. The current study, building upon this prior work, investigates the effect of different conditions – fibrosis, PTX and tumor – on sound transmission in the human thorax using airway “insonification”.

2.3 Objective

The goal of this study is two-fold: firstly, to perform in-vivo experimentation on 3 healthy human subjects using the acoustical excitation technique of airway “insonification” and perform measurements of the resulting surface velocity on the posterior side of the torso using a scanning laser Doppler vibrometer (SLDV). The second and more significant aim of this work is to develop and experimentally validate a computational model of sound transmission (using insonification) inside healthy human lungs that utilizes parenchymal and major airway geometry developed from CT scans. This computational model is essentially subject-based, and thus captures the variation in the geometric parameters of the pulmonary system from one person to another. A quantitative comparison of the sound propagation inside the lung parenchyma using in vivo experimentation and computational simulation via finite element analysis (FEA) is performed in order to evaluate the computational model. This subject-based computational model is used to perform finite element analysis in order to simulate specific pathological cases in the lung parenchyma associated with PTX, diffuse fibrosis, a localized tumor. FEA is used as a tool to develop unique “cross-sectional” views of the torso in order to visualize the nature of propagation of mechanical waves

inside healthy as well as diseased lung parenchyma. The author would like to note that to investigate the influence of Pneumonia on mechanical wave motion in the torso (using Percussion), a separate experimentally validated computational model developed by Peng et al [5] was used. This finite element model did not have a detailed airway mesh implemented inside the lungs in order to reduce the computational time of the simulations. This approximation is justified, as percussion involves transmission of mechanical wave motion through the chest (source of excitation located at the sternum), to the ribs, soft tissue of the lung and fat, and finally reaching the torso posterior. The presence of airways has a negligible impact on this transmission of mechanical wave motion, in stark contrast to insonification, which involves airway pressure being transmitted through the airways into the lung tissue which then transmits into the torso posterior.

2.3.1 Rationale for the present choice of pulmonary pathologies

The current work considers three pathologies that are expected to have substantially different effects on sound transmission. PTX involves an alteration in lung parenchymal geometry and density, as well as the introduction of trapped air between the parenchyma and chest wall. This should have a substantial effect on transmission. Fibrosis results in a distributed change in shear viscoelastic properties in the parenchyma with no significant change in geometry. A tumor results in a localized change in both tissue shear viscoelastic properties and density.

PTX is defined as an abnormal accumulation of air in the region between the lungs and the pleural space that results in a partial or complete collapse of the lung. PTX may be caused by penetrating or blunt chest trauma (e.g. knife wounds or car accidents) or may result from small sacs of air (blebs) in lung tissue that rupture, causing air to leak into the pleural space. The trapped air in the pleural space can increase the intra- pleural pressure and lead to lung collapse. PTX is more

common in men than in women. This condition occurs in 7.4 to 18 per 100,000 men and 1.2 to 6 per 100,000 women each year [18].

Idiopathic pulmonary fibrosis is a chronic, progressive lung disease where lung parenchyma becomes fibrotic, thereby compromising oxygenation of the blood. This scarring typically worsens over time until inadequate oxygenation leads to death. Most individuals survive 3 to 5 years after their diagnosis. In the United States, about 100,000 people are affected with 30,000 to 40,000 new cases diagnosed yearly [19].

Pneumonia is a pulmonary infection that leads to 3.5 million deaths each year [20], half of which occur in remote places that have no access to basic medical infrastructure and healthcare. In order to reduce the number of fatalities due to Pneumonia, there is a need to develop a cost-effective, quick and a relatively easy to use method of diagnosis that can enable an early diagnosis of the disease in populations having limited access to medical infrastructure.

Poor diagnostic sensitivity and specificity underlie the reason that lung cancer remains the leading cause of cancer death in both the United States and in the world for both men and women. Nearly 80% of lung cancer is detected at an advanced inoperable stage, while current systemic therapy offers only modest benefit. Regardless of the lung cancer type – small-cell or non-small-cell carcinoma squamous or adenocarcinoma – the tumorous growths alter the acoustic field in the lungs, as a result of changes in tissue density and viscoelasticity as compared to surrounding healthy lung tissue [21].

2.3.2 Notable improvements over past studies

Computational modelling has been used to better understand a wide variety of pulmonary function tests for several years. In the past year or two, researchers have been able to demonstrate commendable success in validation and usage of computational models in order to gain an insight into pulmonary diseases from a clinical point of view. For example, in 2019, the research group led by Tawhai and Lin (Choi et al [22]) developed a one dimensional CFD model to simulate the flow and pressure distribution of air in a healthy and an asthmatic lung and validated their results experimentally on 5 healthy and 5 asthmatic human subjects. The study determined flow distribution patterns inside healthy and asthmatic lungs and these experimentally validated flow distribution patterns can be used for imposing boundary conditions of three-dimensional CFD.

In the current work, the computational model aims to be more precise in comparison to the standard pulmonary function tests (PFT) by incorporating more region specific information with respect to the change of tissue viscoelastic properties due to pathologies such as PTX, fibrosis and tumors. The current work complements earlier research led by Choi et al [22] and lays down the scope and foundation for a more region-specific and precise assessment of mechanical wave motion inside human lung parenchyma by incorporating a detailed airway structure.

2.4 Theory

2.4.1 Airway acoustics: Impedance

Acoustic impedance is defined as the ratio of acoustic pressure to acoustic particle velocity and is a function of frequency. The acoustical impedance of airways was calculated by Habib *et al* [23], [24] using the modified Horsfield model. This model takes into account terminal respiratory tissues and assumes airway walls to be non-rigid. This section details the mathematical procedure used to determine the acoustical impedance of the airways.

2.4.2 Calculation of acoustical impedance using modified Horsfield model

A deterministic algorithm [25] was used to generate airways using Matlab followed by the creation of a finite element model using Ansys ICEM CFD. This section describes the mathematical technique used to compute the terminal impedance of each of the airway segments using the modified Horsfield model. The modified Horsfield model uses a “bottom-up” approach in calculating the acoustical impedance of the airway tree. For instance, the model first calculates the input acoustical impedance of a terminal (end) bronchiole ($n = \text{order number} = 1$). The model then “moves up” to the next higher level of bronchiole (i.e., larger airway) to iteratively calculate the acoustical impedance for the remainder of the airway tree, ending at $n = 35$ for the trachea. The degree of asymmetry at each airway bifurcation is specified by a recursion index denoted by $\Delta^{(n)}$. Therefore, an airway of order n bifurcates into two airways of order $n - 1$ and $n - 1 - \Delta^{(n)}$. For a particular airway having an order n , the bifurcated airway types (the daughter airways) are the same throughout the entire lung [6].

In general, for an n^{th} airway segment, the input acoustical impedance $Z_{in}^{(n)}[\omega]$ at the end located towards the trachea is given by the expression (with $n = 1, 2, \dots, 35$):

$$Z_{in}^{(n)}[\omega] = \frac{Z_T^n[\omega] + Z_0^n[\omega] \tanh\left[\gamma_0^{(n)}[\omega] l^{(n)}\right]}{1 + \left(Z_T^n[\omega]/Z_0^n[\omega]\right) \tanh\left[\gamma_0^{(n)}[\omega] l^{(n)}\right]} \quad \dots (2.1)$$

In the eq. (2.1), ω is the mechanical frequency in radians/second, $Z_0^{(n)}[\omega]$ is the characteristic impedance of the n^{th} airway segment **and** $\gamma_0^{(n)}[\omega]$ is the propagation coefficient of the same airway segment [26]. In addition, $Z_T^{(n)}[\omega]$ is the output acoustical impedance of an n^{th} airway segment, at the end away from the trachea. This is given by:

$$Z_T^{(n)}[\omega] = \begin{cases} \frac{N_T}{j\omega C_g + 1/\left[R_t + j\left(\omega I_t - 1/[\omega C_t]\right)\right]} & n = 1 \\ \frac{1}{1/Z_{in}^{(n-1)}[\omega] + 1/Z_{in}^{(n-1-\Delta[n])}[\omega]} & n = 2, \dots, 35 \end{cases} \quad \dots (2.2)$$

In eq. (2.2) above, N_T denotes the number of end segments (segments with order number = $n = 1$).

For any intermediate airway segment,

$$N_T^{(n)} = N_T^{(n-1)} + N_T^{(n-1-\Delta[n])} \quad \dots (2.3)$$

And, $Z_T^{(1)} = 1$ and $Z_T^{(n)} = N_T$. In addition, in eq. (2.2), R_t represents the resistance, I_t the inertia and C_t the compliance of terminal tissue; C_g represents the alveolar gas compression compliance (Dubois six-element terminal airway model [27]). For the current model, N_T evaluates to 2.35×10^6 .

2.4.3 Parenchymal acoustics

The lung parenchyma is a poroviscoelastic medium. There are two theories that model the transmission of sound inside the lung parenchyma, namely, the Biot Theory and the “effective medium” or “bubble swarm” theory. It has been demonstrated through experimentation [6] that the Biot theory is more accurate in predicting compression wave speed and attenuation. The dynamic oscillatory displacement u of the lung parenchyma is determined by solving the second-order differential equation [28]:

$$\mu u_{i,jj} + \left(K_b + \frac{\mu}{3}\right) u_{j,jj} - (\alpha - \beta) p_{,i} = \frac{d^2}{dt^2} (\rho - \beta \rho_f) u_i \quad \dots (2.4)$$

Similarly, the dynamic pressure (p) of the air inside the lung is given by the solution to the second order differential equation [28]:

$$\beta p_{,ii} - \frac{\phi^2}{R} \rho_f \frac{d^2 p}{dt^2} = \rho_f \frac{d^2}{dt^2} (\alpha - \beta) u_{i,i} \quad \dots (2.5)$$

In equations (2.4) and (2.5), μ and K_b are the shear modulus and the bulk modulus of the lung parenchyma respectively; ρ_f and ρ are the densities of the air and the lung parenchyma respectively; ϕ is the volume fraction of the air inside the lung; α , β and R are parameters that couple the lung parenchyma with the air inside them. Based on equations (2.4) and (2.5):

$$c_s = \sqrt{\frac{\mu}{\rho - \beta \rho_f}} \approx \sqrt{\frac{\mu}{\rho}} \quad \dots (2.6)$$

Note, c_s is the frequency-dependent complex-valued shear wave speed. This is due to the fact that the lung parenchyma is viscoelastic, thereby leading to a complex shear modulus. Thus, in equation (2.6) above, the shear modulus μ is a function of the frequency:

$$c_s(\omega) \approx \sqrt{\frac{\mu(\omega)}{\rho}} = \sqrt{\frac{\mu_R + i\mu_I}{\rho}} \quad \dots (2.7)$$

Equations (2.4) and (2.5) are coupled and this leads to two compression waves [6]: a fast compression wave and a slow compression wave having a much larger attenuation. For the fast compression wave with wavenumber k_{pf} , the wave propagation speed is given by:

$$c_{pf} = \frac{\omega}{\text{real}[k_{pf}]} \quad \dots (2.8)$$

On the other hand, for the slow compression wave with wavenumber k_{ps} , the propagation speed is given by:

$$c_{ps} = \frac{\omega}{\text{real}[k_{ps}]} \quad \dots (2.9)$$

Both of these speeds are frequency dependent. In the present study, due to the relative motion between the lung parenchyma and the air inside of it, the slow compression wave attenuates faster than the fast compression wave. Only the fast compression waves propagate in the lung parenchyma [6].

2.4.4 Geometrical modeling of the airways

A direct method of developing realistic geometrical models of the larger airways is through the use of CT images [29]. However, small conducting and terminal airways cannot be imaged with clarity. As a result, there are alternative methods of generating airway geometries based on mathematical algorithms. One of the first mathematical models for characterizing airway segments and branching behavior was developed by Horsfield *et al* [30]. Kitaoka *et al* [31] proposed a deterministic algorithm that could generate an elaborate and complex 3D airway geometry with the number of segments specified by the user in a non-symmetric manner. The current study uses an airway mesh that was developed and shared by Dr. Kitaoka's research group: this model was based on the seven fundamental laws of branching. The branching angle was restricted to 90 degrees. This model was not subject specific, but rather, a computational one. The authors recommend the usage of a newer and more accurate subject specific model of airways, developed by Henry *et al* [32], that uses CT images of the human subject in conjunction with computer algorithm.

2.4.5 Lung parenchyma: material model

In order to predict the mechanical wave motion inside the lung parenchyma for wavelengths that are greater than the dimensions of the microscopic heterogeneous features of the lung, homogenized representations of the lung's mechanical properties have been used [33]. Based on these homogenized representations, two models of wave propagation through the lung parenchyma have been proposed: the first model is based on the “bubble swarm” theory (also known as “effective medium” theory) [34] while the second model uses the Biot theory of poroelasticity [6]. The latter approach that uses Biot theory results in a better prediction of the behavior of mechanical waves as compared to the effective medium approach. The current work models the material properties of the lung parenchyma using the Biot theory.

2.5 Experimentation on Healthy Human Subjects

Experimental studies were performed on three healthy male human subjects, designated as HS1, HS2 and HS3, aged 25, 28 and 26 years; and with a BMI of 21.2, 21.5 and 21.4, respectively, after receiving appropriate Institutional Review Board (IRB) approval. Figure 1 (a) shows a schematic representation of the experimental setup with the healthy human subject seated in an upright position on a chair. In order to improve the signal to noise ratio (SNR), the human subject (HS) was requested to sit still and hold breath for 20 seconds during the experiment. Retro-reflective glass beads with a nominal diameter of 45 – 63 μm (P-RETRO-250, Polytec, Irvine, CA) were applied externally on the thorax that was intended for measurements (the red grid shown in fig. 1 (b)) in order to increase the reflection of the laser beam emanating from a SLDV (PSV-400, Polytec, Irvine, CA). A polyurethane tubing with an outer diameter of 29/32” and an inner diameter of 5/8” (McMaster-Carr, Elmhurst, IL, USA) was kept in the mouth of the human subject and inserted as deep as possible (while at the same time ensuring the safety and comfort of the human

subject). Acoustic energy generated from a 3.5-inch speaker (PDWR30W, PylePro, Brooklyn, NY) was guided through this tube into the mouth and transmitted into the lungs via the airways, finally propagating into the torso. A ¼-inch microphone (377A01, PCB Piezotronic, Depew, NY) capable of measuring sound pressure level was mounted at the outlet of the tube at the mouth of human subject; the signal recorded by this microphone was used as a reference for the SLDV. The speaker was driven by a waveform generator (SignalCalc ACE, Data Physics, San Jose, CA) that generated a broad-band periodic chirp signal with a spectral content from 50 – 600 Hz. The output of the waveform generator was connected to a power amplifier (P 3500S, Yamaha, Buena Park, CA). 63 scanning points (as shown in fig. 1b) were chosen on each side of the dorsal side of the torso of the human subject.

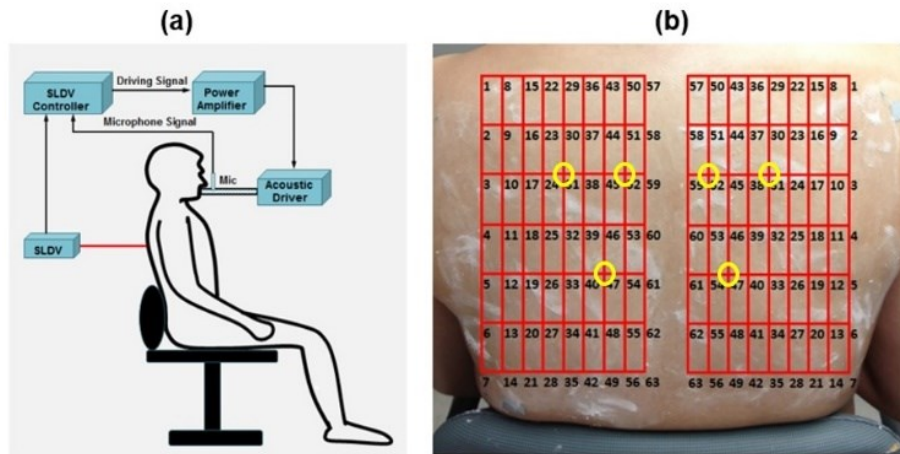


Figure 1. (a) Schematic diagram of the experimental setup; (b) The grid of measurement points on the dorsal side of torso of the human subject.

The SLDV system acquired the surface velocity (mm/s) at each point on the measurement grid shown in fig. 1 (b) and used this data to determine the frequency response function (FRF) at each point of measurement. The FRF is defined as the frequency-dependent ratio (in absolute scale) of

the output velocity measured by the SLDV over the reference pressure measured by the microphone placed close to the mouth of the human subject.

$$FRF = 20\log_{10}\left(\frac{\text{Surface velocity measured by SLDV}}{P_{ref}}\right) \quad \dots (2.10)$$

It is to be noted that the SLDV system measured the surface velocity at each of the point on the grid individually, beginning from the left-hand side (point no. 1 on the left grid) and ending on the point no. 63 on the left grid, before moving on to the grid on the right side (point no. 1) and continuing the measurements until point no. 63. This method of measuring the velocity first on the left grid, followed by the right grid, may have caused a certain amount of error (in the form of noise) during the measurement of velocity at the points on the right grid due to the inability of the human subject to hold the breath and stay still for a longer period of time, as is evident from the results discussed in section 2.4.

2.6 Development of Computational Models

2.6.1 Modeling healthy human lung parenchyma

A comprehensive three dimensional model of the human torso was generated using the CT images of a male human subject obtained online from the Visible Human Project database repository [35] of the National Library of Medicine (NLM). In order to construct the three dimensional geometries from the CT images, the CT image sets were imported and processed using Mimics v.14 (Materialise, Plymouth, MI), a commercial image processing and 3D modeling software. The generated 3-D model contained the geometry of the torso, the lungs, the ribcage, the cartilage, and the scapulae. The dimensions of the human model were rescaled to appreciate the average size of the human subjects in the experimental study.

The three dimensional models thus generated were then imported into ANSYS ICEM CFD 12.1 (Ansys Inc, Canonsburg, PA), a finite element mesh generation tool [36] which was used to generate a finite element model. This finite element model was then combined with the airway mesh generated using the deterministic algorithm developed by Kitaoka et al [25]. The surface of the trachea and the mainstem bronchi were extruded in the radial direction in order to create thickness of the airways. All the further generations of airways downstream of the mainstem bronchi were assumed to have a negligible thickness. This finite element model was then imported into Comsol (Comsol Group, Stockholm, Sweden), and material properties were assigned to each organ (component) as described in the section 2.3.3.

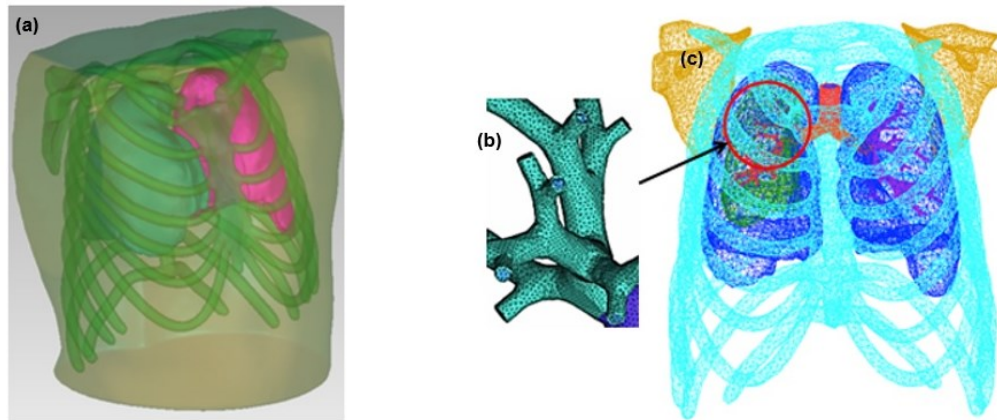


Figure 2. (a) Three dimensional modeling; (b) and (c): generation of finite element mesh.

The finite element mesh consisted of 689 839 tetrahedral elements (3D), 144 551 triangular elements (2D), 27 713 edge elements (1D) and 9 112 vertex elements. The minimum element quality was 0.07269 and the average element quality was 0.6168. The element volume ratio was 3.781×10^{-7} and the mesh volume was $3.426 \times 10^7 \text{ mm}^3$. These parameters were optimized with

regards to the accuracy of the solution vis-à-vis the computational time, based on our earlier experiences on modeling pulmonary acoustics in porcine and human computational analysis and studies [13, 14, 18]. The three dimensional computational model of the healthy lung had 36 608 triangular surface elements and a mesh area of a 95 370 mm³; the lung affected with PTX had 16 476 triangular surface elements and a mesh area of 42 600 mm³.

2.6.2 Material properties of bone and soft tissue

This section explains the calculation of material properties that were assigned to bones (this includes the cartilage as well as the scapulae) and the soft tissue of the torso. The material properties of the normal lung, as well as the lung affected with PTX, fibrosis and a lung containing local tumor have been explained separately in the subsequent sections.

The chest wall was considered to be a viscoelastic medium and a Voigt model of viscoelasticity was used to determine the frequency dependent shear modulus of it [37], [38] as shown in equation (2.11) below:

$$\mu_t = \mu_{t1} + j\omega\mu_{t2} \quad \dots (2.11)$$

In eq. (2.11), the subscript “t” denotes the soft tissue; μ_{t1} and μ_{t2} denote the shear elasticity and shear viscosity with the values being $\mu_{t1} = 2.5 \times 10^3 \text{ Pa}$ and $\mu_{t2} = 15 \text{ Pa.s}$. Assuming a density of 1100 kg/m³, the complex shear wave speed can then be estimated through equation (2.7) and the compression wave speed can be estimated using equation (2.9). The complex Young’s modulus of the bone can be represented by

$$E = E_{b1} + j \cdot E_{b2} \quad \dots (2.12)$$

with $\tan \delta_E = E_{b2} / E_{b1}$ [39] and subscript “b” denotes the bone.

The value of the factor $\tan \delta_E$ is frequency-dependent and was experimentally measured by Garner et al [39]. For the current frequency range of interest, the real part of E is taken to be $E_{b1} = 12.7 \text{ GPa}$ in the computational simulation. In addition, the complex shear modulus is expressed as

$$\mu_b = \mu_{b1} + j\omega\mu_{b2} \quad (2.13)$$

with $\tan \delta_\mu = \mu_{b2} / \mu_{b1}$. The factor $\tan \delta_\mu$ was determined from experimental measurements [39], [40] and the real part of shear modulus is $\mu_{b1} = 3.15 \text{ GPa}$.

In FEA using Comsol, Version 5.3a (Comsol Group, Stockholm, Sweden), the region corresponding to the healthy lung, the collapsed lung and the air were modeled using the *Pressure Acoustics Module*. The soft tissue and the bone were modeled using the *Linear Elastic Material Model (viscoelastic sub-module)*. A *free-free boundary condition* was applied on the torso surface while an *acoustic-structure boundary interaction* was imposed on the lung-muscle tissue interface. An input harmonic excitation of 1 Pa (that corresponds to insonification at the trachea) was applied at the inlet of the trachea.

2.6.3 Computational modeling of Pneumothorax (PTX)

To simulate the pathological case of PTX, a 3-dimensional model of the normal right lung was shrunk by 70% in volume (in order to simulate the case of 90% PTX) and fit inside the original lung cavity. The PTX percentage is defined by the ratio of volume of air which occupies the chest cavity outside the lung and the air volume in normal lungs [8], [33]. 3-dimensional models of all the other organs were left unaltered. Figure 3 (a) shows the 3-dimensional model used in the

simulation of PTX: the right lung (with an air fraction of $\phi = 58.5\%$) represents the condition of PTX and the left lung (with an air fraction of $\phi = 75\%$) corresponds to a normal lung.

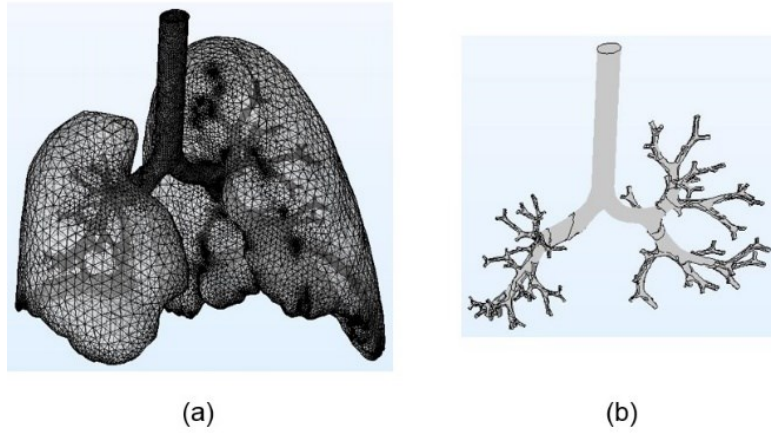


Figure 3. Computational simulation of PTX (collapsed lung): (a) Finite element model of lungs (healthy left lung and right lung affected with PTX) and (b) 3-dimensional model of airways.

According to Peng et al. [9], changes in trans-pulmonary pressure lead to a significant change in the diameter of small airway segments that have a negligible cartilage content. On the other hand, this change in diameter due to the collapse of a lung is negligible for larger airway segments such as the main stem bronchi, trachea and those branches of airways with order number $n = 31$ to $n = 35$. For a small airway segment of order number n , the relationship between the change in airway radius $da^{(n)}$ and the change in trans-pulmonary pressure dp is governed by:

$$da^{(n)} = \frac{\alpha^{(n)}}{2} dp, \alpha = \frac{A}{A_0} \quad \dots (2.14)$$

In eq. (2.14), A is the reduced cross-sectional area due to change in trans-pulmonary pressure and A_0 is the original cross-sectional area.

2.6.3.1 Material properties of healthy and PTX lung

Biot theory [6] was used to compute the material properties of both the healthy lung and the lung affected by PTX. For instance, the density of the normal lung (having volume fraction of air, $\phi = 75\%$) was computed using the Biot theory and was found to be 250 kg/m^3 while that of the lung affected with PTX (with an air volume fraction of 58.5%) was estimated to be 418.67 kg/m^3 . In addition, the speed of primary waves (c_p or compression wave) and secondary waves (c_s or shear wave) were first estimated at discrete frequencies using Biot theory. Non-linear interpolation (using best curve fit) was then used to compute these properties over a range of frequencies from 100 Hz to 500 Hz.

Impedance of the terminal airways was computed using the Horsfield order number [30], which in turn was computed using the mean diameter. For normal airways the mean diameter of the terminal segments was 2.31 mm corresponding to an order number of 18. In the PTX state, the lung is collapsed and this causes a decrease in the diameter of the airways. Thus the mean diameter for the terminal segments corresponding to the PTX lung was 0.19 mm corresponding to an order number of 8. The impedance of normal lung was computed to be $11.74 - i*(0.55) \text{ Pa-s/m}$ while the impedance of the PTX lung was computed to be $17.26 - i*(38.04) \text{ Pa-s/m}$. The terminal impedances thus obtained were then applied to end of the airways as a boundary condition in the computational simulation and the material properties of airways were obtained from Royston et al [25]. Table 1 summarizes the material properties (c_p and c_s) that were used in the computational simulation. Note that while the table lists the values of the wave speeds at particular frequencies, in an actual finite element simulation non-linear interpolating polynomials were used to compute the frequency dependent wave speeds.

Table 1. Sample values of the material properties used in the computational study using finite element analysis.

Frequency, Hz	<i>Normal Lung</i>			<i>PTX Lung</i>		
	(c_p), m/s	(c_s), m/s	Impedance (Pa-s/m)	(c_p), m/s	(c_s), m/s	Impedance (Pa-s/m)
200	26.02+4.18i	5.62+1.12i	14.14+22.72i	23.47+5.96i	4.36+0.90i	15.16+19.63i
300	27.09+5.64i	5.91+1.27i	15.94+34.32i	25.15+7.90i	4.58+0.98i	16.23+30.22i
400	28.19+6.73i	6.14+1.38i	17.33+40.65i	26.81+9.24i	4.76+1.07i	18.19+45.71i
500	29.24+7.55i	6.33+1.47i	18.76+51.1i	28.32+10.18i	4.91+1.14i	21.04+56.93i

2.6.3.2 Mode of excitation to investigate PTX

To study the influence of pneumothorax on the sound transmission characteristics of the lungs, excitation in the form of a sinusoidal pressure input at the top of the trachea of amplitude 1 Pa was applied over a range of frequencies from 100 Hz to 500 Hz in the computer simulation to be compared to experimental data obtained as described in Section 2.5.

2.6.4 Computational modeling of Tumor

To simulate the pathological case of a tumor, two spherical regions of diameter 3 cm and 2 cm were created as shown in the figure 4 below. As per the guidelines for early diagnosis, detection and staging of lung carcinoma provided by the American Cancer Society [41], a tumor of diameter more than 3 cm but less than 4 cm is considered to be at Stage IB. This category of tumor is considered to be non-malign (the cancer has not spread to nearby lymph nodes or to distant parts of the body).

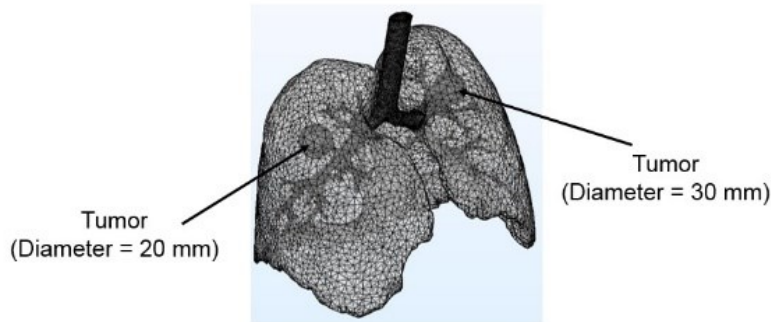


Figure 4. Finite element modelling of tumor.

2.6.4.1 Material properties of Tumors

The tumors have been modeled as a viscoelastic medium. Current literature does not provide macroscopic shear viscoelastic properties of lung tumor. Based on a clinical study [42] performed on 6 breast carcinoma patients, both the shear viscosity and shear stiffness of the fibro adenomas and carcinomas were larger than those of the normal tissue. In particular, shear stiffness was the parameter that could be used to differentiate a malign tissue from normal tissue. Using that study, the shear stiffness of the tumors was estimated to be 3.33 times the shear stiffness of the normal lung tissue. While the density of the normal lung tissue (with an air volume fraction of $\phi = 0.75$) was estimated using the Biot theory and was found to be 250 kg/m^3 , the density of tumor was assumed to be that of water (that is, 1000 kg/m^3). Table 2 lists the compression and shear wave speeds in a tumor [6].

Table 2. Compression and shear wave speeds used in the computational study of a lung with tumor.

Frequency (Hz)	c_p (m/s)	c_s (m/s)
300	$27.66 + 5.26i$	$8.26 + 0.91i$
500	$32.13 + 9.23i$	$13.91 + 8.09i$
800	$34.47 + 10.40i$	$14.78 + 8.54i$

2.6.5 Computational modeling of Fibrosis

The 3-D model used for simulating fibrosis was identical to that of a normal lung, with material properties for the fibrotic lung computed as follows.

2.6.5.1 Material properties of lung with fibrosis

Current literature does not have studies pertaining to the macroscopic shear viscosity of lungs affected with fibrosis in the frequency range under consideration in the current study (100 Hz –

800 Hz). In their assessment of six human breast-fibroadenoma patients, Sinkus et al. [42] estimated the shear viscosity and shear stiffness of fibroadenomas and carcinomas at a frequency of 65 Hz and noted that these values were larger than the surrounding normal tissue. In the current study, the shear stiffness increase ratio estimated by Sinkus et al. was extrapolated to the current frequency range of interest. Therefore, the shear stiffness of the fibrotic tissue was assumed to be 1.5 times that of the normal tissue; further, the shear viscosity of the fibrotic lung was chosen such that the shear wave attenuation, governed by the imaginary part of the shear wave number, equals that of the normal lung. In order to simulate the conditions of fibrosis using FEA, the modified material properties in terms of the shear viscoelastic parameters described above were applied to the entire lung parenchyma (as listed in Table 3), while all the other material properties remained the same.

Table 3. Compression and shear wave speeds used in the computational study of a normal lung and a lung with fibrosis.

Frequency (Hz)	Normal lung		Lung with fibrosis	
	Compression wave speed (m/s)	Shear wave speed (m/s)	Compression wave speed (m/s)	Shear wave speed (m/s)
500	$29.24 + 7.55i$	$6.33 + 1.47i$	$29.66 + 7.56i$	$7.95 + 2.36i$
800	$31.81 + 9.12i$	$6.82 + 1.68i$	$32.18 + 9.11i$	$8.53 + 2.69i$

2.6.5.2 Mode of mechanical excitation for investigating Fibrosis: Side shear

Insonification is not an effective way to differentiate a healthy lung from a fibrotic lung based on visualization of compression waves [6]. The authors therefore propose the use of shear excitation technique in order to generate and transmit shear waves within the chest so as to effectively differentiate a normal lung from a fibrotic lung. As shown in the fig. 5 below, shear waves were

generated by using a “rubbing” motion (or, a sideward to-and-fro excitation) on the chest through the application of a harmonic displacement of 1 mm along the y -direction.

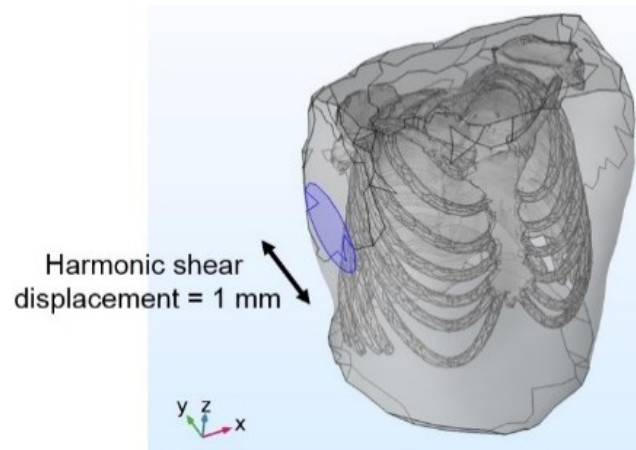


Figure 5. Application of a “shear” excitation on the side of the torso to investigate fibrosis.

2.6.6 Computational modeling of Pneumonia

An earlier work of the research group [5] involved the development and validation of a technique known as percussion that involves application of mechanical wave motion at the sternum of porcine subjects and measuring the resulting surface velocity of the soft tissue at the posterior side of the torso. One of the primary objectives of this study was to develop and experimentally validate a computational model of sound propagation inside the lung parenchyma using percussion in order to predict the response of the chest and pulmonary system to surface excitation (mechanical motion). The current study makes use of this experimentally validated computational model in order to predict and quantify the changes in nature of mechanical wave motion in lungs as well as chest tissue due to the condition of Pneumonia. As shown in fig. 6 below, the bottom lobe of the left lung is modeled to simulate the condition of Pneumonia.

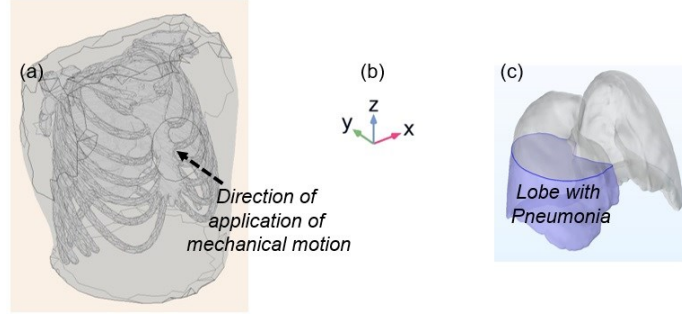


Figure 6. Computational modeling and simulation of pneumonia: (a) Three dimensional model showing the circular region on the chest surface where mechanical motion (percussion) is applied; (b) orientation of the global coordinate system, with the y-axis pointing along the direction of mechanical motion and (c) three dimensional model of the lung tissue, with the lobe highlighted in indigo color representing the condition of pneumonia.

The lobe with pneumonia is modeled to be filled with water (density = 1000 kg/m^3 and wave speed = speed of sound in water = 1490 m/s). On the other hand, the material properties of the healthy lung are dependent on the frequency of the imposed mechanical motion, and can be found in an earlier study performed by the members of the same research group [16].

2.7 Results and Discussion

2.7.1 Insonification experiments on healthy human subjects

Figure 7 presents a comparison of the average Frequency Response Function (FRF, defined in equation 2.10 as the lung normal surface velocity (in dB) m/s with respect to a 1 Pa input acoustic pressure), shown in blue color, versus average plus one standard deviation values (shown in green) versus the FRF obtained from finite element analysis (represented in red). Averages for experimental FRF were computed by dividing the sum of FRF for each HS at a given experimental frequency by 3.

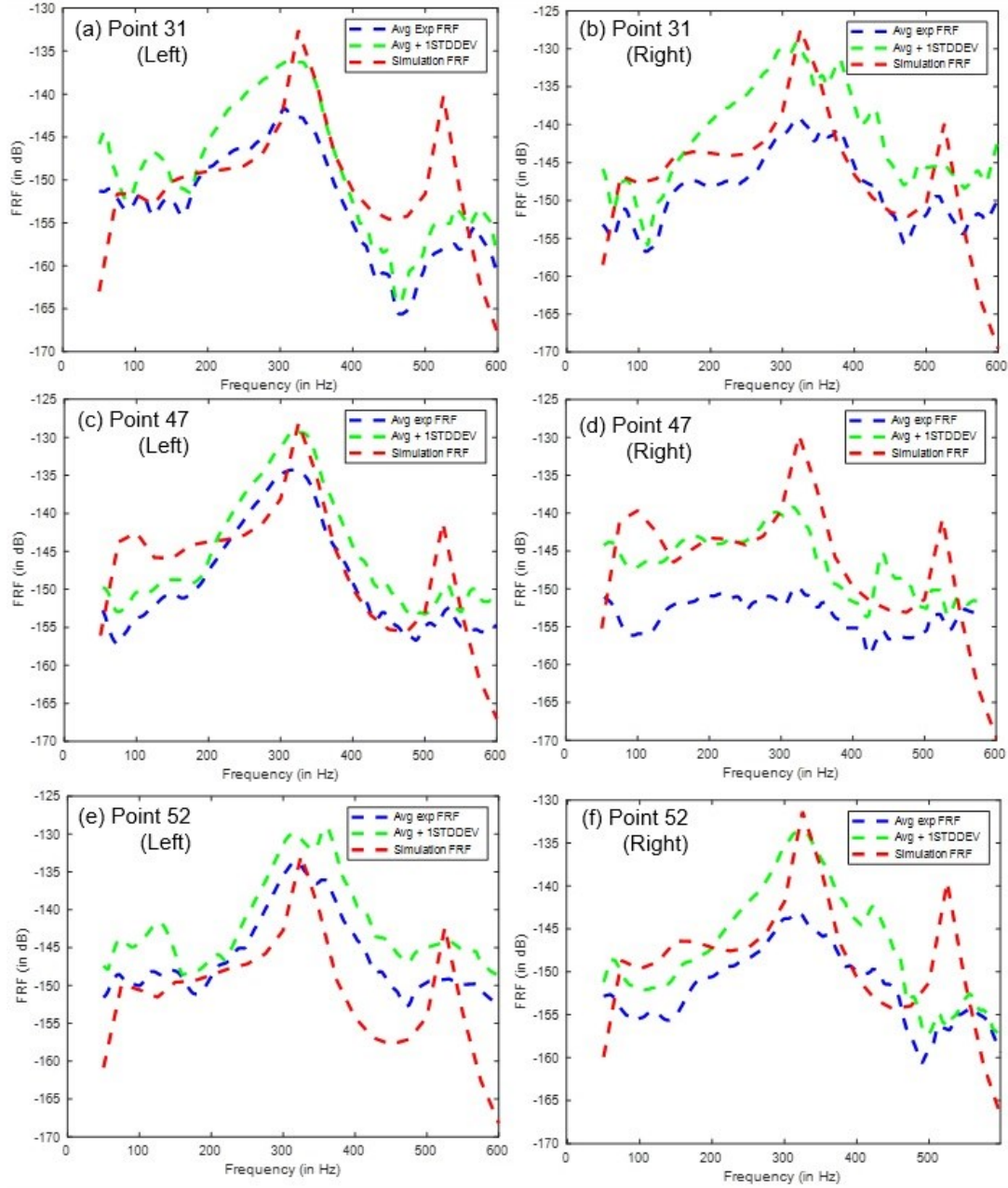


Figure 7. A comparison of results of FRFs for in-vivo experiments involving 3 Human Subjects, with results presented in terms of the Average FRF (blue dashed curve) and Average Plus One Standard Deviation (green dashed curve), both compared against the FRF values obtained from finite element simulation (red dashed curve). (a,c,e): comparison of FRF (experiment versus FEA) for points #31, #47 and #52 on the left side of the dorsal side of torso (figure 1(b)); (b,d,f): comparison of FRF (experiment versus FEA) for points #31, #47, and #52 on the right side of the dorsal side of torso (Figure 1(b)).

Standard deviation at each frequency was then computed for each of these experimental FRFs using the following mathematical expression:

$$\text{Standard Deviation} = \sqrt{\frac{(HS1-AVG)^2 + (HS2-AVG)^2 + (HS3-AVG)^2}{3}} \quad \dots (2.15)$$

From fig. 7, it is observed that the FRF obtained from computational simulation (red curve) follows a similar trend as that of the average plus one standard deviation FRF (green curve) with respect to the spectral magnitudes and features. It is to be noted that this trend is captured more so in the measurements performed on the left side of the torso (fig. 7 (a), (c) and (e)) than in the FRF values computed for points on the right side of the torso (fig. 7 (b), (d) and (f)). This is due to the fact that the SLDV first measured the surface velocity on the left side of the torso posterior before moving on to the points on the right side of the torso posterior, all while the human subject was holding his/ her breath. This is believed to have resulted in some deviation in the measured values of surface velocity (in comparison to the computational study, which represents an idealized situation) as some human subjects were unable to hold their breath while the measurements were still being performed on the right side of the torso posterior. This is evident in particular in fig. 7 (d). The observation that the simulation seems to bias to a larger magnitude than the experimental measurements (closer to one standard deviation above it) across many frequencies suggests some small systematic error that is under investigation. Nonetheless, major trends with frequency, such as peaks at ~300 and just over 500 Hz, are generally captured. In addition, a shift of peaks and valleys of computational results are observed (in comparison to the in vivo human experiments). These shifts could be due to the difference in the size and dimensions of the finite element model as compared to the actual human subjects used in the experimentation. The computational study used a 3-dimensional model that was scaled to the average size of the three human subjects.

Figure 8 shows a contour plot of the lung normal surface velocity amplitude (in dB m/s per 1 Pa of input acoustic pressure), at a frequency of 500 Hz for a healthy human subject, computed using (a) FE simulation and (b) in-vivo insonification experiment. The red rectangle (in fig. 8 (a)) represents the Region of Interest (ROI) on the finite element model that corresponds to the same region on the corresponding contour plots shown for the in-vivo experiments in fig. 8 (b).

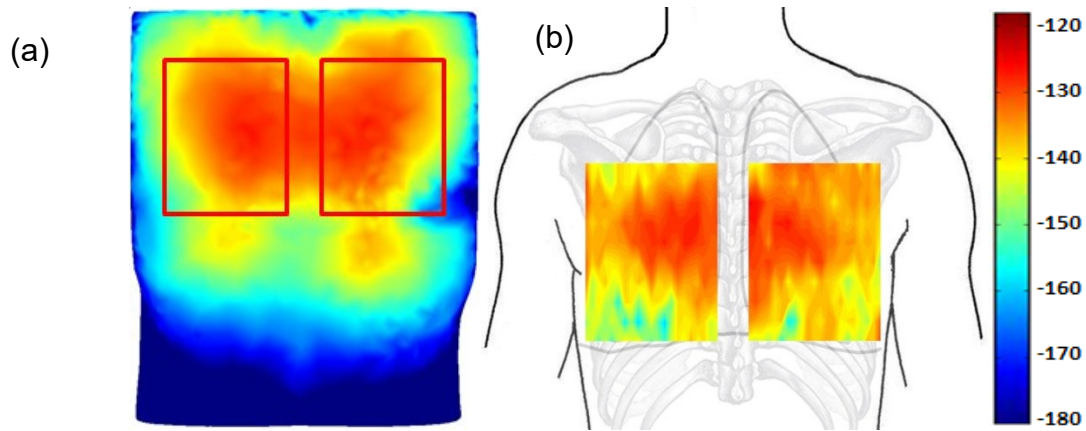


Figure 8. A comparison of the lung normal surface velocity amplitude (in dB m/s per 1 Pa of input acoustic pressure) at 500 Hz for a healthy human torso, computed using (a) simulation and (b) experiment. The rectangle in (a) represents the region of interest for the same areas corresponding to the measurements performed in the experiment as shown in (b).

From fig. 8 it is observed that both the experiment and computational simulation show a comparable pattern of velocity amplitude distribution. As expected, the amplitude of velocity is larger over the central areas of the lung (due to the source of excitation being located at the trachea, the path of propagation of excitation is through the airways into the lung parenchyma), the velocity amplitude gradually decays in the peripheral areas. In addition, the pattern of distribution of velocity amplitude observed in the experiment is more mottled than in computational simulation, probably due to the coarser resolution in the experiment and experimental noise that can result in smaller measured velocity amplitudes at some of the scanned points.

It is noted that some models of frequency propagation include a correction for the effect that cheek shunting has on the measurement of the impedance. Alternately, experimental subjects are asked to hold their cheeks in order to minimize cheek shunting. For the current study, however, the authors did not make this correction as the current work made use of measurements of transmission of mechanical wave motion within the lung parenchyma and the torso, rather than making impedance measurements. Corrections to eliminate the effects of cheek shunting could be included in future studies.

2.7.2 Computational simulation of PTX

The predominant type of waves observed in the lungs due to insonification are compression waves, not shear waves [6]. Figure 9 shows contours of amplitude of y -(i.e., ventrodorsal) velocity (in dB scale) across a cross-section of torso taken at the geometric center ($z = 0$) of the 3D model of the FE study. As the location of measurement of acoustic signal is often at the dorsal side of the torso, an emphasis is therefore laid on the amplitude of wave velocity at the dorsal side of the torso immediately behind the healthy lung and the collapsed lung (due to pneumothorax). It is observed that at lower frequency, the amplitude of velocity is equal behind both the healthy lung and the lung affected with PTX. As the frequency increases, the preferred path of propagation of the compression waves is through the healthy lung more than the lung affected by PTX. This is reflected in the higher amplitude of the velocity at the dorsal side of the torso behind the healthy lung (fig. 9 (e)).

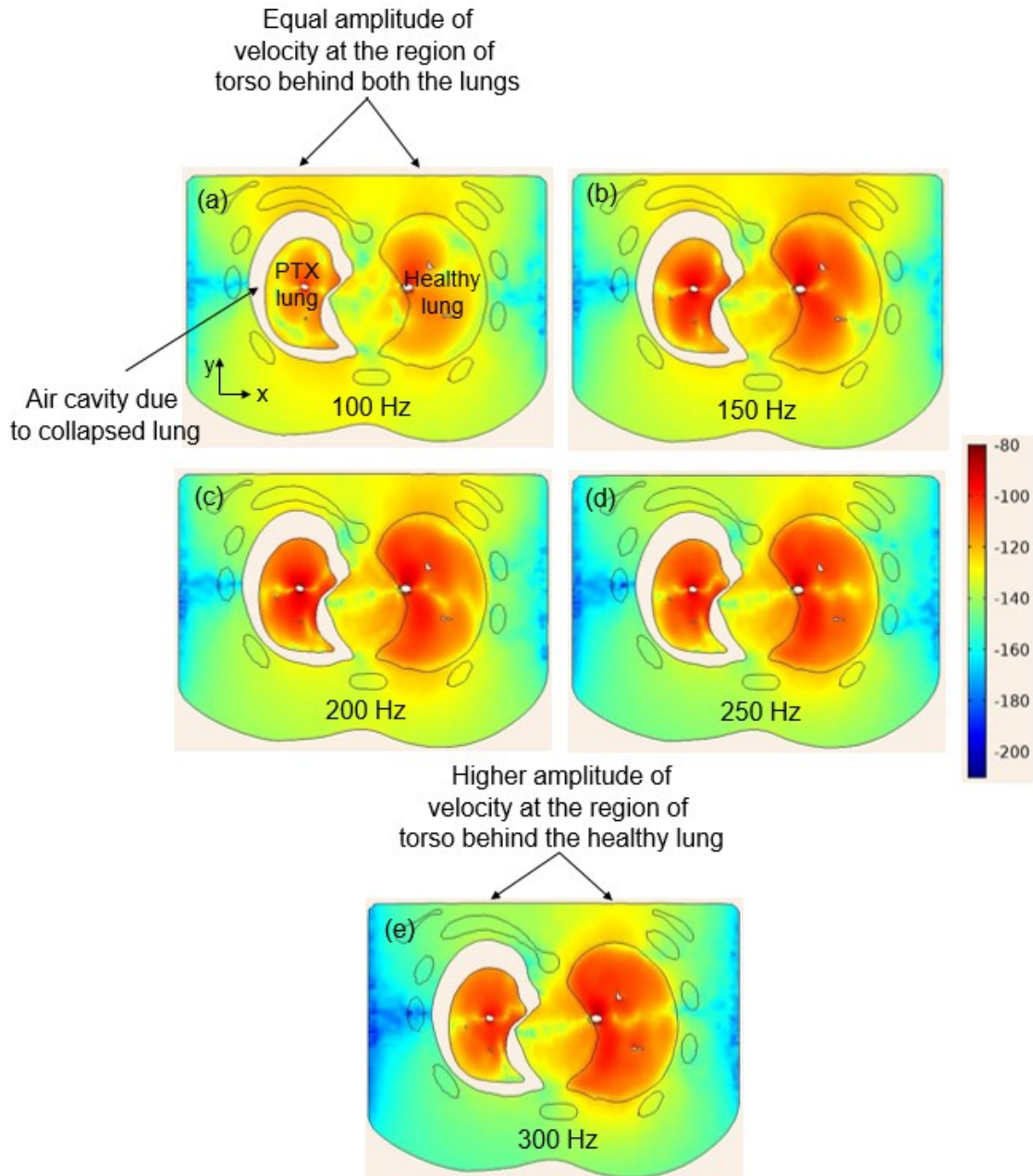


Figure 9. Contour plots of acoustic velocity (in y-direction) shown at a cross section taken in the middle of the torso, as a function of frequency.

Figure 10 presents another view of the results presented in figure 9, in terms of the surface velocity measured on the torso posterior, on the regions immediately behind the healthy lung as well as the lung affected with PTX.

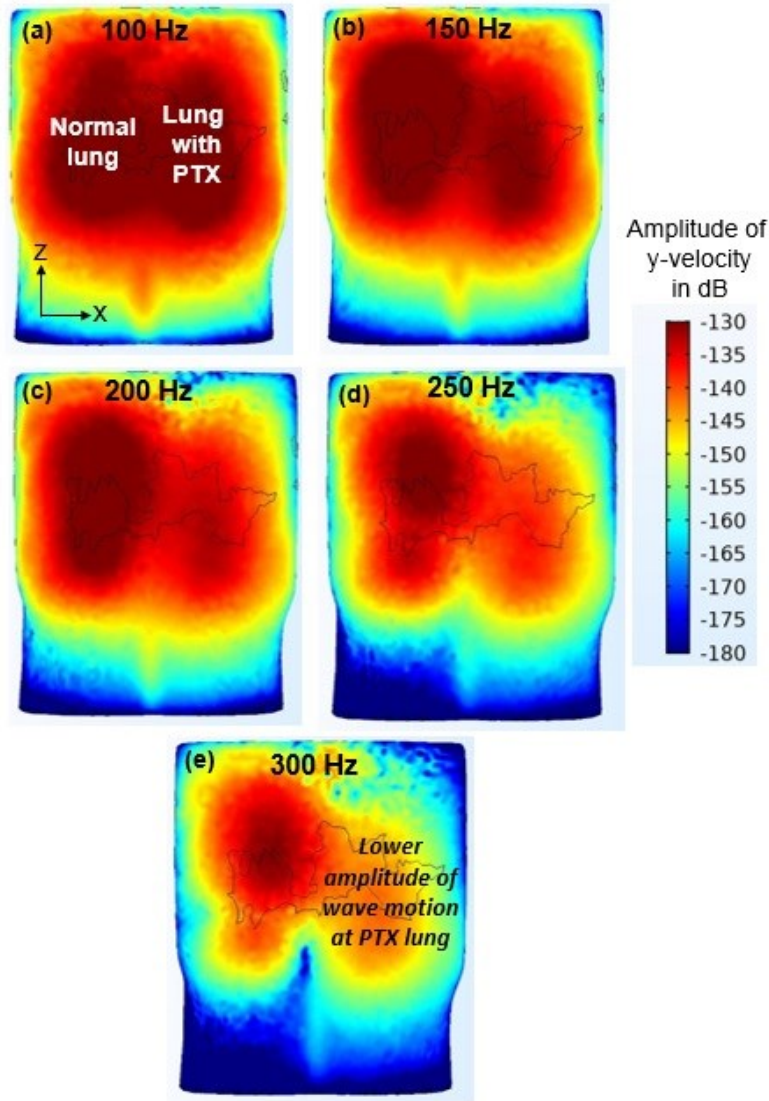


Figure 10. Contour plots of surface velocity in absolute scale (in y -direction) at the dorsal side of the torso as a function of frequency. Note: y -direction is normal to the zx -plane, pointing outwards from the plane of the image.

The observations drawn from these contour plots reinforce the same mechanism of wave propagation as a function of increasing frequency, as discussed above where at lower frequencies, the path of propagation of compression waves is through both the healthy lung and collapsed lung. However, as the frequency increases, the path of propagation of the compression waves is

predominantly through the healthy lung. These observed spectral trends are also in agreement with human and animal studies of the acoustic effects of PTX [43]–[45].

Clinically, this finding is significant because it enables non-invasive diagnosis of the presence of PTX by measuring the sound that is transmitted to the chest surface over the lungs. At higher frequencies, the region of the torso surface nearest the lung affected with PTX would give a significantly weaker signal in comparison to a region of torso surface near the healthy lung. A reason for this could be an increased impedance mismatch between the surrounding normal tissue and the collapsed part of the lung (PTX) that has an air cavity. This air cavity imposes a barrier to the propagation of compression waves thereby leading to a weaker signal at the region of the torso behind a PTX lung.

2.7.3 Computational simulation of Fibrosis

This section presents the results of computational studies (FE simulations) performed using two techniques, viz., insonification and side shear excitation.

2.7.3.1 Simulation of Fibrosis using Insonification

Figure 11 presents contour plots of amplitude of displacement (in dB scale) in x-, y- and z- directions at 500 Hz and 800 Hz for both healthy lung as well as the lung affected with fibrosis. The patterns of propagation of compression waves show insignificant change due to the presence of fibrosis, which confirms the findings of the computational analysis done on porcine subjects [6].

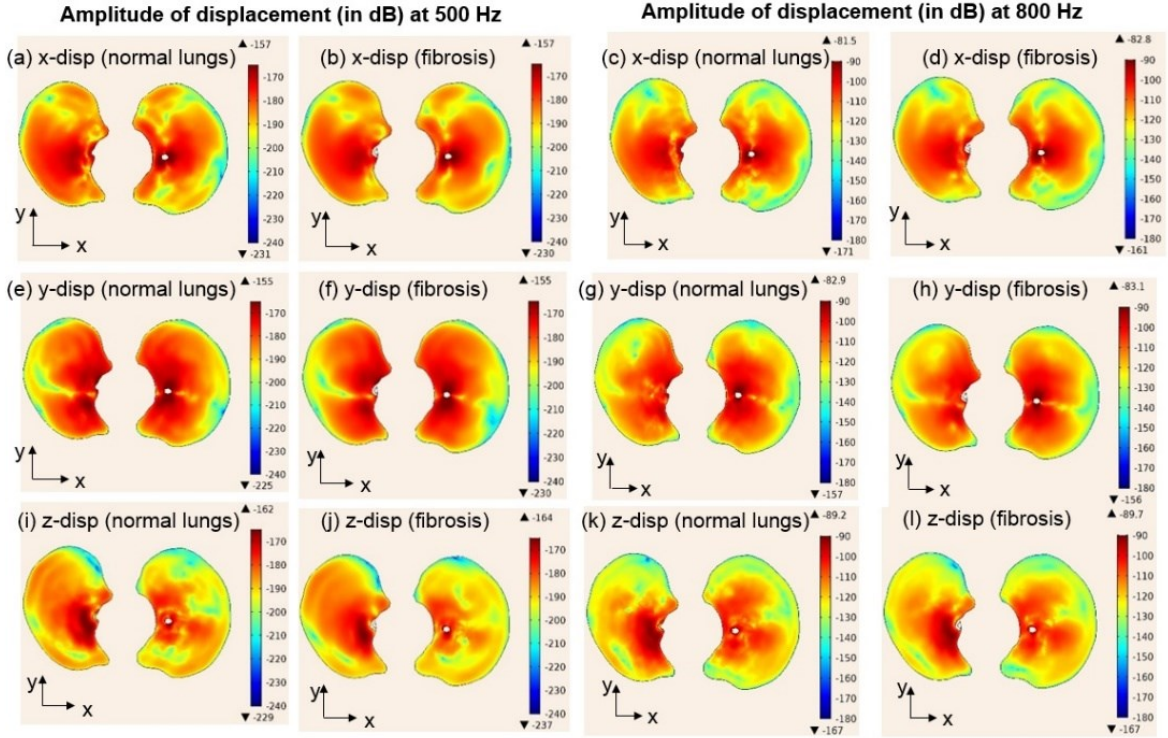


Figure 11. Contour plots of amplitude of displacement (in absolute scale, dB), at two frequencies of 500 Hz ((a), (b), (e), (f), (i), (j)) and 800 Hz ((c), (d), (g), (h), (k), (l)).

As such, insonification is not an ideal mode of excitation to detect the presence of fibrosis. Thus “shear” excitation is used to introduce shear waves of lower wavelengths (as compared to the compression waves introduced by insonification).

2.7.3.2 Simulation of Fibrosis using Side Shear

Figure 12 presents the results of “shear” mechanical excitation applied to one side of the torso in order to generate shear waves inside the tissue. The curl operator was applied to eliminate the compression wave component so that the resultant wave form has contributions of pure shear waves. From these contour plots, it is observed that the wavelength of shear waves increases due to fibrosis, due to an increase in the shear stiffness of the lung with fibrosis. Furthermore, this difference is more obvious at lower mechanical frequencies, for example at 100 Hz and at 200 Hz.

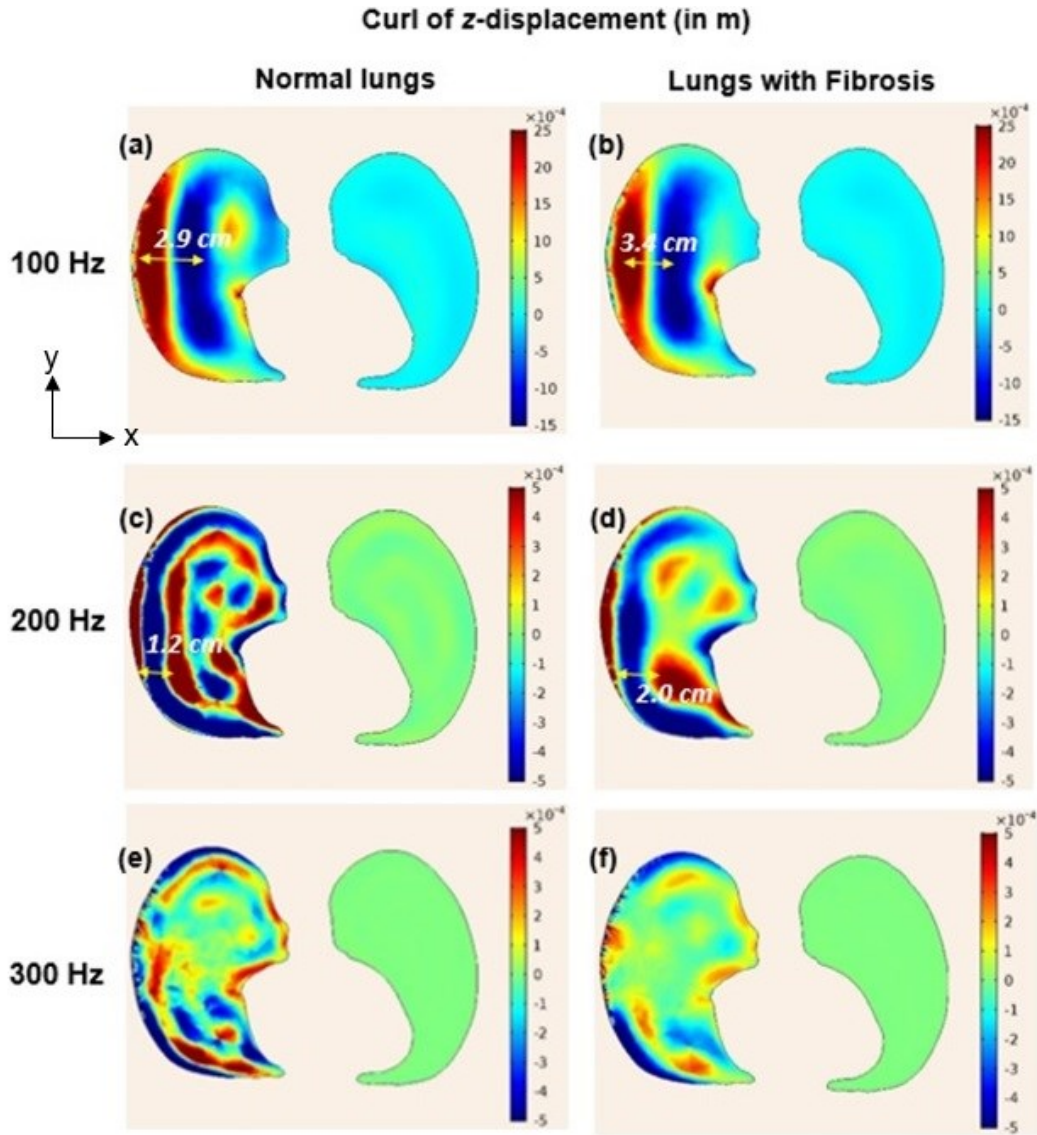


Figure 12. Contour plots of curl of displacement in z-direction (in m) showing propagation of shear waves in normal lung ((a), (c), (e)) and a lung with fibrosis ((b), (d), (f)) at frequencies of 100 Hz, 200 Hz and 300 Hz.

From a clinical perspective, this signifies that application of a shear excitation to the torso is more effective method of determining the presence of fibrosis as compared to the use of insonification, which predominantly excites compression waves. For instance, shear excitation can be applied by means of a passive mechanical driver that is placed on the surface of the torso, and the resulting

wave motion can be visualized using magnetic resonance elastography technique, as described in [46].

2.7.4 Computational simulation of Tumor

Figure 13 presents the results of computational analysis of the pathological case of a tumor, using insonification as a means to introduce compression waves in the lung parenchyma. In these contours, both the healthy (fig. 13 (a), (c), (e)) as well as the lungs with tumor (fig. 13 (b), (d), (f)) show the geometry of a tumor. The mechanical properties of the tumor region are the same as that of a healthy lung parenchyma in healthy case, while the material properties of the tumor region are those listed in Table 2 in the case of a lung containing a tumor. From the contour plots of velocity amplitude (in dB scale) shown in figure 13, it is evident that the presence of tumor leads to an increase of the wavelength of the propagating compression waves in the vicinity of the tumor region. In addition, due to the impedance mismatch between the tumor and the surrounding lung parenchyma, the velocity amplitudes in the tumor region are diminished, the tumor boundary near the main stem bronchi is more visible possibly facilitating earlier detection of smaller tumors while they are still operable. Several recent and ongoing studies have focused on developing new techniques for enhancing lung MRE [12]. These results suggest that a method that implements airway compression wave acoustic forcing and measures parenchymal displacement or velocity (e.g. using MRE) may be useful for radiation free detection of pulmonary neoplasms.

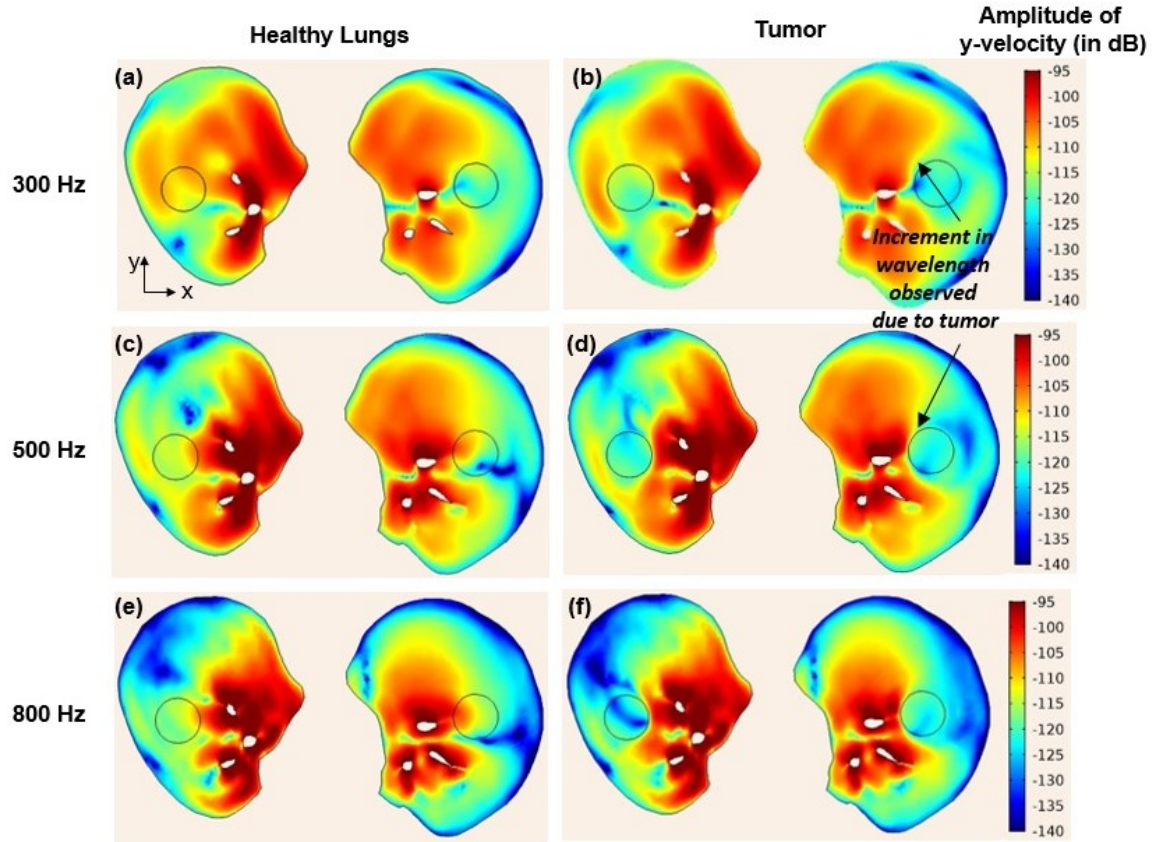


Figure 13. Contour plots of amplitude of velocity (in y-direction), at 300 Hz, 500 Hz and 800 Hz for a healthy lung ((a), (c), (e)) and lung containing tumor ((b), (d), (f)).

2.7.5 Computational simulation of Pneumonia

Figure 14 presents the results of FEA in terms of the torso surface velocity (y-direction), in dB, at the posterior surface of the torso (fig. 14 (a)-(d)). FEA enables unique visualization of propagation of mechanical wave motion along a slice taken within the chest surface as shown in fig. 14 (e). The slice plane is chosen so as to be approximately at the middle of the torso volume. Figure 14 (f)-(i) represents the y-directional velocity amplitude (in dB scale) for the slice chosen in fig. 14 (e). In all of these plots, velocity is shown only along the y-direction, as the direction of application of mechanical motion is along the y-axis (fig. 6 (a)-(b)).

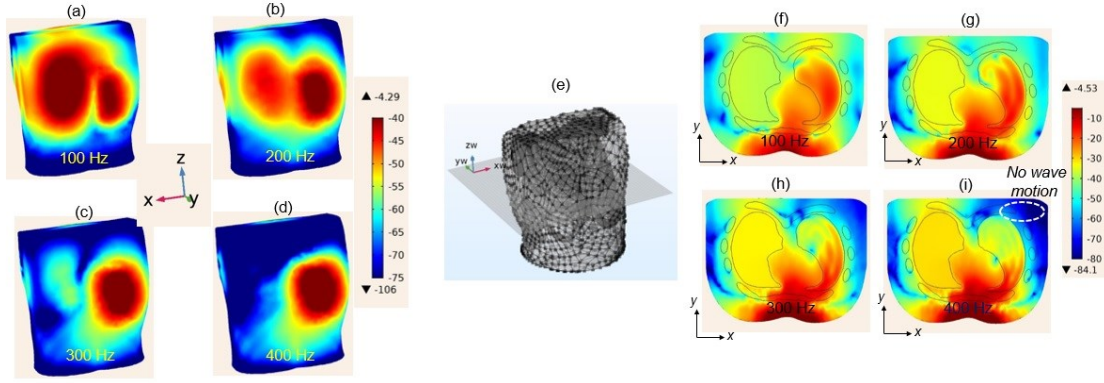


Figure 14. Results of Finite Element Simulation: (a) – (d): Plots of y-directional velocity amplitude (in dB scale) shown on the posterior surface of the torso; (e): selection of a cross-sectional slice at the middle of the torso to enable visualization of mechanical wave motion inside the chest; (f) – (i): plots of velocity amplitude in y-direction for the slice chosen at the middle of the chest region. At higher mechanical frequencies, the preferred path of propagation of mechanical waves is through the infected lung (pneumonia), as is evident from the regions of “zero wave motion” at the posterior of the torso region that is behind the healthy lung (contours in dark blue color, as highlighted in (i)).

From the plots of y-directional velocity, it is observed that:

- At lower frequencies (50-100 Hz) the path of wave propagation is predominantly through the rib/bones and the healthy lung.
- At intermediate frequencies (100-200 Hz) the path of wave propagation begins a transition from the rib/bone region to the region containing the lung affected by Pneumonia region.
- At higher frequencies (300-600 Hz) the path of wave propagation is through the lobe of the lung affected by Pneumonia.

The investigator postulates the reason for this change of path of wave motion to be the frequency-dependent nature of the wave velocity and impedance, as defined in eq. (2.16) below:

$$Z(\omega) = \rho c(\omega) \quad \dots (2.16)$$

In eq. (1), ω is the mechanical frequency (in rad/s), Z is the acoustical impedance of the soft tissue, ρ is the density of the soft tissue and c is the speed of propagation of the mechanical wave. Inside a healthy lung, due to a large impedance mismatch between the soft tissue and the semi-rigid chest wall (bones), most of the mechanical wave motion is reflected back to the anterior surface. However, in the case of a lung infected with pneumonia (in the current simulation such a lung lobe is assumed to be filled with water), the presence of “pleural fluid” surrounding the soft tissue reduces the impedance mismatch at the interface between the soft tissue and the chest wall, and as a result, mechanical waves propagate preferably through the diseased lung (pneumonia) at higher mechanical frequencies. This is shown in fig. 14 (c, d) and fig. 14 (h, i), where, there is no wave motion at the region of torso behind the healthy lung (blue regions shown in the velocity contours).

2.8 Limitation of current study

Figure 7 and figure 37 (Appendix B) present a comparison of the Frequency Response Function (FRF) variation with mechanical frequency. While Fig. 7 presents the variation of the FRF in the form of Average and Average + 1 Standard Deviation for the experimental study, Fig. 37 presents variations for all the 3 healthy human subjects (dashed curves) as compared to the computational study. From fig. 37 it is observed that the experimental variations are closer to the computational (ideal) curves for the measurements made on the left side of the torso posterior, while the measurements made on the right side of the torso posterior show deviation from the computational curve. This is due to the fact that the human subjects were asked to hold their breath still while the measurements were being made by the SLDV (fig. 1), first on the left side, followed by the right side of the torso posterior. HS #1 and #2 were unable to hold their breath while measurements were being made on the right side of the torso posterior, thereby leading to measurements that had

contributions made by an unsteady posture and movements made by the human subjects. In the future, due to the advancements made in SLDV acquisition technology, it would be possible to simultaneously measure mechanical motion at all the 48 points on both left and right sides of the torso posterior, therefore leading to a better match between the experimental measurements and computational simulation.

3. 1-NORM: A NOVEL WAVEFORM ANALYSIS TECHNIQUE TO QUANTIFY THE DEGREE OF MECHANICAL INHOMOGENEITY OF VISCOELASTIC MATERIALS

Note: This chapter contains my own work, which was published in the Journal of Mechanical Behavior of Biomedical Materials [2]. Text, figures and results from our journal publication have been used in this dissertation after obtaining the necessary copyright permission from the publisher (please refer to Appendix C for license agreement).

3.1 Introduction

Magnetic Resonance Elastography (MRE) is a non-invasive diagnostic technique that enables a quantitative estimation of the viscoelastic properties of biological tissue [47]. Prior studies have used this technique to estimate the viscoelastic parameters of soft biological tissues such as liver [48], [49], skeletal muscle [50], [51], heart [13], [52], brain [53], [54], and other tissues [11], [55]–[57]. The primary goal of this investigation is to develop and experimentally validate 1-Norm, a Fourier-transformation based technique that can be used to quantify the magnitude of mechanical wave scattering caused due to the mechanical property inhomogeneity in biological tissues such as in skeletal muscle, the brain (due to white matter tracts), as well as due to the presence of neurodegenerative disease (such as Alzheimer’s disease (AD)), or due to injury, such as damage to skeletal muscle fascicles. The second goal of this study is to propose the 1-Norm as an alternative technique to determine the mechanical property inhomogeneity of a biological tissue based on wavefront analysis, rather than using traditional wave inversion technique (to compute the stiffness), as these inversion techniques are ill-posed. In the current work, the investigator demonstrates the validity, relevance and capability of 1-Norm to be able to detect an increase in the degree of mechanical inhomogeneity of mouse brain (5xFAD species) due to the presence of neurodegenerative disease, accompanied with a reduction in the brain stiffness (demonstrating an

agreement with the findings of a similar study performed on human subjects by Majumdar et al [58]).

In addition, 1-Norm is also used to quantify the effects of freezing and thawing on the mechanical property inhomogeneity of excised biological tissues (porcine kidneys, porcine liver and porcine lumbus muscle) due to a freeze-thaw cycle, accompanied with a reduction in tissue stiffness, a finding which is in agreement with the results of a prior work [59] which demonstrated a reduction in tissue stiffness of ex vivo rat liver due to freezing and thawing. This demonstrates the capability of 1-Norm to determine the degree of mechanical inhomogeneity of excised biological tissues, paving a way for 1-Norm as an alternative MRE-based biomarker to stiffness, which relies on ill-posed wave inversion.

3.1.2 Literature review

Muscle fibers are one of the building blocks of skeletal muscle and occur as uniformly spaced, spatially distributed structures that group together to form a muscle fascicle. Several such fascicles combine together as a bundle to form the skeletal muscle. The skeletal muscle is connected to the bone through connective tissues called tendons. On a microscopic scale, epimysium and perimysium are the connecting tissue layers that surround a group of 10 to 100 muscle fibers and separate them into fascicles. The skeletal muscle is therefore inhomogeneous and possesses directional anisotropy because of the presence of a predominant direction along the muscle fibers [60].

Some of the prior work has assumed mechanical properties of the bulk skeletal muscle to be homogeneous and anisotropic [14], [61]–[63]. This assumption is reasonable at a macroscopic scale. A single strand of muscle fiber measures 10-100 μm in diameter and up to 100 mm in length [60] and thus at a microscopic level it is necessary to consider each of these muscle fibers as a

structural inhomogeneity that is uniformly distributed inside a homogeneous medium (that is, the connective tissue). Qin et al [64] modeled the inhomogeneity and directional anisotropy by constructing phantoms that used a “bundle” of spandex (elastane) fibers dispersed in a viscoelastic medium of Polyvinyl Alcohol (PVA). However, muscle fibers are not stacked as a single bundle and a better model would be one that is composed of uniformly distributed “inhomogeneities” dispersed in a homogeneous medium. The present study therefore uses 3D-printed anisotropic fiber phantoms that have a controlled distribution of uniformly spaced fibers of equal diameter and possessing known material properties.

Based on an observation of the contours of displacement of propagating mechanical waves in a 3D printed fiber phantom, the investigator notes that the presence of fibers not only causes an elongation of the waves in the direction of the fibers, but also causes a scattering effect at the locations of fiber intersection. This represents a coupled scenario in which directional anisotropy is superimposed with inhomogeneity. The authors thus use FEA as a tool to decouple the effects of directional anisotropy from those of inhomogeneity. This is achieved by modeling and analyzing finite element phantoms that have uniformly spaced spherical inclusions dispersed throughout a homogeneous matrix as described in section 3.

3.1.3 Objective of the investigation

1-Norm is proposed as a measure to quantify the magnitude of wave scattering due to the presence of inhomogeneities. The specific aims of this study are, firstly, to develop a technique capable of quantifying the magnitude of wave scattering due to the presence of inhomogeneities in a medium; secondly, to apply and validate this technique on a 3D printed phantom containing carefully oriented fibers, and confirm these results using FEA applied to inhomogeneous phantoms containing symmetrically spaced spherical inclusions. Both of these scenarios include utilizing a

pre-determined microstructure (arrangement) of inhomogeneities and have known material properties, thereby enabling easier visualization and accurate interpretation of the results. The third and final aim of this study is to extend the application of 1-Norm technique to actual biological tissues including an excised porcine lumbus muscle sample and an excised bovine liver specimen. This third aim also encompasses a demonstration of the validity and relevance of the 1-Norm waveform analysis technique in being able to detect and quantify the change in the degree of mechanical inhomogeneity of a biological tissue due to temperature change, such as due to freezing, and due to neurodegenerative disorder (Alzheimer's disease). Using the current work we hope to be able to prove the reliability of 1-Norm as a quantitative 'marker' of degree of inhomogeneity of a tissue, and as an alternative MRE-based biomarker to stiffness, which relies on ill-posed wave inversion. The investigation demonstrates that 1-Norm can not only sense a change in the mechanical inhomogeneity of these aforementioned excised biological tissues, but 1-Norm can also be used as an alternative to wave-inversion techniques (computation of stiffness) which are ill-posed, as discussed in the next chapter.

3.1.4 Significance of the investigation

MRE is a clinically proven and a well-established non-invasive method that involves estimating the stiffness of biological tissues in vivo to assess the influence of disease on the tissue mechanical properties [65]. However, current methods involve use of wave inversion to estimate the tissue stiffness, and wave inversion techniques are ill-posed, meaning that the solution to the inverse problem is non-unique and is unstable, owing to its sensitivity to initial conditions. 1-Norm is not only proposed as a mathematical quantifier of the degree of mechanical inhomogeneity of biological tissues, but, in addition, 1-Norm is also proposed as a novel alternative MRE-based biomarker to stiffness, which relies on ill-posed wave inversion (in Chapter 4) achieved by

demonstrating a correlation between the values of 1-Norm (signifying wave scattering due to the presence of inhomogeneity) and tissue stiffness, during neurodegenerative disorder and due to freezing and thawing.

3.1.5 Clinical relevance of 1-Norm

While still at a nascent pre-clinical stage, the investigator believes that the 1-Norm wave-scattering technique has the potential to serve as a biomarker in detecting the presence and in staging the severity of neurodegenerative diseases and disorders that lead to an increase in tissue inhomogeneity (such as primary sclerosing cholangitis (PSC) of the liver). At its current stage, 1-Norm has been shown to be sensitive to microscopic changes in tissue inhomogeneity. The 1-Norm technique represents an alternative MRE-based biomarker to stiffness, which relies on ill-posed wave inversion. It is noted that further studies including histopathology and in vivo experimentation are needed to shed light on the microscale causes of mechanical property inhomogenization in due to diseases such as AD and PSC.

3.2 Theory

3.2.1 Wave propagation in a viscoelastic continuum

The mechanical behavior of soft biological tissues such as liver, brain white matter and skeletal muscle is viscoelastic. This implies the presence of viscous damping which is mathematically accounted for by the imaginary term of the complex shear modulus when expressed in the frequency domain. Under the assumptions of local homogeneity and isotropy the wave equation of a viscoelastic compressible medium can be written as [66]:

$$\rho \frac{\partial^2 \vec{u}(r,t)}{\partial t^2} = (\lambda + \mu) \nabla \nabla \cdot \vec{u}(r,t) + \mu \nabla^2 \vec{u}(r,t) \quad \dots (3.1)$$

In eq. (1), λ and μ are the Lamè parameters; λ relates to volumetric compressibility of the medium while μ denotes the shear modulus. Also used in eq. (3.1) are other parameters such as the density of the medium (ρ), the displacement vector \vec{u} , and the nabla operator ∇ . Application of a Fourier transform to eq. (3.1) leads to the wave equation in the frequency domain:

$$-\rho\omega^2\vec{U}(r, \omega) = [G_L(r, \omega) + G_S(r, \omega)]\nabla(\nabla \cdot \vec{U}(r, \omega)) + G_S(r, \omega)\nabla^2\vec{U}(r, \omega) \quad \dots (3.2)$$

In eq. (3.2), G_L and G_S are the complex modulus of the first (λ) and second (μ) Lamè parameter, respectively and $\omega(=2\pi f)$ corresponds to the angular mechanical frequency (in radians per second), while f is the mechanical frequency in Hertz. Assuming the medium to be incompressible, that is,

$$\nabla \cdot \vec{U}(r, \omega) = 0 \quad \dots (3.3)$$

Considering only out-of-plane displacements ($U = U_z$) reduces equation (3.2) to

$$-\rho\omega^2\vec{U}(r, \omega) = G_S(r, \omega)\nabla^2\vec{U}(r, \omega) \quad \dots (3.4)$$

A rearrangement of the terms in eq. (3.4) leads to the scalar Helmholtz equation:

$$G_S(r, \omega) = -\frac{\rho\omega^2\vec{U}(r, \omega)}{\nabla^2\vec{U}(r, \omega)} \quad \dots (3.5)$$

The term on the left-hand-side of eq. (3.5) is the complex-valued shear modulus of the material, which is a function of the mechanical frequency (f). MRE observes shear wave propagation inside a material medium with shear wave velocity (c) defined as [53]:

$$c(\omega) = \frac{1}{\text{Re} \sqrt{\rho/G_S(r, \omega)}} \quad \dots (3.6)$$

Further, the length of the shear wave λ is related to the velocity c and to the mechanical frequency f by:

$$\lambda = \frac{c(\omega)}{f} \quad \dots (3.7)$$

The present work uses a geometric focusing technique [67] in order to introduce radially converging wave motion inside a material medium. This type of a converging wave pattern compensates for the damping inside the medium. For this technique to be applicable, the sample needs to have a cylindrical outer surface, with the mechanical excitation being applied at the circumference of the sample in a direction perpendicular to the plane of the circumference. In this manner the wave front decays gradually, thereby concentrating the wave energy on a smaller surface and compensating for the loss of wave amplitude due to attenuation.

3.2.2 Magnetic Resonance Elastography (MRE)

Magnetic Resonance Elastography (MRE) involves application of mechanical excitation to a sample while simultaneously introducing an oscillating magnetic field gradient, resulting in a phase accumulation in the complex-valued MRI image [68], [69]. This phase accumulation (θ) at a given location is given by:

$$\theta(\vec{r}, s) = \gamma \int_s^{s+\Delta t} \vec{G}(t) \cdot \vec{u}(\vec{r}, t) dt \quad \dots (3.8)$$

In the eq. (3.8) above, γ is the gyromagnetic ratio, $\vec{G}(t)$ is the time dependent magnetic field gradient vector and $\vec{u}(r, t)$ is the time and space dependent displacement vector. The phase accumulation as described in the eq. (3.8) above results in a single snapshot of mechanical wave propagation. Several such snapshots, implemented by shifting the start of the magnetic field gradient over the period of the vibration, provide MR phase images that correspond to the

mechanical wave propagation. These MR phase images can then be used to compute the complex wave images $U(r, \omega)$ and subsequently the complex shear modulus $G(r, \omega)$ [70].

3.2.3 Introduction to 1-Norm

The basis of introducing the 1-Norm technique is the observation that the wave fronts in an anisotropic fiber phantom show a pattern of scattering at the location of fiber intersections. This pattern of scattering can be quantified by measuring the distance of each point on the delineated wave front from the center of the specimen. The wave front can then be expressed as a function r over ϕ in polar coordinates as illustrated in fig. 15 and subsequently a 1D discrete Fourier transform is applied along ϕ to obtain a frequency spectrum. The 1-Norm corresponds to the sum of Fourier components (absolute value) of harmonic #7 up to harmonic #n/4.

Units of 1-Norm: 1-Norm is a normalized length unit.

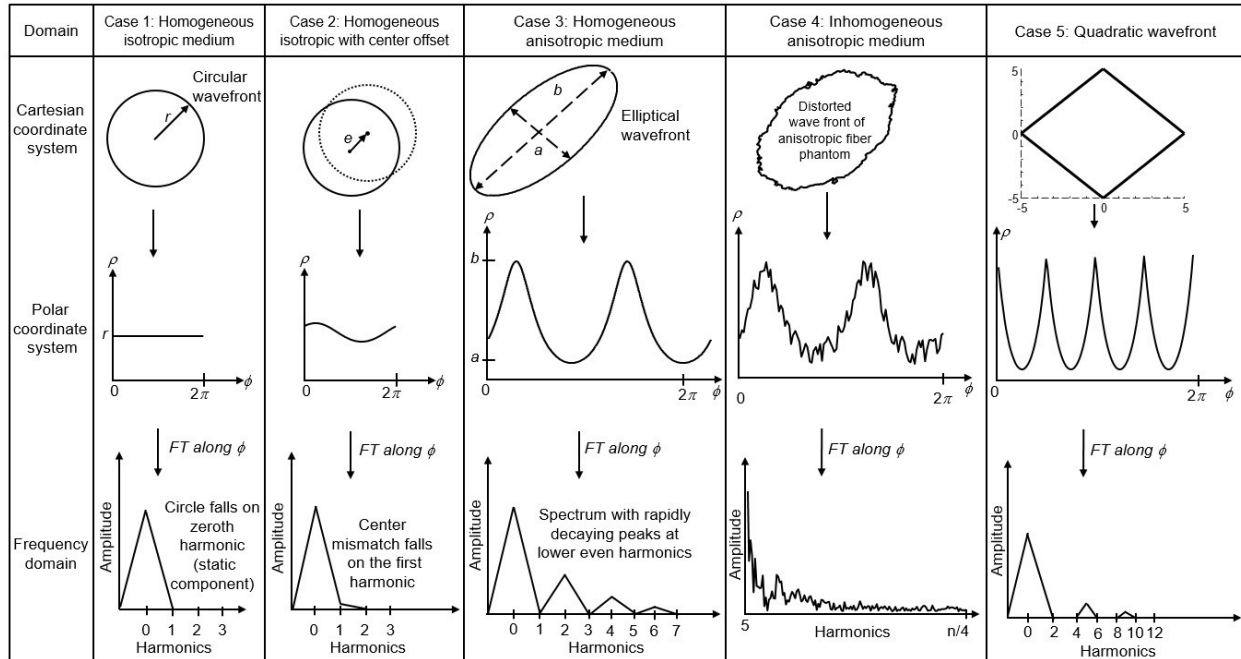


Figure 15. Schematic diagram depicting the technique of 1-Norm being applied to: **Case 1:** A homogeneous isotropic medium; **Case 2:** A homogeneous isotropic medium with a center mismatch; **Case 3:** A homogeneous anisotropic medium; **Case 4:** Wavefront from MRE

experimental data on 3D printed anisotropic fiber phantom and **Case 5:** Quadratic wavefront from MRE experiments on ex vivo porcine lumbus muscle.

From fig. 15, it is observed that:

- **Case 1:** The wave shape for an ideal homogeneous and isotropic material medium is a perfect circle. A circle appears as a straight line in polar coordinates and, consequently, the circle falls on the zeroth harmonic (static component) of the wave front spectrum;
- **Case 2:** An ideal homogeneous and isotropic medium, having a circular contour but with a moderate center offset (eccentricity) leads to a peak on the first harmonic (due to the center mismatch). The investigator notes that the contributions of other harmonics are negligible for moderate center offsets. These contributions are only measurable when the origin is closer to the circular wavefront.
- **Case 3:** For a medium consisting of directional anisotropy, for example, due to the presence of fibers, the wave fronts experience an elongation in the direction of the fibers, thereby causing the wave front to take the shape of an ellipse. As shown in fig. 15, an ellipse falls on even harmonics of wave front spectrum upon application of polar coordinate transformation and Fourier transform along ϕ ; however, the spectral values are rapidly decaying for higher harmonics and already negligible at harmonic # 6.
- **Case 4:** Actual data obtained from Magnetic Resonance Elastography experiments on soft biological tissues display wave fronts that depict scattering effects (in addition to potential elongation due to directional anisotropy). These deviations appear on the higher harmonics of the frequency spectrum (typically on the 7th and higher harmonics).

- **Case 5:** Quadratic wavefront obtained from MRE experiments on ex vivo porcine lumbus muscle tissue that was non-circular in shape. The contributions of non-circular (quadratic) wavefront are confined to lower harmonics (up to 5). The shape of the ex vivo porcine lumbus muscle sample has no effect on the values of 1-Norm, as lower harmonics (up to 6) are ignored in the definition of 1-Norm.

The investigator notes that a center mismatch of circle or ellipse, as can occur during wave front assessment of experimental data, falls on the first harmonic of the wave front spectrum. Additionally, wave front scattering is not represented by spectral values of harmonics $\#N/4$ and higher, where N is the number of (evenly spaced in terms of ϕ) samples of $r(\phi)$. These harmonics rather reflect contour line noise that occurs even without the presence of scatterers (these two observations were made in pre-tests and are not illustrated in figure 15).

3.3 Method

Magnetic Resonance Elastography (MRE) experiments were performed on a 3-D printed inhomogeneous gelatin-based phantom consisting of a precisely controlled microstructure. A custom-built experimental set-up was designed that generated shear waves that were polarized perpendicular to the fibers and that propagated in the plane in parallel to the fibers. These experiments were followed by ex-vivo MRE experimentation on porcine lumbus muscles in order to be able to demonstrate the feasibility and applicability of 1-Norm on native skeletal muscle. In addition to MRE, Finite Element Analysis (FEA) simulations were performed in order to decouple the effects of directional anisotropy (imposed by the fibers) from the effects of scattering (observed at the locations of intersection of fibers). The following subsections describe the implementation of each of these steps in detail.

3.3.1 MRE on 3D printed fiber phantom

Preparation of inhomogeneous fiber phantom: An inhomogeneous fiber phantom was constructed using a two-step procedure as previously described [71], [72]. Briefly, 15% w/v gelatin (porcine type A, Sigma-Aldrich) was maintained at 31 °C and 3D-printed out of a 200 µm diameter nozzle layer by layer onto a 10°C cooled stage using a commercial 3D printer (EnvisionTEC GMBH 3D Bioplotter). Anisotropy of the overall phantom (in the macroscale) was accomplished by 3D-printing struts so that the x-distance between adjacent struts was 1 mm, while the y-distance between adjacent struts was 1.8 mm. In the second step, the 3D printed structure was cross-linked by incubating it in a solution of 15 mM EDC (1-ethyl-3-(3-dimethylaminopropyl) carbodiimide) (Sigma-Aldrich) and 6 mM NHS (N-Hydroxysuccinimide) (Sigma-Aldrich) for 1 hour. Structures were then washed repeatedly in deionized water to remove residual cross-linker. The cross-linked 3D printed phantom was then punctured with a custom-made 8 mm diameter steel biopsy punch to trim it to appropriate dimensions.

Separately, a soda glass tube with 8.2 mm outer diameter and 10 cm in length was machined to have smooth opening at both the ends. One end of the tube was sealed using laboratory parafilm (BEMIS®, Wisconsin, USA), then tightly capped using modeling clay (Crayola Modeling Clay, Pennsylvania, USA) and placed in an upright position. A 37°C solution of 5% w/v water-based gelatin was carefully poured into the glass tube until it filled about one-half the length of the tube. The cross-linked structure was then carefully placed into the tube. After achieving the desired orientation of the fibers, the glass tube was topped up with a lukewarm solution of 5% w/v gelatin to ensure the 3D printed structure was completely immersed inside the gelatin medium. Cross-linking enhanced the stiffness and stability of the 3D printed structure thereby preventing it from being dissolved when immersed in the surrounding 5% gelatin. The parafilm and clay seal at the

bottom of the glass tube was removed prior to the experimentation so that the tube remained open at both the ends in order to prevent a reflection of waves at this end.

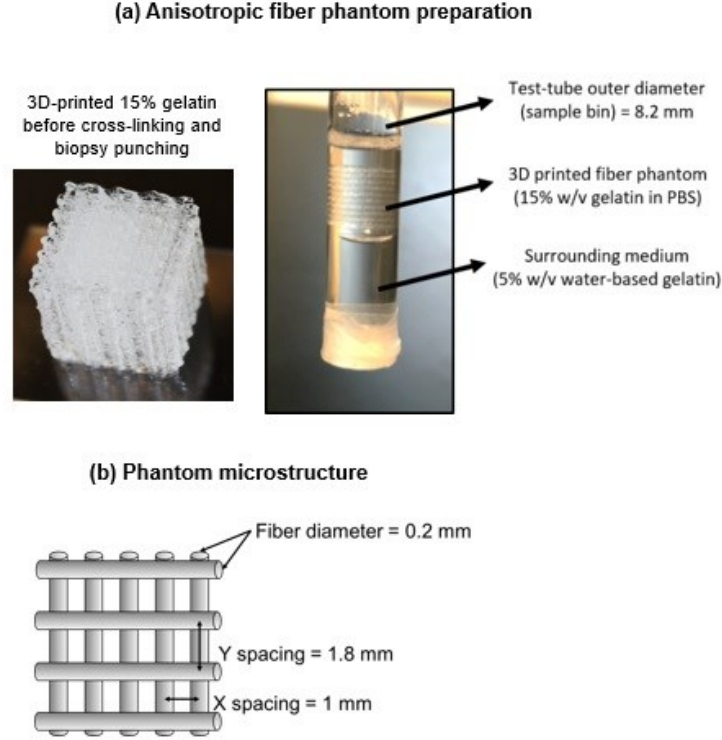


Figure 16. The 3-D printed anisotropic fiber phantom (placed inside a borosilicate glass test tube) and surrounded by gel medium **b.** Microstructure of the 3-D printed anisotropic fiber phantom

Experimental set-up: As MRE involves application of harmonic vibration to the sample in conjunction with MRI, a custom-built experimental set up was used [73] in order to simultaneously grip the sample in a vertical position and apply a harmonic excitation as shown schematically in fig 17. Experiments were performed on a Bruker 11.7 T MRI scanner having a 56-mm vertical bore, a 19 mm gradient coil (with a maximum strength of 3000 mT/m) and a 10 mm diameter radiofrequency coil. As shown in the fig. 17 below, a “trigger signal” from the MRI pulse sequence prompted the wave form generator (33220A Function/Arbitrary Waveform Generator, 20 MHz,

Agilent Technologies Test and Measurement, Englewood, CO) to produce an electrical signal, that was then amplified by a power amplifier (P3500S Power Amplifier, Yamaha Corporation of America, Buena Park, CA). A Direct Current bias (not shown in the fig. 17) was added to the output of the power amplifier through a series connection of a constant DC power supply unit (E3634A 200W Power Supply, Agilent Technologies Test and Measurement, Englewood, CO). The usage of this DC voltage bias ensured positive-valued voltage oscillations across the terminals of the piezoelectric device, so as to preserve its mechanical integrity.

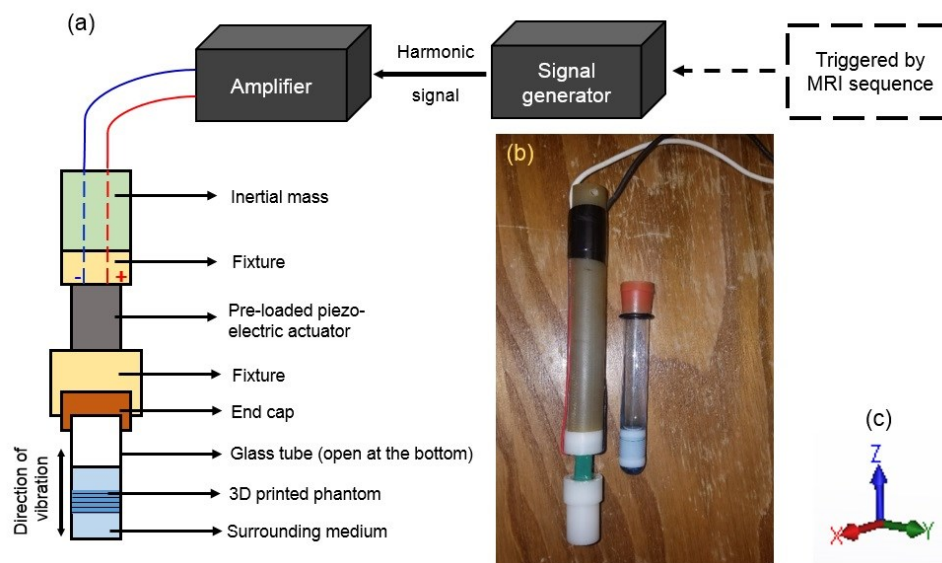


Figure 17. Schematic diagram of the experimental set-up used in Magnetic Resonance Elastography experiments on the 3D printed fiber phantom (representational diagram; not to scale) **b.** Picture of the piezoelectric actuator (on left) and test-tube sample (on the right) **c.** Orientation of the coordinate system

An “MRI-safe” piezoelectric actuation device (Thor Labs Inc.) measuring 6.5 x 6.5 x 18 mm and with a capability to provide a maximum mechanical displacement of 11.6 microns at 100 V was used in this study. Of importance was the inertial mass connected to one end of the piezoelectric

actuator: this inertial mass acted as a mechanical grounding that provided a reaction force to the piezoelectric actuator thereby making it capable of providing a mechanical motion to the sample.

MRE experiment parameters (Bruker 11.7 T vertical bore MRI system): A gradient echo based pulse sequence [73] was used for MRE experiments, with relevant parameters being: Acquisition matrix = 128 x 128, field of view = 10 mm x 10 mm, slice thickness = 1 mm, flip angle = 30 degrees, repetition time = 100 ms, echo time = 3.95 ms, MEG strength = 1200 mT/m, eight time steps. Experiments were performed at frequencies of 2, 3 and 5 kHz. Separate MRE experiments (using the same pulse sequence and parameters as listed above) were performed on a homogeneous 10% w/v water-based homogeneous and isotropic gelatin phantom and the results thus obtained were used to compare and contrast the nature of wave propagation observed inside the 3D printed inhomogeneous fiber phantom against the homogeneous 10% w/v water-based gelatin phantom.

MRE experiment data processing: The data obtained from MRE experiments was analyzed using Matlab (Mathworks Inc., Natick, MA). The Fourier transform was used to convert the phase difference wave images (in time domain) to complex wave images in the frequency domain at frequencies of 2, 3 and 5 kHz. At each of the frequencies, the real part of the complex shear wave displacement image was visualized and the '*contour*' command in Matlab was used to identify and delineate the profiles having zero displacement of shear waves. The delineated contour profiles at each of the frequencies were selected so as to be at the same distance from the outer edge of the bin. The coordinate positions (in Cartesian coordinate system) of each of the points located on these contours were transformed into polar coordinates. The polar coordinates of each of the points on the delineated profile were used to compute the distance from the geometric center of the wave image and sorted in to a dataset. This data set was used to generate a frequency spectrum using a

discrete spatial Fourier transform in Matlab. A numerical value for 1-Norm was obtained using a summation of absolute values of Fourier transform of these harmonics, higher than 6. The static component and the first four harmonics that show contributions due to center mismatch, the circle or the ellipse were discarded in the calculation of the 1-Norm (see fig. 1). A comparison of the 1-Norm values for the homogeneous 10% w/v water-based gelatin phantom versus that of the 3D printed anisotropic fiber phantom are presented in section 4. A total of $n = 108$ points were used to compute the 1-Norm.

3.3.2 Finite element phantom model

Rationale for using Finite Element Analysis: The 3D printed inhomogeneous fiber phantom (as described in section 3.3.1) had fibers along both x and y directions (fig. 16), which resulted in shear waves being elongated along the direction of fibers in addition to scattering effects observed at the location of fiber intersection (due to inhomogeneities). While the directional effect was due to the anisotropy caused by the orientation of fibers, the scattering effect was due to the inhomogeneities at the locations of fiber intersections. As such, the 3D printed inhomogeneous fiber phantom exhibited a “coupled” scenario wherein directional anisotropy was superimposed upon inhomogeneity. The authors propose Finite Element Analysis [74] as a tool to model and investigate virtual phantoms that possess a controlled distribution of spherical inclusions (fig. 18) without the presence of fibers, effectively “de-coupling” the effects of directional anisotropy from those of inhomogeneity.

Three-dimensional modeling: As depicted in fig. 18 below, a three-dimensional solid model of the phantom containing spherical inclusions was developed using Solidworks 2017 (Dassault Systèmes, France). The phantom modeled in this study was 7.8 mm in diameter and 1 mm in height. Two circular arrangements of spherical inclusions, known as the outer ring and the inner

ring, each with a diameter of 0.5 mm, were modeled. Three cases were considered with respect to the spacing between the neighboring spherical inclusions on the outer ring, namely $d = 2.5$ mm (fig. 18 (b)), $d = 1.65$ mm (fig. 18 (c)) and finally $d = 1.25$ mm (fig. 18 (d)) respectively.

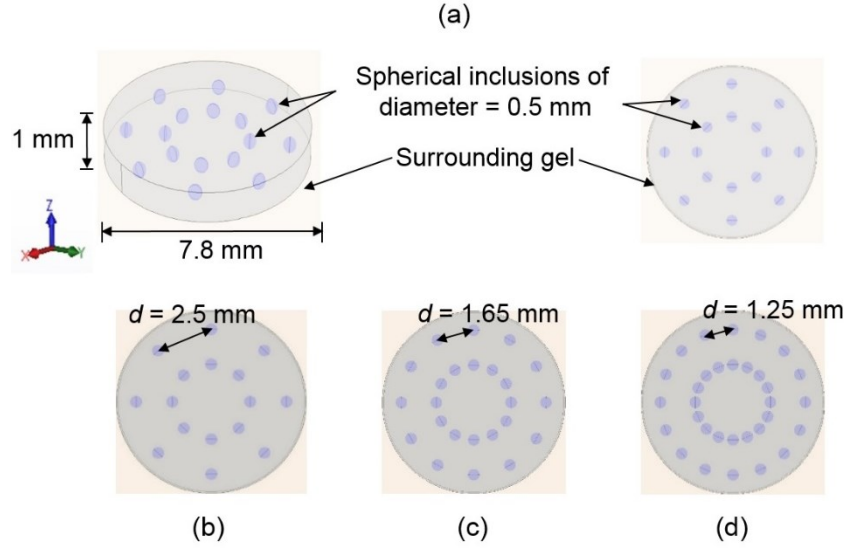


Figure 18. Finite Element Analysis (a) Three-dimensional modeling and orientation of spherical inclusions; (b) FE model with interstitial gap of $d = 2.5$ mm between neighboring spherical inclusions; (c) and (d): FE models used in additional investigations using reduced distance ($d = 1.65$ mm and $d = 1.25$ mm) between neighboring spherical inclusions

Mesh generation and boundary conditions: The three-dimensional solid model created using Solidworks was imported into Comsol (Comsol Group, Stockholm, Sweden) and discretized to create separate component level entities for the spherical inclusions as well as the surrounding medium, in order to enable easier selection of individual components. Tetrahedral elements were used to mesh the model. The meshed model had 807827 elements. A harmonic displacement of 11.6 micrometers (in z-direction, as shown in fig 18) was applied at the external surface of the outer medium in order to simulate harmonic excitation from a piezoelectric actuator in an actual MRE experiment. A boundary condition of equal radial displacement was imposed on the boundary nodes of the spherical inclusions at the locations where they were in contact with the

nodes of the matrix. Finite element simulations were performed at frequencies of 1, 2, 3, 4 and 5 kHz for both homogeneous (5% w/v water-based gelatin) phantom as well as the phantom containing spherical inclusions.

Material properties: Table 3 lists the material properties used for the surrounding medium (5% w/v water-based gelatin) as well as for the spherical inclusions (20% w/v water-based gelatin). The values of shear modulus were obtained by rheometry (Modular Compact Rheometer (MCR) 302, Anton Paar GMBH, Virginia, United States). In addition, density and bulk modulus were assumed to be those of water, as shown in Table 3. Using a 5% w/v water-based gelatin as the surrounding medium and 20% w/v water-based gelatin for the spherical inclusions resulted in a large difference in their material properties, which then provided for a distinct visualization of the scattering effects.

Table 3. Material properties used in Finite Element Analysis

Surrounding gel (5% w/v water-based gelatin)	Spherical inclusions (20% w/v water-based gelatin)
Shear modulus = $5.74 + 3.29j$ kPa	Shear modulus = $27.35 + 7.92j$ kPa
Density = 1000 kg/m^3 ; Bulk modulus = 2150 MPa	Density = 1000 kg/m^3 ; Bulk modulus = 2150 MPa

Post processing: Contours of shear wave displacement (in the z-direction) were obtained from Comsol for a single central slice at an axial location at the center of the plane containing the spherical inclusions (at $z = 0$). These data points (containing x and y coordinates as well as the shear wave displacement) were formatted into a 128 x 128 data matrix of equispaced x and y coordinates and exported to Matlab (Mathworks Inc., United States) for further processing. The approach described in section 3.3.1 was used to delineate the contours of zero displacement at each of the frequencies of interest (1, 2, 3, 4 and 5 kHz) for both the homogeneous finite element

phantom (5% w/v water-based gelatin) as well as the finite element phantom containing spherical inclusions. A total of $n = 108$ points were used in the computation of the 1-Norm.

3.3.3 MRE on excised porcine lumbus muscle (Agilent 9.4 T preclinical MRI system)

MRE experiments were performed on an excised porcine lumbus muscle in order to demonstrate the feasibility and application of the concept of the 1-Norm on native muscle tissue.

Sample preparation: A slice of porcine lumbus muscle was obtained from a local butcher. Prior to the experiment, the slice was trimmed to the dimensions shown in the fig. 19 below so as to eliminate regions of fat tissue to avoid artifacts during the acquisition of MR images.

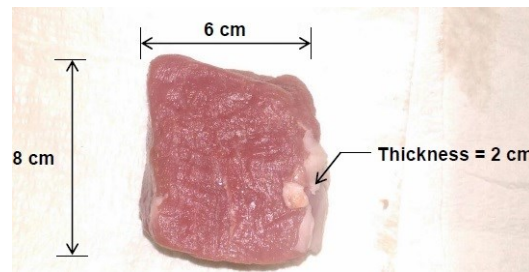


Figure 19. Dimensions of the ex-vivo porcine lumbus muscle used in Magnetic Resonance Elastography experiments. Muscle fibers are oriented in the direction perpendicular to the plane of the image, which is also the direction of mechanical vibration.

Experimental Setup: A custom-designed sample holding cup with an outer diameter of 6.4 cm, a wall thickness of 0.3 cm and a height of 8.5 cm, made of polyester (Polylactic Acid) was 3-D printed in the lab. This cup provided a mechanical excitation through a preloaded piezoelectric actuator device (P-840.10 Physik Instrumente, Massachusetts, United States) connected to the closed end of the cup as shown in fig. 20 below. The muscle sample was wrapped inside several layers of water-resistant paper in order to ensure a tight fit inside the sample holding cup, while simultaneously preventing any leakage of fluids from the muscle sample into the MRI system.

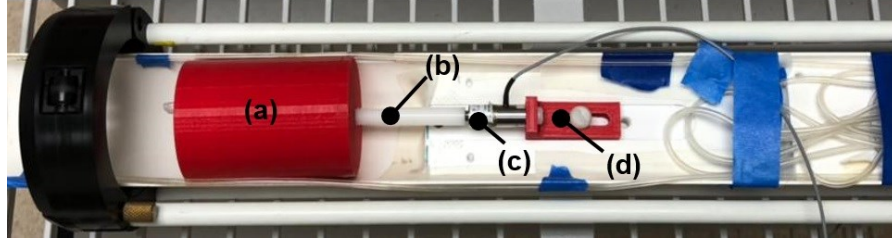


Figure 20. Apparatus used in MRE experimentation of an ex-vivo Porcine Lumbar muscle. (a) Cylindrical excitation cup used as sample holder with an outer diameter of 6.4 cm and a height of 8.5 cm; (b) connecting rod made of Delrin, with a diameter of 1 cm and a length of 6.2 cm; (c) Pre-loaded piezo electric actuator and (d) inertial coupling of the rear end of the piezo to the supporting structure

Experiments were performed on an Agilent 9.4 T horizontal bore MRI scanner, using a gradient coil with an inner diameter of 120 mm and an RF coil with an inner diameter of 72 mm. The electrical connections used in this study were identical to those used in the MRE experimentation on the 3D printed inhomogeneous phantom, with the only difference being in the orientation of the sample, due to the horizontal bore of the Agilent 9.4 T MRI system.

MRE experimentation parameters: A spin-echo based MRE pulse sequence was used with the following relevant sequence parameters: pulse repetition time = 1000 ms, echo time = 13.874 ms, field of view = 64 mm x 64 mm, slice thickness = 1 mm, acquisition matrix = 64 x 64, number of slices = 20, eight time offsets with two acquisitions each (inverted MEG polarity) for phase difference calculation and an MEG strength of 396 mT/m. The MEG frequency was matched to the mechanical frequency. Experiments were performed at 500 Hz, 600 Hz, 800 Hz and 1000 Hz.

Data processing: Data obtained from MRE experiments was analyzed in Matlab (Math-Works, Inc., Natick, MA) using an approach similar to the one highlighted in section 3.3.1. Fourier transform was used to convert the phase difference wave images to complex wave images in the frequency domain. In addition, 2D phase unwrapping (Flynn algorithm) was applied to the data at frequency of 500 Hz and 600 Hz [75]. A central slice was selected for data analysis and

computation of 1-Norm. At each of the frequencies (500 Hz, 600 Hz, 800 Hz and 1000 Hz), contour lines of zero displacement were delineated using the ‘*contour*’ command in Matlab and were processed using the technique highlighted in section 3.3.1 in order to compute the 1-Norm. Section 3.4 presents the results in terms of contours of shear wave displacement, frequency spectra as well as the values of 1-Norm. The number of points on the delineated profiles varied between 130 and 152. All profiles were interpolated to $n = 108$ samples in order to compute the wave spectra and 1-Norm.

A note on the effect of shape of the ex vivo muscle sample on the values of 1-Norm: While the technique of 1-Norm presented in this study uses geometrically focused cylindrical wavefronts, in real life, the shape of an actual muscle tissue can be non-circular. As a worst case scenario the authors investigate the influence of a square wavefront on the values of frequency spectra as shown in fig. 21 below. The results of this comparison are presented in terms of ratios of amplitude of successively decaying harmonics on frequency spectrum and are presented in table 4 below. Similar to an elliptical wavefront, the spectrum of a square-shaped wavefront is primarily confined to lower harmonics with rapidly decaying peaks. Thus the values of 1-Norm (which by definition includes harmonics 7 and higher), are not affected by the shape of the muscle tissue used in the current study.

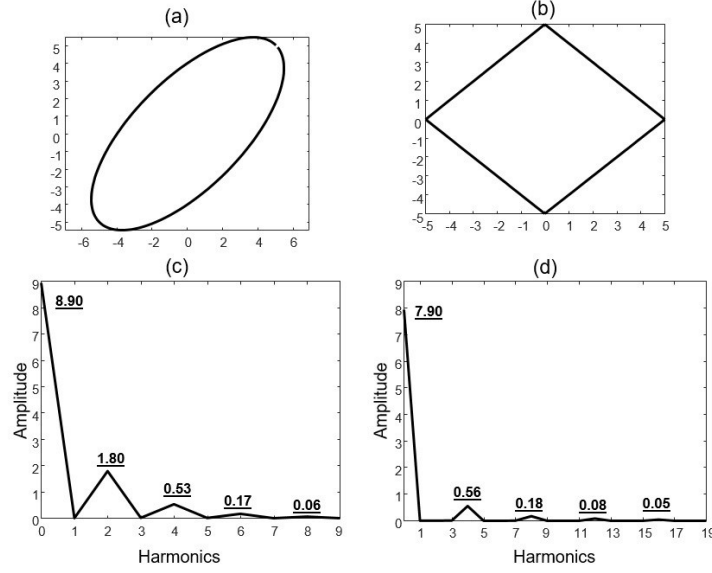


Figure 21. A comparison of (a) elliptical and (b) square shaped wave fronts along with the corresponding frequency spectra for (c) elliptical wavefront and (d) square wavefront. Both elliptical and square wavefronts exhibit rapidly decaying peaks at lower harmonics.

Table 4. Comparison of rapidness of decay of peaks on frequency spectra in terms of ratio of harmonics for:

(A) An elliptical wavefront

	Ratio of harmonics									
	$\frac{2^{nd}}{0^{th}}$	$\frac{4^{th}}{2^{nd}}$	$\frac{4^{th}}{0^{th}}$	$\frac{6^{th}}{4^{th}}$	$\frac{6^{th}}{2^{nd}}$	$\frac{6}{0^{th}}$	$\frac{8^{th}}{6^{th}}$	$\frac{8^{th}}{4^{th}}$	$\frac{8^{th}}{2^{nd}}$	$\frac{8^{th}}{0^{th}}$
Elliptical wavefront	0.2	0.3	0.06	0.3	0.1	0.02	0.3	0.1	0.03	6.7×10^{-3}

(B) A square wavefront

	Ratio of harmonics									
	$\frac{4^{th}}{0^{th}}$	$\frac{8^{th}}{4^{th}}$	$\frac{8^{th}}{0^{th}}$	$\frac{12^{th}}{8^{th}}$	$\frac{12^{th}}{4^{th}}$	$\frac{12^{th}}{0^{th}}$	$\frac{16^{th}}{12^{th}}$	$\frac{16^{th}}{8^{th}}$	$\frac{16^{th}}{4^{th}}$	$\frac{16^{th}}{0^{th}}$
Square wavefront	0.07	0.3	0.02	0.4	0.1	0.01	0.6	0.3	0.09	6.3×10^{-3}

3.3.4 MRE on excised bovine liver sample (Agilent 9.4 T preclinical MRI system)

As a continuation of the investigation, an excised bovine liver tissue was chosen as a second example in order to investigate the feasibility of the 1-Norm technique. Figure 22 (A, B) shows the steps involved in the preparation of the excised bovine liver tissue sample for MRE experiments. The liver sample was first cut into a circular shape (fig. 22 C) and carefully placed inside a cup that contained solidified 10% w/v water based gelatin filled upto one-half the length. After orienting the liver sample inside the cup, molten 10% w/v gelatin solution (at about 40 °C) was carefully poured so as to surround the tissue sample completely inside the gelatin medium. The medium was allowed to solidify at room temperature.

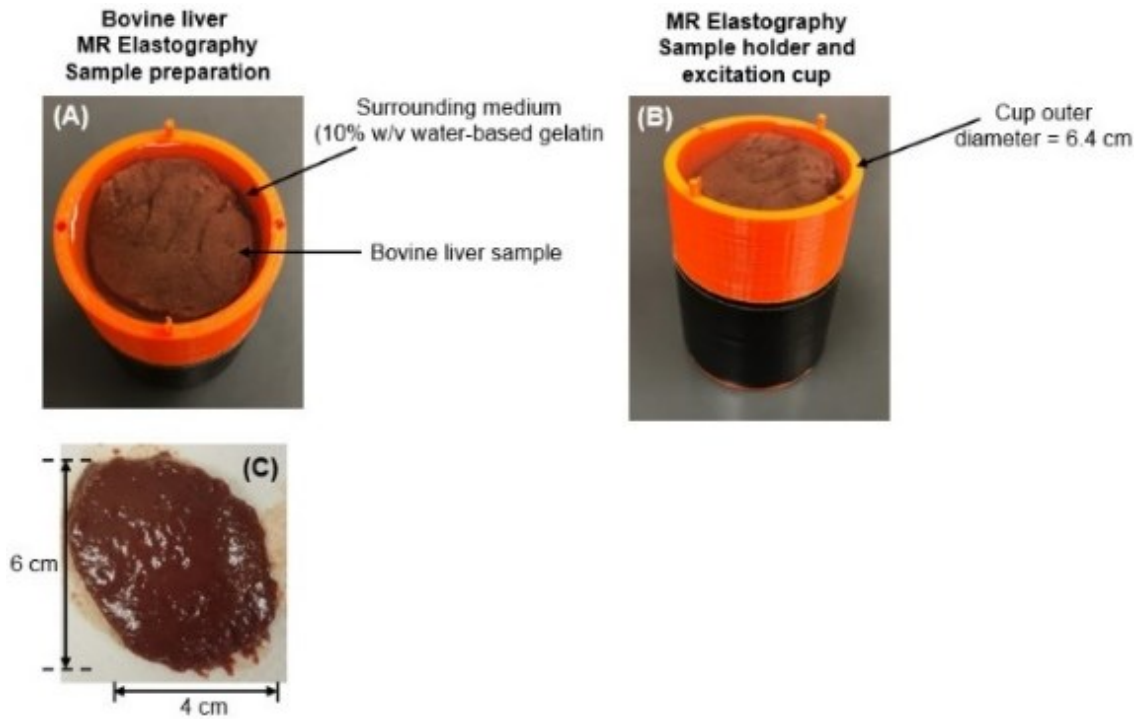


Figure 22. MRE on excised bovine liver sample. **(A) Sample preparation:** the bovine liver tissue was surrounded by 10% w/v water based gelatin medium in order to enable propagation of mechanical shear waves from the excitation cup into the sample. **(B)** Sample holder and excitation cup and **(C)** Dimensions of the liver sample used in the MRE study.

Experimentation parameters: Experiments were performed on a 9.4 T horizontal bore Agilent MRI system, using a spin echo sequence, with the following parameters: TR = 3s, TE = 0.051s, phase offsets = 8, FOV = 64 x 64 mm, no. of slices = 30, frequencies analyzed = 200 Hz and 300 Hz.

Data processing: The same data processing technique as described in the previous section for the porcine lumbus muscle sample, was used here.

3.4 Results

3.4.1 MRE experiments on 3D printed fiber phantom

Figure 23 and Table 5 summarize the results of MRE experimentation on the 3D printed inhomogeneous fiber phantom and compare those to a homogeneous 10% w/v water-based gelatin phantom of identical dimensions and with material parameters as the matrix of the fiber phantom. The spectra shown in fig. 23 B of the contours highlighted in fig. 23 A were used for the calculation of the 1-Norm, which are presented in table 5 A for both experimental phantoms.

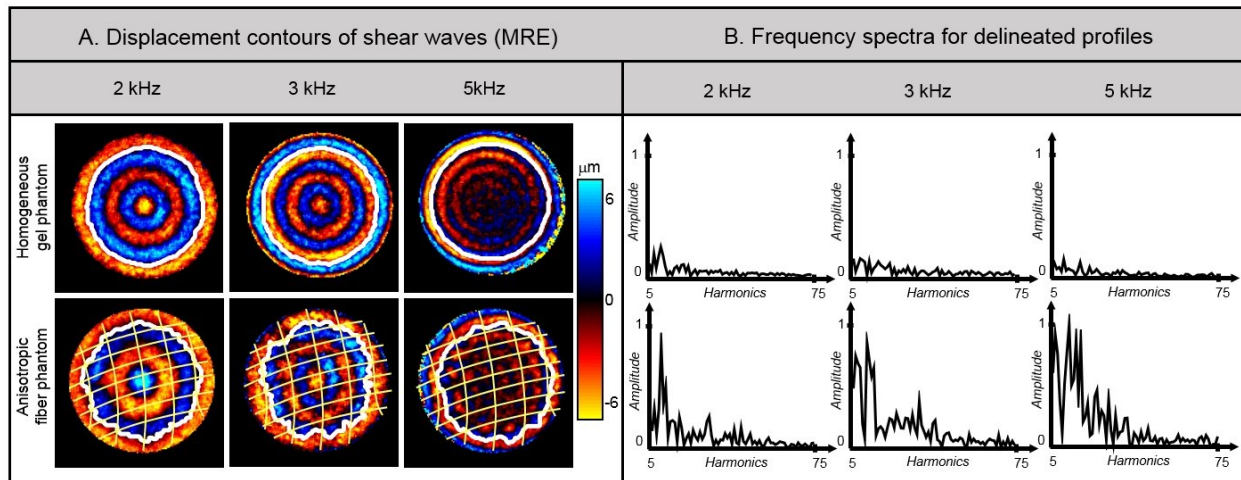


Figure 23. Results of MRE experiments on 3D printed fiber phantom.

(A) Phase images showing a comparison of shear waves (out-of-plane displacement) inside an experimental homogeneous, 10% w/v water-based gelatin phantom (top) versus a 3D printed

inhomogeneous fiber phantom (bottom) with the fibers highlighted in yellow and delineated contours of zero displacement highlighted in white. The presence of fibers causes scattering of waves and an elongation of the wave-fronts along the direction of fibers.

(B) Frequency spectra for the delineated contours (highlighted in white on the left-hand-side), obtained using a spatial Fourier transform for a homogeneous 10% w/v water-based gelation phantom (top) versus the 3D printed inhomogeneous fiber phantom (bottom). A shift of the spectrum towards higher harmonics is observed for the inhomogeneous fiber phantom due to increased scattering of the wave-fronts at fiber intersections.

Table 5. Summary of values of 1-Norm across various experiments (all computed using $n = 108$ points on the delineated contour)

A. 1-Norm values for MRE experiments performed on 3D printed anisotropic fiber phantom and compared against a homogeneous 10% w/v water-based gelatin phantom (column 2)

Frequency (Hz)	1-Norm for Homogeneous gel phantom	1- Norm for 3D printed fiber phantom
2000	2.2	6.9
3000	2.4	8.0
5000	2.9	10.2

B. 1-Norm values for FEA simulations performed on phantoms containing spherical inclusions and compared against a homogeneous FEA simulated phantom (column 2)

Frequency (in Hz)	1-Norm (Homogeneous FEA Phantom)	1-Norm for Inhomogeneous FEA phantom with spherical inclusions		
		Center-to-center distance between inclusions $d = 2.5$ mm	Center-to-center distance between inclusions $d = 1.65$ mm	Center-to-center distance between inclusions $d = 1.25$ mm
1000	0.04	0.5	0.2	0.1
2000	0.08	0.7	0.5	0.1
3000	0.2	1.8	1.6	1.0
4000	0.4	2.7	2.4	1.9
5000	0.7	3.0	2.6	2.2

C. 1-Norm values for MRE experiments performed on ex vivo porcine lumbus muscle tissue

Frequency (Hz)	1-Norm for ex vivo porcine lumbus skeletal muscle
500	1.6
600	2.1
800	2.3
1000	2.5

3.4.2 FEA on phantoms with uniformly spaced scatterers

Figure 24 shows the contour lines of zero displacement for varying interstitial distances (d) between the spherical inclusions, as a function of the mechanical frequency. The frequency spectra of the contour lines shown in fig. 24 are illustrated in fig. 25 and table 5B (on previous page) presents the values of 1-Norm.

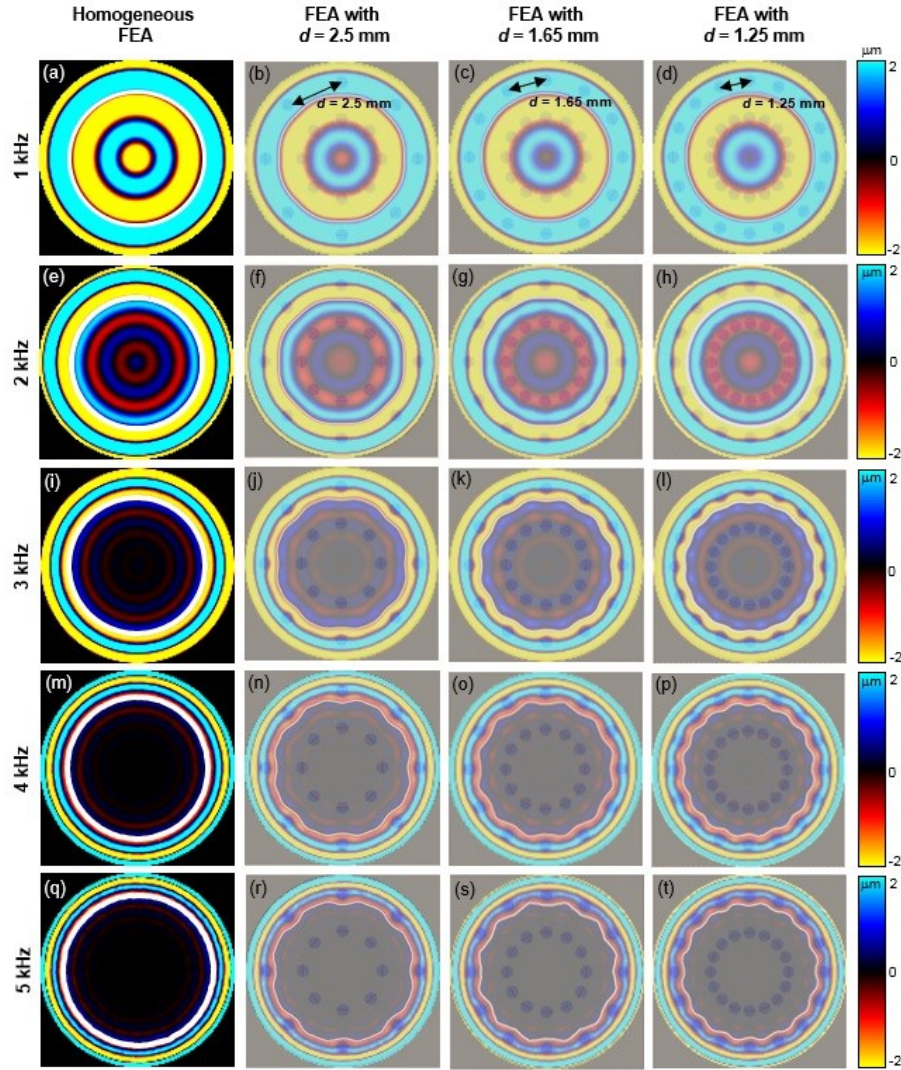


Figure 24. Contours of real part of shear wave displacement profiles for FE simulation. Snapshots of the shear wave at frequencies of 1 kHz (a-d), 2 kHz (e-h), 3 kHz (i-l), 4 kHz (m-p) and 5 kHz (q-t) for a homogeneous 5% w/v water based gelatin finite element phantom (first column) versus inhomogeneous finite element phantoms (columns 2 through 4) containing uniformly distributed spherical inclusions of spacing d (2nd column: $d=2.5$ mm; 3rd column: $d=1.65$ mm; 4th column: $d=1.25$ mm) that cause scattering of wave fronts.

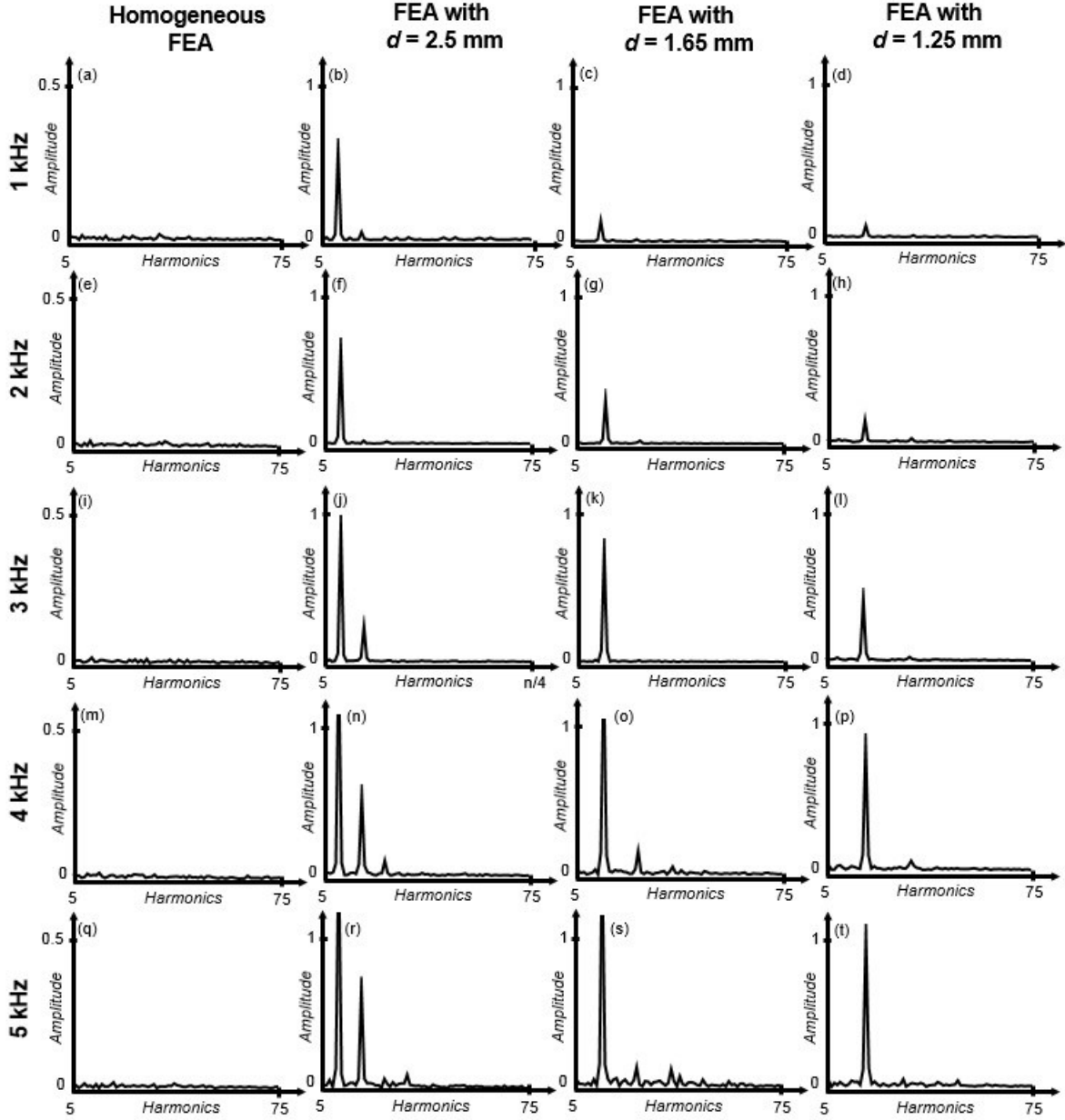


Figure 25. Frequency spectra for delineated contours of zero shear wave displacement in Finite Element Simulations: Frequency spectra obtained using spatial Fourier Transform of the delineated wave fronts at mechanical frequencies of 1 kHz (a-d), 2 kHz (e-h), 3 kHz (i-l), 4 kHz (m-p) and 5 kHz (q-t). From Left: Column 1: Wave spectra for a homogeneous 5% w/v water-based gelatin Finite Element phantom; Columns 2 through 4: Wave spectra for Finite Element phantoms containing spherical inclusions (of diameter 0.5 mm) with a spacing of $d = 2.5$ mm, $d = 1.65$ mm and $d = 1.25$ mm, respectively.

3.4.3 MRE experiments on excised porcine lumbus muscle

MRE experiments were performed on an ex-vivo sample of a porcine muscle as described in section 3.3. Figure 26 depicts the shear wave front of zero displacement along with frequency spectra at mechanical frequencies of 500 Hz, 600 Hz, 800 Hz and 1 kHz; table 5 C presents the values of 1-Norm computed at the aforementioned mechanical frequencies.

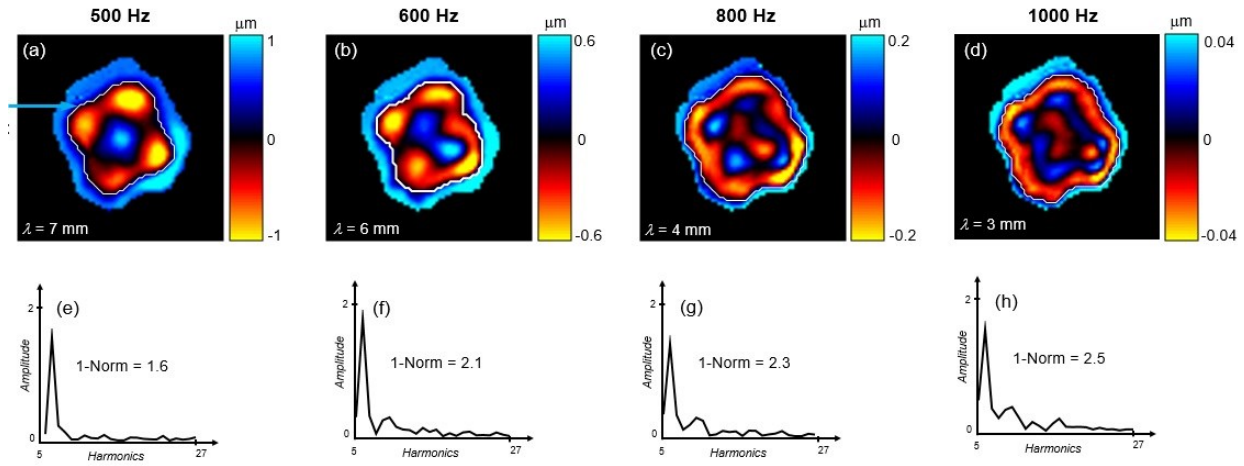


Figure 26. Results of MRE experimentation on excised porcine lumbus muscle sample. **(a-d)** Plots of real part of complex-valued shear wave displacement along with delineated profile of zero displacement (highlighted in white color) observed in the MRE experiments on ex-vivo porcine lumbus muscle at frequencies of a) 500 Hz, b) 600 Hz, c) 800 Hz and d) 1000 Hz. **(e-h)** The corresponding frequency spectra for the delineated profile of zero wave displacement at frequencies of e) 500 Hz, f) 600 Hz, g) 800 Hz and h) 1000 Hz, along with the 1-Norm values.

Note: The direction of muscle fibers is normal to the plane of the image.

3.4.4 MRE on excised bovine liver tissue

Figure 27 presents the results of MRE experimentation on ex vivo bovine liver sample, including the contours of shear wave displacement of the liver ROI and the gelatin ROI.

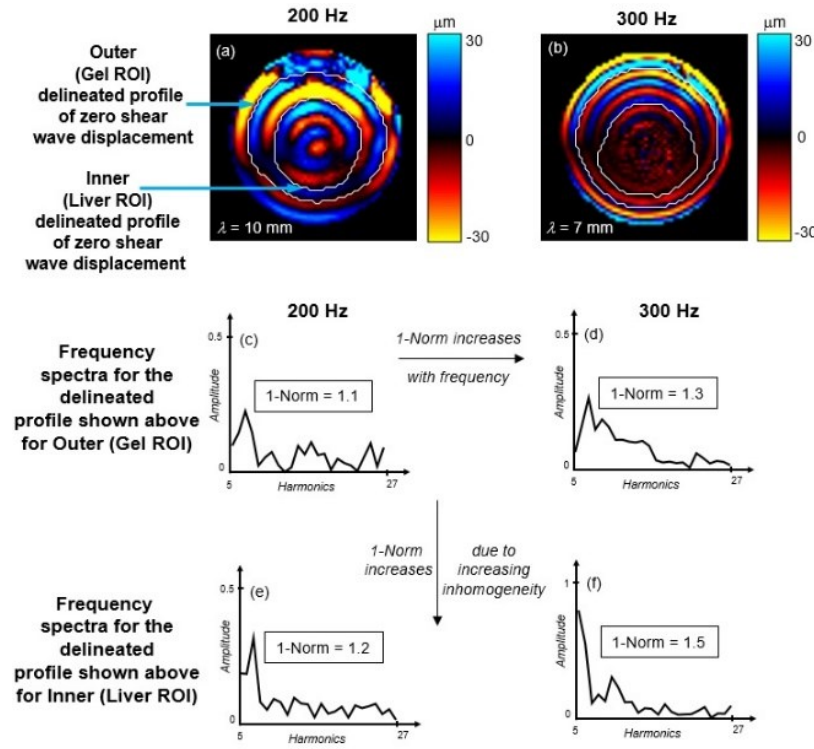


Figure 27. Results of MRE experimentation on excised bovine liver tissue. **(a-b)** Shear wave images and zero displacement contour lines (highlighted in white color) observed in the MRE experiments on ex-vivo porcine lumbus muscle at frequencies of a) 200 Hz and b) 300 Hz. **(c-d)** The corresponding frequency spectra for the surrounding medium (gel) at frequencies of c) 200Hz and d) 300 Hz. **(e-f)** Frequency spectra for the delineated contour of zero displacement for the liver at e) 200 Hz and f) 300 Hz.

3.5 Discussion

3.5.1 Coupled anisotropy and scattering effects

The investigation revealed that in the 3D printed inhomogeneous phantom there was an elongation of the wave front along the direction of fibers, in addition to a scattering effect at the locations of

intersection of fibers, and that the orientation of the wave front elongation varied with the mechanical phase (see fig. 28). This situation represented a coupled scenario, in which two separate phenomena, namely, scattering and anisotropy effects occurred simultaneously, thereby making the problem more complex. In the current study, therefore, FEA has been used as a tool to de-couple the effects of directional anisotropy caused due to fibers, from those of inhomogeneities, observed at the locations of fiber intersections. This has been achieved by Finite Element modeling of three-dimensional phantoms containing uniformly distributed and symmetrically spaced repeatable units of individual spheres (of diameter 0.5 mm) that act as inhomogeneities as described in section 3.3.2.

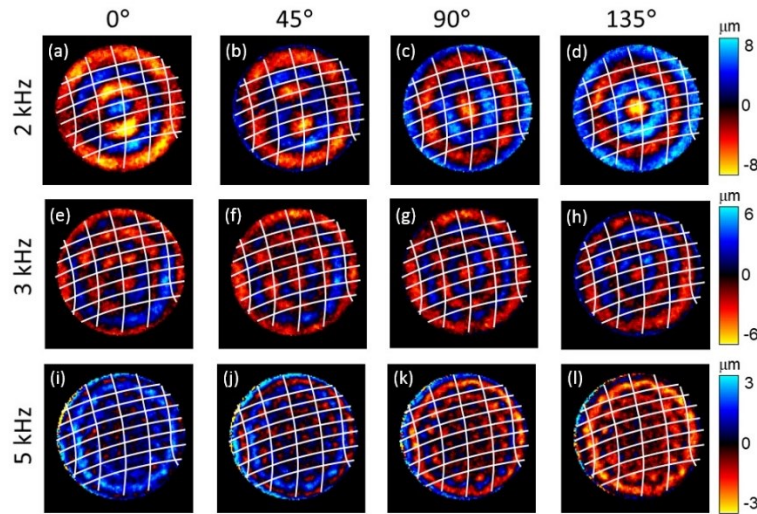


Figure 28. Snapshots of shear waves propagating in the 3D printed inhomogeneous fiber phantom for varying mechanical phases at frequencies of (a) through (d): 2000 Hz; (e) through (h): 3000 Hz and (i) through (l): 5000 Hz. The wave fronts exhibit both elongation (due to directional anisotropy) accompanied with scattering (at fiber intersections) due to inhomogeneities. Fibers are highlighted in white color.

3.5.2 Interpretation of 1-Norm Variations

It is observed in fig. 23 A that the delineated profile of zero shear wave displacement (highlighted in white) is distorted from that of a perfect circle due to the presence of fiber intersections. In addition, the effects of scattering become more pronounced with increasing mechanical frequency, which can also be observed as a shift of the wave spectrum towards higher harmonics as shown in fig. 23 B. This results in a higher value of 1-Norm at higher mechanical frequencies. For the homogeneous 10% w/v water-based gelatin phantom, the scattering effects are less prominent as compared to the inhomogeneous 3D printed fiber phantom, as expected, due to an absence of inhomogeneity and anisotropy.

Finite element simulations were performed in order to understand the effects of uniformly distributed and symmetrically spaced spherical inclusions inside a homogeneous matrix medium on the behavior of shear wave propagation. This scenario decouples inhomogeneity from anisotropy because of the absence of fibers. From the contour lines of zero displacement (drawn in white) in figure 24, it is observed that for a given distance (d) between neighboring spherical inclusions, the wave scattering becomes more pronounced with an increase in the mechanical frequency. This is due to the fact that as the mechanical frequency increases, the wavelength of the propagating shear waves approaches the value of the distance (d) between the neighboring spherical inclusions, thereby resulting in stronger scattering of the incident wave front, as shown in fig. 29.

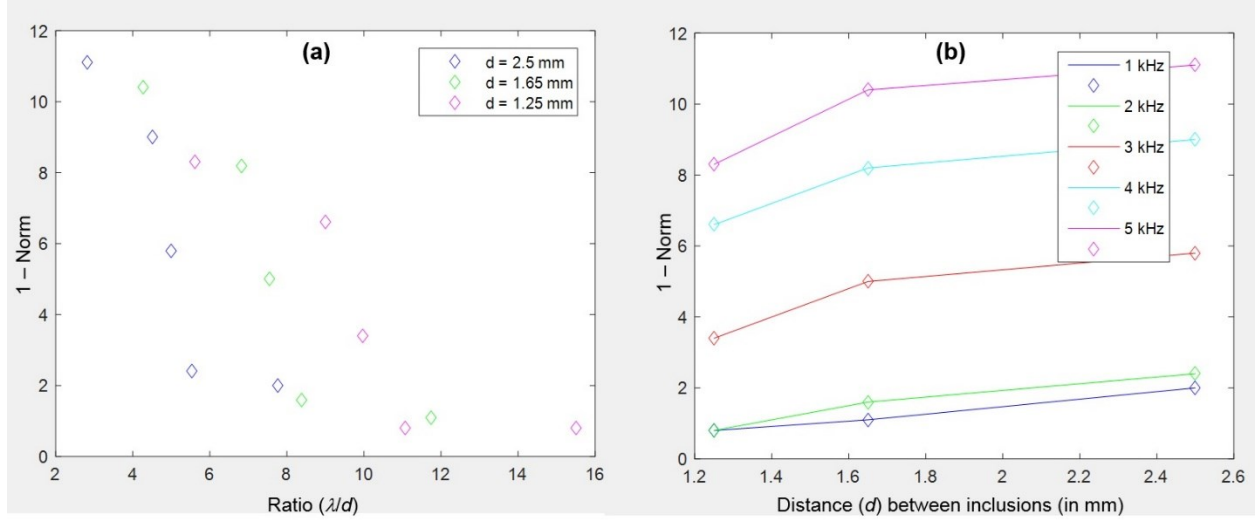


Figure 29. Plot of variation of 1-Norm with respect to the ratio (λ/d), where λ is the wavelength of propagating shear waves and d is the spacing between neighboring spherical inclusions. **(b)** Plot of variation of 1-Norm with respect to the spacing (d) between the neighboring spherical inclusions, at frequencies of 1 kHz, 2 kHz, 3 kHz, 4 kHz and 5 kHz.

While the variation of 1-Norm may depend on a variety of experimental conditions such as the mechanical parameters of the matrix and inclusion or fibers, distribution and shape of the inclusions, presence of noise and mechanical frequency, all observations in the simulation study imply that the 1-Norm is inversely correlated to the ratio of wavelength (λ) and distance (d) between inclusions.

We further note that our FE model represents both ends of the extremities with respect to the limits on the distance (d) between the neighboring inclusions. For instance, at the lower limit, as $d \rightarrow 0$, the inclusions form a ring. On the other extreme, we have the upper limit of $d \rightarrow \infty$, which means a homogeneous medium that has the mechanical properties of the matrix. Indeed, we observe at a given frequency, as the distance (d) between the neighboring spherical inclusions increases, thereby receding from the condition of homogeneity at the lower d -limit, the contour lines possess higher spectral values resulting in increased 1-Norm values. However, the increase rate (or slope) of the 1-Norm seems to get weaker at higher d -values. The investigator speculates

that the 1-Norm over d function will reach a maximum and eventually decline as it approaches the higher d -limit of homogeneity.

From fig. 26 it is observed that MRE experiments on the ex-vivo porcine lumbus muscle sample and the bovine liver tissue sample show the same trend as observed in the 3D printed inhomogeneous fiber phantom as well as Finite Element Analysis. Based on the 1-Norm value, shear wave scattering increases with the mechanical frequency. A higher value of 1-Norm was observed in the skeletal muscle as compared to the liver under experimental conditions with similar wave length. This observation makes sense, as the muscle tissue is more inhomogeneous (due to the fibers) in comparison to the liver tissue.

The investigator notes that the values of 1-Norm are considerably higher for the 3D printed anisotropic fiber phantom in comparison to the Finite element phantom containing spherical inclusions due to the coupling between directional anisotropy (due to fibers) and inhomogeneity (at the locations of fiber intersections), as well as due to the presence of noise in MRE experiments using the physical phantom. The presence of this noise can be seen on the frequency spectra shown in fig. 23 B (bottom row) versus fig. 25 (column 1 at 3 kHz): while the spectral values are smaller for finite element analysis compared to the ones obtained using MRE, they are also more uniform and sharper, which indicates smooth wave front variations that can also be observed in figure 24. Thus, FEA provides an almost noise free environment for the examination of scattering effects in comparison to a physical MRE experiment, besides being more flexible, faster and economical.

3.5.3 Limitations

The current FEA investigation of the 1-Norm has two limitations. Firstly, while the work emphasizes the effect of distance between spherical inclusions on the scattering of shear waves, the size (diameter) of the spherical inclusions can also influence the pattern of wave scattering.

The current work has not explored the influence of varying the diameter of the spherical inclusions on the nature of propagation of shear waves. Secondly, the current study has limited itself to uniformly distributed spherical inclusions and thus, a future extension of this work will include randomly distributed spherical inclusions of various diameters and their effect on the shear wave propagation. Thirdly, the current capabilities of 3D printing bio-phantoms do not permit the investigator to achieve alignment of fibers in a direction perpendicular to the plane of the image. The 3D bioplotter (EnvisionTEC GMBH 3D Bioplotter) can overlay one layer of fibers over another in the same plane as that of the image. This explains why the direction of anisotropy is different in the 3D printed fiber phantom in comparison to the actual ex vivo muscle tissue.

3.5.4 Outlook

The current investigation has established the 1-Norm as a tool for quantification of scattering of wave fronts due to the presence of inhomogeneities. It is noted that the investigator attempted to fit power functions of the form $y = a(x^b)$, where y represents the measured values of 1-Norm (from FEA) and x represents the distance between the two neighboring spherical inclusions; a and b are variables. The investigator tried to fit power functions using $a = 1$ and $b = \frac{1}{2}$ as well as with $b = \frac{1}{3}$. Optimization of parameters a , b (and inclusion of an additional parameter c) using a power function of the form $y = a(x^b) + c$ using the *cftool* command in Matlab was also performed. It was observed that none of these power functions gave a perfect fit at each frequency of interest. While the investigator was able to explain the 1-Norm variations for different experimental FEA scenarios, it was not feasible to find an equation that could directly relate the values of 1-Norm to the experimental parameters. This endeavor requires the consideration of other experimental scenarios such as inhomogeneous phantoms with varying inclusion sizes, with different stiffness ratios of matrix and inclusions, as well as with randomly distributed inclusions.

The current definition of 1-Norm is optimized to circular wave fronts: these can be introduced either from the exterior of the circular medium (using geometric focusing technique), or these waves can be introduced using a point-source excitation at the center of the specimen. The application of the technique of 1-Norm to other experimental conditions may require optimization to the geometry of contact area between actuator and tissue. The investigator speculates that the current definition of 1-Norm already yields valuable results when, for example, using an (approximately) plane source. In this situation simply the first processing step of coordinate transformation can be omitted but the subsequent steps should be the same.

In a real-world scenario, the inclusions could represent neighboring filaments of the skeletal muscle. Therefore, in a long-term perspective, future studies may evaluate the 1-Norm for healthy human skeletal muscles and compare the values to those of injured/ traumatized skeletal muscle in order to be able to develop a non-invasive quantitative diagnostic technique capable of identifying the location and extent of damage and injury to a skeletal muscle.

There has been a previous work that investigated the influence of inhomogeneities on shear wave propagation [76]. In Papazoglou et al. the scatters were randomly distributed and different regimes of shear wave diffusion were found depending on experimental parameters, such as shear wave length, mean scatterer (inclusion) spacing and stiffness of the scatterers (inclusions). However, in the current study, a different approach was used which involved analyzing wave front distortion quantified in the form of 1-Norm and to study the dependence of the 1-Norm values on experimental parameters in phantoms with uniformly distributed scatterers. This pilot study may open the path to use the 1-Norm as biomarker for diseases that result in heterogeneous stiffness distribution, such as primary sclerosing cholangitis [77]. It is noted that the usefulness of the 1-

Norm under in vivo conditions with randomly distributed inclusions needs to be investigated in future studies. It remains to be shown if any of the scatterer approaches, namely, the 1-Norm technique or the shear wave diffusion technique [30], alone or in combination are sensitive biomarkers for diseases with a high degree of inhomogeneity.

4. 1-NORM TO CHARACTERIZE CHANGES IN MECHANICAL INHOMOGENEITY IN FREEZE-THAWED TISSUES AND IN MOUSE BRAIN DUE TO NEURODEGENERATIVE DISEASE

4.1 Introduction

The objective of this chapter is to demonstrate the validity and relevance of the 1-Norm waveform analysis technique in being able to detect inhomogeneities and quantify the degree of mechanical property inhomogeneity of a biological tissues due to freezing and thawing, and due to neurodegenerative disorder (Alzheimer's disease). Using the current work the investigator hopes to be able to prove the reliability of 1-Norm as a quantitative 'marker' of the degree of inhomogeneity of a tissue, and as an alternative MRE-based biomarker to stiffness, which relies on ill-posed wave inversion.

4.1.1 Hypotheses

It is hypothesized that a freeze/thaw cycle leads to a measurable change in the mechanical inhomogeneity of biological tissues due to the destruction of the cell wall during freezing and thawing. Likewise, it is hypothesized that neurodegenerative diseases such as Alzheimer's disease (AD) lead to a change in the mechanical property inhomogeneity of the brain due to deposition of amyloid plaque [78] and a loss of neurons [79]. The dissertation aims to test these two hypothesis by performing MRE experiments on a range of excised biological tissues, namely: excised porcine kidneys (3 samples), excised porcine liver (3 samples), excised porcine lumbar muscle (3 samples) and, separately on 3 control (healthy) female mice brains and 3 5xFAD species female mice brains with AD. It is proposed to apply the 1-Norm waveform analysis technique to analyze the propagation of shear waves in these excised biological tissues in order to characterize their degree of inhomogeneity, due to freezing and thawing and due to neurodegenerative disease.

4.1.2 Approach

In a prior work [2], the investigator has established the 1-Norm as a mathematical tool to quantify the degree of mechanical inhomogeneity of an excised porcine lumbus muscle and excised bovine liver tissue. The prior investigation [2] had noted that the scattering effects of inhomogeneities became more pronounced at higher mechanical frequencies of excitation which was reflected through higher values of 1-Norm. The aim of the current work is to demonstrate the validity and relevance of 1-Norm on four different excised biological tissues, namely, porcine kidneys, porcine liver, porcine lumbus muscle and female mouse brain (control and 5xFAD species with Alzheimer's disease). Through the use of these four different types of excised tissues, this investigation aims to: firstly, to demonstrate that 1-Norm is capable of quantifying the magnitude of scattering of mechanical wavefronts, thereby, serving as a "marker" for identifying the degree of mechanical inhomogeneity of biological tissues. Secondly, the investigation aims to demonstrate the capability of the 1-Norm as an alternate tool to wave inversion, which is currently the standard technique used to estimate the stiffness of biological tissues. By computing 1-Norm, one would not have to perform a wave field inversion (which is an ill-posed technique) to estimate the stiffness of biological tissues.

4.1.3 Frozen Tissue Samples

Bio-specimens (blood, tissues and other fluids) are harvested from both patients and healthy individuals for research as well as for the treatment of diseases through the development of personalized medicine [80]. This involves tailoring therapies for individual patients by evaluation of their genome. For these purposes, it is necessary to ensure that after extraction, these bio-specimens are preserved in such a way so as to ensure the genetic material (RNA and DNA) and the extra-cellular matrix which contains proteins and enzymes remain intact until their required

purpose is fulfilled. Freezing is the preferable technique used in preserving bio-specimens [80]. An advantage of using freezing is that in a frozen tissue, proteins are uniquely well preserved along with intactness of all the enzymatic activity [80]. Pathology departments and biobanks will likely have to store and disseminate increasing numbers of frozen bio-specimens to meet an increasing demand from the healthcare industry. In a first application of the 1-Norm technique to a real-life healthcare scenario, the investigator aims to investigate the influence of freezing and thawing of biological tissues on the mechanical inhomogeneity using 1-Norm. Here, it is demonstrated that 1-Norm is capable of identifying a change in the stiffness of frozen tissue, which is reflected through an increase in the magnitude of scattering of mechanical wavefronts. Results are validated against an earlier work [59] by estimating tissue stiffness before and after freezing and thawing. Based on the findings of this investigation, it is concluded that 1-Norm can potentially serve as an alternative MRE-based biomarker to stiffness, which relies on ill-posed wave inversion.

4.1.4 Alzheimer's Disease

Alzheimer's disease (AD) is a progressive neurodegenerative disease that causes the brain to shrink (atrophy) and the brain cells to die [81]. Alzheimer's disease is the most common cause of dementia — a continuous decline in thinking, behavioral and social skills that affects a person's ability to function independently. Approximately 5.8 million people in the United States age 65 and older live with Alzheimer's disease [81]. Of those, 80% are 75 years old and older. Out of the approximately 50 million people worldwide with dementia, between 60% and 70% are estimated to have Alzheimer's disease [81]. The early signs of the disease include forgetting recent events or conversations. As the disease progresses, a person with Alzheimer's disease develops severe memory impairment and loses the ability to carry out everyday tasks. At a microscopic level, AD is associated with a loss of neurons [79], synaptic degeneration, a loss of white matter tracts due

to axonal damage and amyloid plaque deposition [78]. In a prior work [82], researchers have used MRE to assess mechanical wave propagation in healthy and in Alzheimer's brain, and have shown that AD leads to a reduction in the stiffness of the brain. In the current investigation, the investigator has used excised brains from 3 control female mice and 3 5xFAD species female mice with AD, at 10 months of age at the time of experimentation. The 5xFAD species female mice had AD that had already progressed into an advanced stage and the mice were displaying a range of cognitive and motor deficits [79].

4.1.5 Significance of the current investigation

MRE is a clinically proven and well-established non-invasive method that involves estimating the stiffness of biological tissues in-vivo to assess the influence of disease on the tissue mechanical properties [65]. However, current methods involve use of wave inversion to estimate the tissue stiffness, and wave inversion techniques are ill-posed. Therefore, 1-Norm is proposed as a novel alternative MRE-based biomarker to stiffness, which relies on ill-posed wave inversion and this is achieved by demonstrating a correlation between the values of 1-Norm (signifying wave scattering due to the presence of inhomogeneity) and tissue stiffness during neurodegenerative disorder and due to freezing and thawing. While still at a nascent pre-clinical stage, the investigator believes that the 1-Norm wave-scattering technique has the potential to serve as a biomarker in detecting the presence and in staging the severity of diseases that involve a change in the heterogeneity of biological tissues such as neurodegenerative diseases (AD), primary sclerosing cholangitis (PSC) of the liver and musculoskeletal disorders.

4.2 Method

MRE experiments were performed on excised porcine kidney specimens (3 samples), porcine liver specimens (3 samples), porcine lumbus muscle specimens (3 samples), and excised mouse brains (3 female control mice and 3 5xFAD female mice model of AD, both at 10 months of age). MRE experiments were performed using a novel 0.5 T Tabletop MRI system (Pure Devices, Würzburg-Rimpar, Germany). The following sections describe the sample preparation steps, the apparatus used and the MRE experimental parameters in detail.

4.2.1 Experimentation set-up

As MRE involves application of harmonic vibration to the sample in conjunction with MRI, a custom-built experimental set up was used [73] in order to simultaneously grip the sample in a vertical position and apply a harmonic excitation as shown schematically in fig. 17. Experiments were performed on a 0.5 T Tabletop MRI system (Pure Devices, Würzburg-Rimpar, Germany). A “trigger signal” from the MRI pulse sequence prompted the wave form generator (33220A Function/Arbitrary Waveform Generator, 20 MHz, Agilent Technologies Test and Measurement, Englewood, CO) to produce an electrical signal that was then amplified by a power amplifier (P3500S Power Amplifier, Yamaha Corporation of America, Buena Park, CA). A Direct Current bias was added to the output of the power amplifier through a series connection of a constant DC power supply unit (E3634A 200W Power Supply, Agilent Technologies Test and Measurement, Englewood, CO). The usage of this DC voltage bias ensured positive-valued voltage oscillations across the terminals of the piezoelectric device, so as to preserve its mechanical integrity.

4.2.2 MRE experimentation on excised porcine kidneys, liver and lumbus muscle tissues

Fresh kidneys, livers and lumbus muscle samples were obtained from 3 individual porcine subjects from a local slaughterhouse. Circular samples with a diameter of 1 cm and a thickness of

5 mm were carefully extracted from each of these tissues. These circular samples were then carefully placed inside a borosilicate glass tube with an outer diameter of 10 mm. MRE experiments were then performed on these fresh samples, using a spin echo pulse sequence, and using a Geometrically-focused harmonic excitation. Table 6 enlists the relevant MRE experimentation parameters.

Table 6. MRE Experimentation Parameters for fresh and frozen kidney, liver and muscle samples.

MRE Pulse Sequence Parameters	Parameter Value
Field of view	9.6 mm x 9.6 mm
Acquisition matrix size	128 x 128
Number of slices	1
Slice thickness	5 mm
Echo time (TE)	35.8 ms
Repetition time (TR)	500 ms
Number of averages	1
Number of time steps	4 (2 acquisitions at each time step with an inverted polarity)
Mechanical frequencies analyzed	500 Hz, 1000 Hz, 1500 Hz, 2000 Hz
Pulse sequence	Spin Echo

In the next step, after completion of the aforementioned MRE experiments, each of the fresh tissue samples (kidney, liver and lumbus muscle) was frozen by placing the glass tube containing the sample inside a refrigerator at -20°C for 24 hours. These samples were then thawed to room temperature (25°C), and the same set of MRE experiments (Table 6) were repeated on these thawed samples.

4.2.3 MRE experimentation on Control and Alzheimer’s Mouse Brain Samples

6 Murine brain samples were harvested from 3 female control mice and 3 5xFAD female mice with AD. Each mouse was of 10 months of age at the time of experimentation. Each brain sample

was carefully placed in a separate 10 mm diameter borosilicate glass tube, whose one end was connected to a piezoelectric actuator. MRE experimentation was performed using the same vibration set-up and the same 0.5 T Table-top MRI system. A spin-echo pulse sequence was used, with the other relevant experimental parameters as enlisted in table 7.

Table 7. MRE Experimentation Parameters for investigating 3 ex vivo control brains and 3 ex vivo 5xFAD Mouse Brains of AD model

MRE Pulse Sequence Parameters	Parameter Value
Field of view	10 mm x 10 mm
Acquisition matrix size	64 x 64
Number of slices	1
Slice thickness	5 mm
Echo time (TE)	13.1 ms
Repetition time (TR)	226.3 ms
Number of averages	1
Number of time steps	8
Mechanical frequencies analyzed	1200 Hz, 1500 Hz, 1800 Hz
Pulse sequence	Spin Echo

4.2.4 Data processing

The data obtained from MRE experiments was analyzed using Matlab (Mathworks Inc., Natick, MA). Image reconstruction was performed on the phase images at each mechanical frequency, by first applying Flynn Phase-unwrapping algorithm followed by a 2π trend correction to minimize phase wraps. Subsequently, a band-pass filter was used to eliminate the compression wave component and noise in each of the phase images. Complex displacement wave images were obtained by choosing the second frequency bin after Fourier transformation along the time-resolved and filtered phase images. At each of the frequencies, the real part of the complex shear wave displacement image was visualized and the ‘*contour*’ command in Matlab was used to identify and delineate the wave profiles having equal displacement (for example, zero displacement). The delineated contour profiles at each of the frequencies were selected so as to be at the same distance from the outer edge of the bin. The coordinate positions (in Cartesian

coordinate system) of each of the points located on the delineated contours were transformed into polar coordinates. The polar coordinates of each of the points were used to compute the distance from the geometric center of the wave image and these were then sorted in to a dataset. This data set was used to generate a frequency spectrum using a discrete spatial Fourier transform in Matlab. A numerical value for 1-Norm was obtained using a summation of absolute values of Fourier transform of these harmonics from 7 to 27.

Of special attention is the fact that the static component and the first six harmonics that show contributions due to center mismatch, the circle or the ellipse, or the shape of the biological specimen were discarded in the calculation of the 1-Norm. Therefore, by definition, the values of 1-Norm quantify the degree of inhomogeneity of the biological sample under investigation. The reader is referred to section 3.3.5 of our prior work [2] to better understand how we eliminated the contributions of the geometry and the shape of biological specimen from the final value of 1-Norm.

The stiffness (real part of shear modulus) was also computed for each of the fresh and freeze-thawed biological samples as well as the mouse brain samples, using the technique described in Chapter 3. These were used to understand the relationship between tissue mechanical inhomogeneity and tissue stiffness for various biological samples, as discussed in detail in section .

4.3 Results

4.3.1 MRE experimentation on fresh and freeze-thawed excised porcine kidneys

Figure 30 presents the wave images of the real part of complex displacement for fresh and freeze-thawed ex vivo porcine kidney sample no. 1. Three such samples were analyzed. Delineated contours of zero wave displacement are highlighted in white color. Tables 8 and 9 present the variation of group averaged values

of 1-Norm and stiffness of the 3 kidney samples in fresh condition and after freezing and thawing respectively.

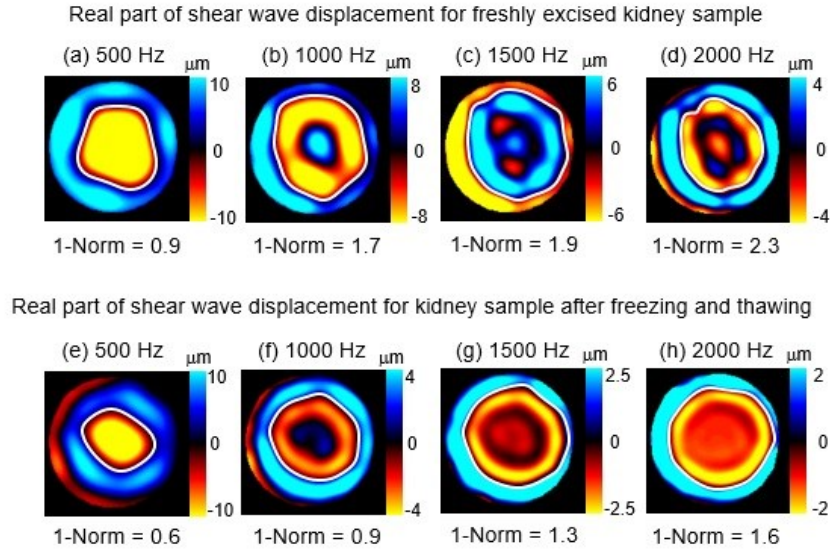


Figure 30. Contours of shear wave displacement, along with delineated profile of equal (zero) displacement (white color), for freshly excised kidney sample no. 1 (a-d) and for the same kidney sample after freezing and thawing (e-h).

Table 8. Variation of group-averaged values of 1-Norm as a function of mechanical frequency of excitation for excised porcine kidneys before and after freeze-thawing, with standard deviation (for $n = 3$ kidney samples) presented in parenthesis

Mechanical Frequency	Group-averaged 1-Norm of fresh kidney sample	Group-averaged 1-Norm of kidney sample after freezing and thawing
500 Hz	0.8 ($\sigma = 0.1$)	0.4 ($\sigma = 0.1$)
1000 Hz	1.4 ($\sigma = 0.2$)	0.9 ($\sigma = 0.2$)
1500 Hz	1.7 ($\sigma = 0.1$)	1.2 ($\sigma = 0.2$)
2000 Hz	2.1 ($\sigma = 0.2$)	1.5 ($\sigma = 0.1$)

Table 9. Variation of group-averaged values of stiffness of excised porcine kidneys as a function of mechanical frequency of excitation, before and after freeze-thawing, with standard deviation (for $n = 3$ kidney samples) presented in parenthesis

Mechanical Frequency	Group-averaged stiffness of fresh kidney sample (kPa)	Group-averaged stiffness of kidney sample after freezing and thawing (kPa)
500 Hz	3.6 ($\sigma=0.3$)	1.7 ($\sigma=0.1$)
1000 Hz	5.2 ($\sigma=0.7$)	3.4 ($\sigma=0.4$)
1500 Hz	7.0 ($\sigma=0.6$)	5.3 ($\sigma=0.2$)
2000 Hz	8.5 ($\sigma=1.7$)	6.0 ($\sigma=1.8$)

4.3.2 MRE experimentation on fresh and freeze-thawed excised porcine liver

Figure 31 presents the wave images of the real part of complex displacement for fresh and freeze-thawed ex vivo porcine liver sample no 1. Three such samples were individually analyzed. Delineated contours of zero wave displacement are highlighted in white color. Tables 10 and 11 present the variation of group averaged values of 1-Norm and stiffness of the 3 liver samples in fresh condition and after freezing and thawing respectively.

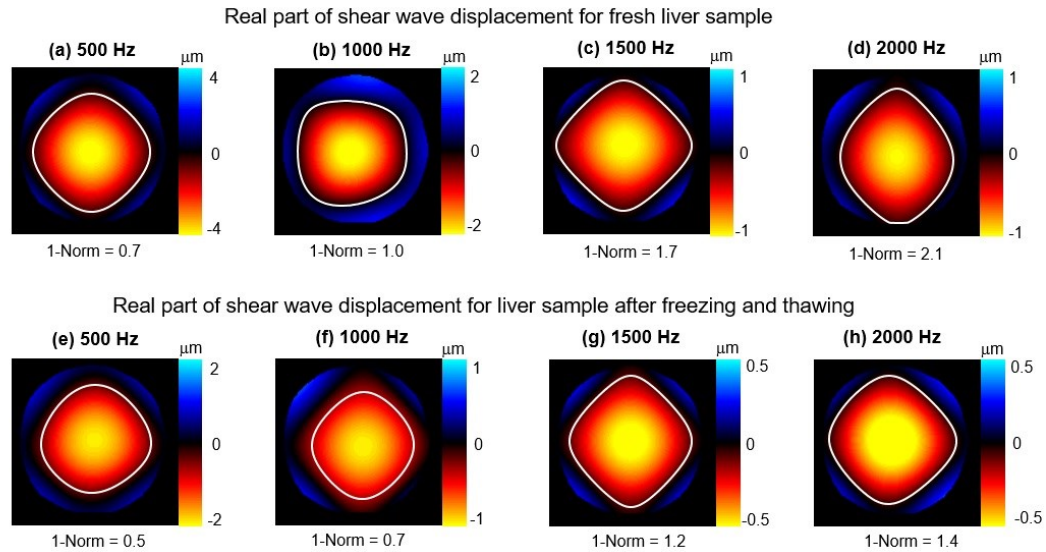


Figure 31. Contours of shear wave displacement, along with delineated profile of equal (zero) displacement (white color), for freshly excised porcine liver sample (a-d) and for the same sample after freezing and thawing (e-h).

Table 10. Variation of group-averaged values of 1-Norm as a function of mechanical frequency of excitation for excised porcine liver tissue before and after freeze-thawing, with standard deviation (for $n = 3$ liver samples) presented in parenthesis.

Mechanical Frequency	Group-averaged 1-Norm of fresh liver sample	Group-averaged 1-Norm of liver sample after freezing and thawing
500 Hz	0.8 ($\sigma=0.08$)	0.6 ($\sigma=0.05$)
1000 Hz	1.1 ($\sigma=0.08$)	0.8 ($\sigma=0.05$)
1500 Hz	1.7 ($\sigma=0.05$)	1.2 ($\sigma=0$)
2000 Hz	2.1 ($\sigma=0.05$)	1.5 ($\sigma=0.09$)

Table 11. Variation of group-averaged values of stiffness of excised porcine liver tissue as a function of mechanical frequency of excitation, before and after freeze-thawing, with standard deviation (for $n = 3$ liver samples) presented in parenthesis.

Mechanical Frequency	Group-averaged stiffness of fresh liver sample (kPa)	Group-averaged stiffness of liver sample after freezing and thawing (kPa)
500 Hz	3.8 ($\sigma=0.1$)	1.9 ($\sigma=0.1$)
1000 Hz	5.5 ($\sigma=0.7$)	3.7 ($\sigma=0.2$)
1500 Hz	6.4 ($\sigma=0.8$)	4.3 ($\sigma=0.1$)
2000 Hz	9.2 ($\sigma=0.8$)	6.7 ($\sigma=0.3$)

4.3.3 MRE experimentation on fresh and freeze-thawed excised porcine lumbus muscle

Figure 32 presents the wave images of the real part of complex displacement for fresh and freeze-thawed ex vivo porcine lumbus muscle sample no 1. Three such samples were individually analyzed. Delineated contours of zero wave displacement are highlighted in white color. Tables 12 and 13 present the variation of group averaged values of 1-Norm and stiffness of the 3 muscle samples in fresh condition and after freezing and thawing, respectively.

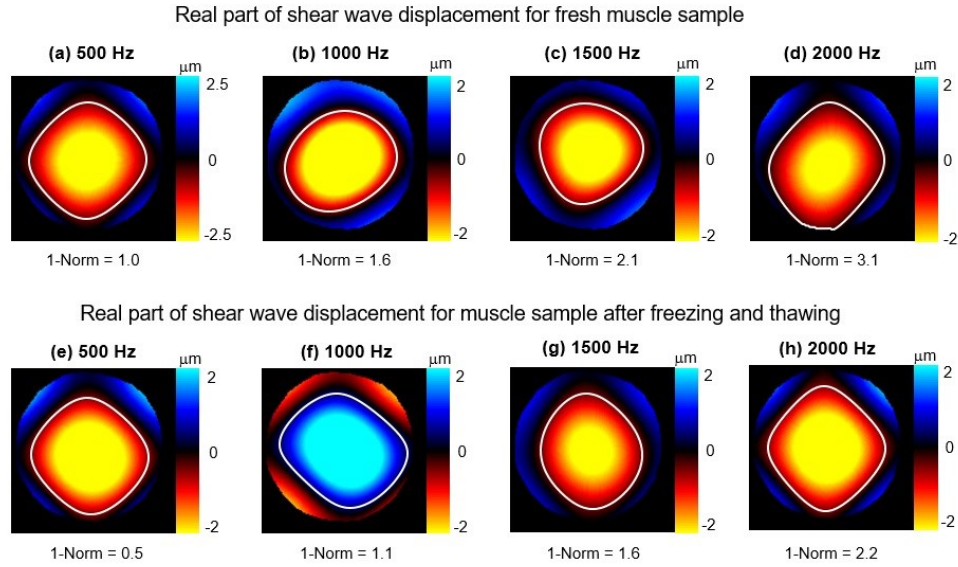


Figure 32. Contours of shear wave displacement, along with delineated profile of equal (zero) displacement (white color), for freshly excised (a-d) porcine lumbus muscle sample and for the same sample after freezing and thawing (e-h).

Table 12. Variation of group-averaged values of 1-Norm as a function of mechanical frequency of excitation for excised porcine lumbus muscle sample before and after freeze-thawing, with standard deviation (for $n = 3$ muscle samples) presented in parenthesis.

Mechanical Frequency	Group-averaged 1-Norm for fresh muscle sample	Group-averaged 1-Norm for muscle sample after freezing and thawing
500 Hz	1.1 ($\sigma = 0.08$)	0.6 ($\sigma = 0.17$)
1000 Hz	1.6 ($\sigma = 0.10$)	1.0 ($\sigma = 0.04$)
1500 Hz	2.0 ($\sigma = 0.05$)	1.5 ($\sigma = 0.04$)
2000 Hz	2.9 ($\sigma = 0.17$)	2.1 ($\sigma = 0.07$)

Table 13. Variation of group-averaged values of stiffness of excised porcine lumbus muscle sample as a function of mechanical frequency of excitation, before and after freeze-thawing, with standard deviation (for $n = 3$ muscle samples) presented in parenthesis.

Mechanical Frequency	Group-averaged stiffness of fresh muscle sample (kPa)	Group-averaged stiffness of muscle sample after freezing and thawing (kPa)
500 Hz	4.1 ($\sigma=0.1$)	1.1 ($\sigma=0.03$)
1000 Hz	5.5 ($\sigma=0.6$)	2.9 ($\sigma=0.07$)
1500 Hz	8.1 ($\sigma=0.7$)	4.4 ($\sigma=0.10$)
2000 Hz	10.0 ($\sigma=0.8$)	5.1 ($\sigma=0.40$)

4.3.4 MRE experimentation on excised control and Alzheimer's disease mouse model brain

Figure 33 presents the wave images of the real part of complex displacement for the control brain of a female mouse (sample no. 2) and a 5xFAD species female mouse model of AD (sample no. 2). Three such samples were individually analyzed. Delineated contours of zero wave displacement are highlighted in white color. Tables 14 and 15 present the variation of group averaged values of 1-Norm (table 14) and stiffness (table 15) of the 3 control and 3 5xFAD mice brains.

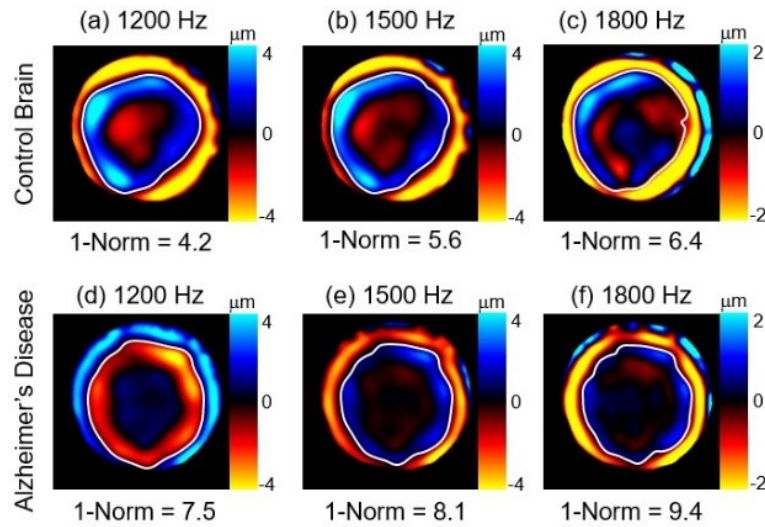


Figure 33. Contours of real part of complex displacement (sample no. 2) obtained after MRE experimentation on excised control (a-c) and Alzheimer's disease (d-f) mouse brains. A total of 3 samples were analyzed.

Table 14. Variation of group-averaged values of 1-Norm as a function of mechanical frequency of excitation for excised mouse brain (control) and 5xFAD mouse model of AD, with standard deviation (for $n = 3$ control and AD brain samples) presented in parenthesis.

Mechanical Frequency	Group-averaged 1-Norm for control mouse brain	Group-averaged 1-Norm for 5xFAD mouse model of AD
1200 Hz	3.4 ($\sigma=0.9$)	5.1 ($\sigma=0.9$)
1500 Hz	4.9 ($\sigma=2.0$)	6.6 ($\sigma=2.0$)
1800 Hz	5.5 ($\sigma=1.6$)	8.1 ($\sigma=3.0$)

Table 15. Group-averaged values of stiffness (real part of complex modulus) for 3 Control Mouse Brains and 3 Mouse models of AD (5xFAD). Standard deviation values are given inside the brackets.

Mechanical Frequency	Mean Stiffness	
	Control mouse brain	5xFAD mouse brain with AD
1200 Hz	9.4 ($\sigma = 0.6$) kPa	7.9 ($\sigma = 0.2$) kPa
1500 Hz	11.3 ($\sigma = 0.2$) kPa	9.5 ($\sigma = 0.6$) kPa
1800 Hz	14.9 ($\sigma = 1.0$) kPa	12.6 ($\sigma = 1.0$) kPa

4.4 Discussion

4.4.1 Influence of Freezing and Thawing on the bulk material inhomogeneity of excised tissues

Figure 34 presents a comparison of the group averaged values of 1-Norm for freshly excised (green) and freeze-thawed biological samples (red). The error bars indicate a limit of 1 standard deviation (above and below the average values). An Analysis of Variance between the 1-Norm values of the fresh and freeze-thawed muscle sample in each group showed a statistical difference with $p < 0.0001$.

It is observed that freezing and thawing leads to a reduction in the values of 1-Norm which in turn indicates a reduction in the degree of inhomogeneity of the biological tissues. In addition, for each sample, at higher mechanical frequencies (1500 Hz – 2000 Hz), the values of 1-Norm are high, which implies that the contributions of inhomogeneities become more prominent at higher mechanical frequencies of excitation. Stiffness of both fresh and freeze-thawed tissue samples was computed and it was observed that freezing and thawing led to a reduction in the overall stiffness of each tissue sample. An Analysis of Variance between the stiffness of the 3 fresh and freeze-thawed biological samples in each group showed a statistical difference with $p < 0.0001$.

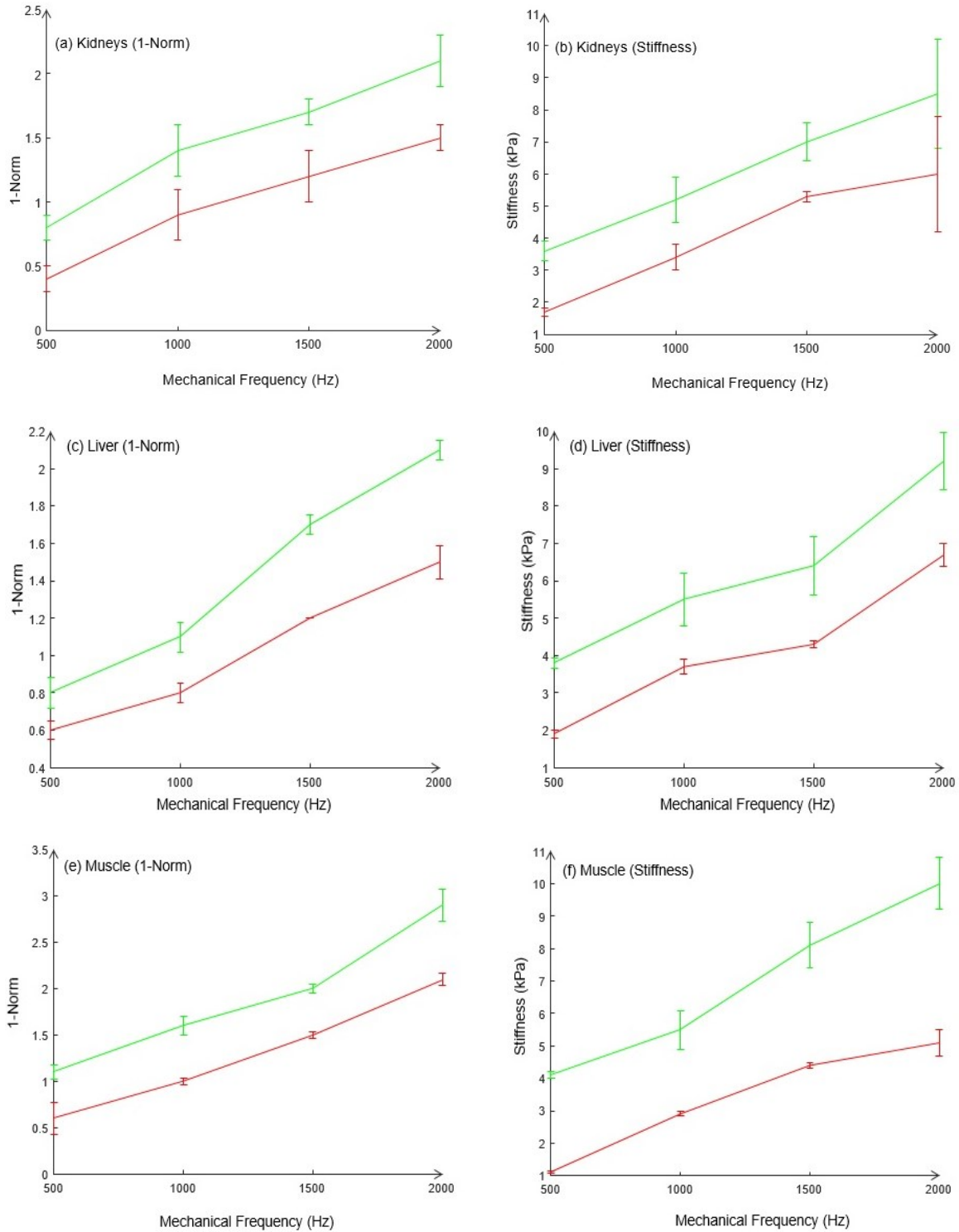


Figure 34. Group-averaged values of 1-Norm and stiffness as a function of mechanical frequency for porcine kidneys (a, b), porcine liver (c, d) and porcine lumbus muscle (e, f) under fresh condition (green) versus after freezing and thawing (red). The error bars indicate the standard deviation over the 3 samples in each group.

A correlation was observed between the variation of 1-Norm and the variation of stiffness due to freezing and thawing. Both 1-Norm and the stiffness reduced as a result of freezing and thawing. It is our speculation that freezing and thawing leads to a damage to the cellular structure of the biological tissues [80], leading to an overall reduction in the stiffness, accompanied by a reduction in the overall mechanical inhomogeneity of the tissue.

4.4.2 Alzheimer's disease and brain tissue inhomogeneity

Figure 35 (a) presents a comparison of the variation of group averaged values of 1-Norm for female control brain samples (green line) and the 5xFAD female mouse brains with AD (red line). As is evident from this plot, the value of 1-Norm for 5xFAD mouse brains with Alzheimer's disease (red) is higher than the 1-Norm value for control mouse brain (green) at each mechanical frequency. This implies that the Alzheimer's brain possesses a higher degree of mechanical inhomogeneity.

As a way of comparing and validating the results with an earlier published work [82], the investigator also computed the stiffness (real part of complex modulus) for each of the 3 control and 3 5xFAD model Alzheimer's mouse brain samples. A reduction in the overall stiffness (fig. 35 (b)) of the brains having Alzheimer's disease was observed, which is in line with the findings of the aforementioned prior study [82].

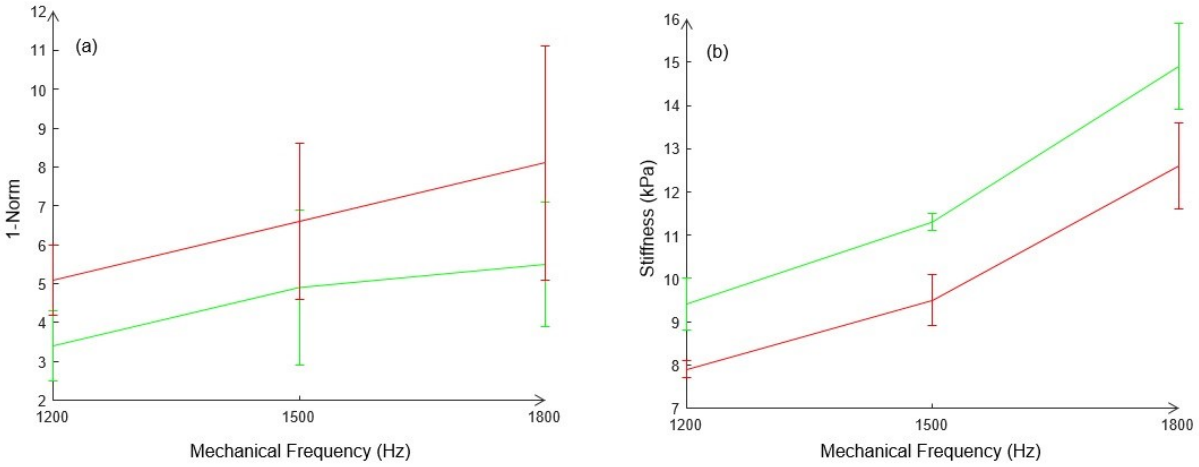


Figure 35. Group-averaged values of (a) 1-Norm and (b) stiffness as a function of mechanical frequency of excitation for 3 Control brains (green) and 3 5xFAD mouse brains with Alzheimer's disease (red). The error bars indicate the standard deviation over the 3 samples in each group.

The results of this investigation (fig. 35) indicate that neurodegenerative disease leads to an increase in mechanical property inhomogeneity of the brain tissue. This could be due to the following reasons: The 3 AD 5xFAD species female mice were 10 months old at the time of MRE experimentation and had developed severe amyloid plaque deposition [78] throughout the hippocampus and cortex region. Synaptic degeneration [79] and neuron loss [79] have also been observed in mice belonging to this model starting from 6 months of age. Additionally, a prior DTI-MRI [83] based clinical investigation on human subjects revealed an increased axial diffusivity in the brains with AD, which the researchers had attributed to axonal damage (which led to an increase in extra axonal space). The investigator therefore speculates that these 4 neurological conditions, that is, amyloid plaque deposition, synaptic degeneration, loss of neurons and axonal damage (leading to an increased axonal space), led to an observable increase in the degree of inhomogeneity of the brain tissue for the three samples of 10-month old female AD mice (5xFAD)

used in our study. Further studies are needed to understand the microstructural changes that lead to an increase in the degree of inhomogeneity of the brain tissue due to AD.

The investigator then compared the research findings of current study to a prior work by Majumdar et al [58] and it was noted that our results were in agreement with this prior study, which reported a reduction in the overall stiffness of the brain due to Alzheimer's disease.

4.4.3 1-Norm as a quantifier of tissue inhomogeneity

The current investigation used three types of ex vivo biological tissues, and investigated the influence of freezing and thawing on the degree of inhomogeneity of these tissues by analyzing the scattering of shear waves (1-Norm). It was observed that the values of 1-Norm were the highest for the porcine lumbar muscle (both in fresh condition and after freezing and thawing) in comparison to porcine kidneys and porcine liver tissue. This observation establishes the fact that the 1-Norm is indeed a relevant quantifier of the degree of inhomogeneity of a biological tissue. It is further noted that, as the mechanical frequency of excitation is increased, the degree of shear wave scattering also increases (both in fresh and in freeze-thawed tissues), implying that the scattering effects of inhomogeneities are more pronounced at higher mechanical frequencies. This is evident from the pronounced increase in the values of 1-Norm for the porcine lumbar muscle tissue at 2000 Hz, before (fig. 36 (a)) and after freezing and thawing (fig. 36 (b)).

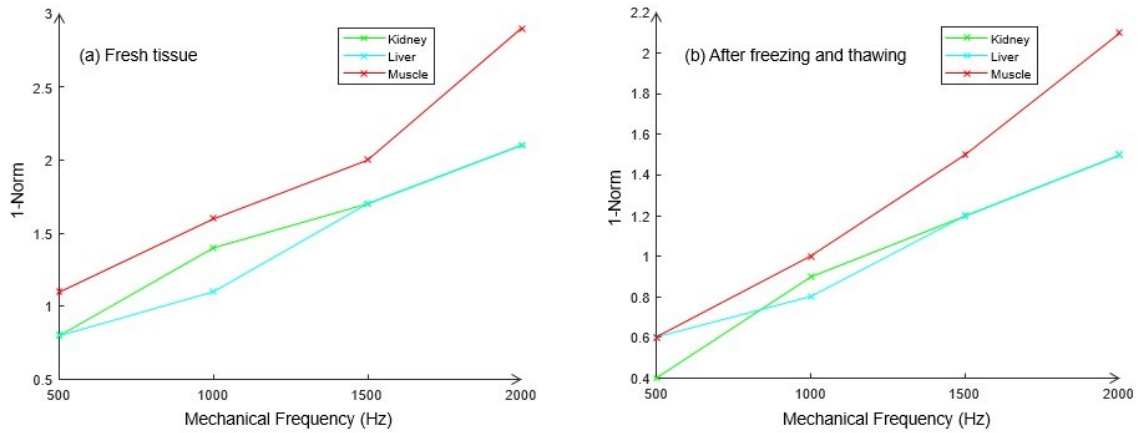


Figure 36. A comparison of group averaged 1-Norm values for ex vivo porcine kidneys (green), porcine liver (cyan) and porcine lumbar muscle (red) (a) in fresh condition and (b) after freezing and thawing.

4.4.4 Correlating mechanical inhomogeneity (1-Norm) with tissue stiffness

This study is a preliminary investigation into the correlation between the tissue microstructure, the resulting tissue mechanical inhomogeneity and the stiffness of the tissue. For the excised biological tissues (porcine kidneys, liver and muscle), there is a direct correlation between the 1-Norm and tissue stiffness. Freezing and thawing led to a reduction in both mechanical inhomogeneity (1-Norm) and stiffness. However, in the case of AD in the mouse brain, this relationship between mechanical inhomogeneity (1-Norm) and brain tissue stiffness becomes inverse. This may be due to a significantly different microstructure of the brain in comparison to kidney/ liver/ muscle, in conjunction with other complex factors in play during AD as explained in section 4.4.2.

4.4.5 Limitation of current study

The present investigation has used three different types of excised tissues with varying degrees of inhomogeneities: namely, porcine kidneys (relatively homogeneous), porcine lumbar muscle

(more inhomogeneous) and excised mouse brain (more inhomogeneous). The investigator has noted a correlation between the degree of inhomogeneity of these biological tissues (using 1-Norm waveform analysis technique) and the stiffness (computed using 2D wave inversion). Pathological examination was not performed on each of the samples to estimate the tissue stiffness before and after the condition of the tissue changed. However, our results are in agreement with prior investigations performed by other research groups which estimated a reduction in stiffness of brain in Alzheimer's disease [82] and a reduction in the stiffness of freeze-thawed rat liver tissue [59].

5. CONCLUSION AND SCOPE FOR FUTURE WORK

5.1 Key achievements of the dissertation

The current work has demonstrated the application and capability of three novel techniques (insonification, percussion and 1-Norm) to be able to aid in the non-invasive diagnosis of diseases and injury using the physics of propagation and scattering of mechanical waves in viscoelastic media. The first two techniques of insonification and percussion are already well established [4]–[6], [16], [17], [33], [43]–[45], [84], [85] and have been successfully applied to both human and porcine subjects. The current dissertation has pioneered the development and experimental validation of a comprehensive subject-based finite element model of mechanical wave motion in healthy human lung parenchyma, and has then extended this model to simulate pathological conditions that lead to geometrical and/ or material property changes in the lung parenchyma. In the future, this comprehensive subject-based computational model can serve as a first step in the non-invasive diagnosis of pulmonary disease and injury. The third technique (1-Norm) is a novel Fourier transformation based method to quantify the degree of mechanical property inhomogeneity of biological tissues, using the physics governing scattering of mechanical waves. Both experimentation and FEA are used to demonstrate the application and validity of this technique, followed by real life applications involving neurodegenerative disease (using excised brains of 5xFAD mouse models with AD) and to analyze the effect of freezing and thawing on the mechanical property inhomogeneity of excised porcine kidneys, livers and muscles.

Chapter 2 details the development and experimental validation of a comprehensive computational model of mechanical wave motion in the human torso using insonification. FEA was used to generate and visualize contour plots of mechanical wave propagation inside healthy and diseased human lung parenchymae. The use of FEA enabled a non-invasive, subject-based assessment and

a quantitative comparison of wave propagation in healthy and diseased lung parenchyma, which can potentially aid in non-invasive diagnosis of pulmonary ailments such as pneumothorax, fibrosis, localized tumors and pneumonia.

Chapter 3 dwelled on the development and formulation of the 1-Norm technique to quantify the scattering effects of inhomogeneities on wave scattering. The technique was first applied to mechanical wave displacement data obtained from MRE experiments on a 3D printed fiber phantom and from finite element analysis of phantoms containing spherical inclusions. Two key findings of this investigation were: (1) at a given mechanical frequency of excitation, the value of 1-Norm increases with a reduction in the spacing between the inhomogeneities; (2) at fixed spacing, the value of 1-Norm increases with an increase in the mechanical frequency of excitation. These two observations imply that the contributions of inhomogeneity become more significant when the spacing between the spherical inclusions decreases, and when the frequency of excitation is higher. The chapter then demonstrated the validity and relevance of the 1-Norm technique through MRE experimentation on excised bovine liver and excised porcine lumbus muscle samples. The investigation reported that at comparable wavelengths, the porcine lumbus muscle sample had a higher magnitude of mechanical inhomogeneity as compared to the bovine liver tissue. This observation made sense: the presence of muscle fibers in the porcine lumbus muscle sample led to a higher degree of mechanical inhomogeneity in comparison to the bovine liver sample. In addition, the values of 1-Norm (obtained from both MRE experiments and from FEA studies) showed a similar trend of increment with an increase in the mechanical frequency of excitation.

Thus, 1-Norm was proven to be capable of identifying and quantifying the extent of mechanical property inhomogeneity of the 3D printed fiber phantom as well as excised biological tissue samples (porcine muscle and bovine liver).

Chapter 4 demonstrated the application of the 1-Norm technique to 2 real life scenarios related to: (1) quantifying the changes in the mechanical property inhomogeneity in three different excised biological tissues (viz., porcine liver, kidneys and muscles) due to freezing and thawing; and (2) quantifying the changes in the mechanical property inhomogeneity of mouse brain of 5xFAD species mouse model due to neurodegenerative disease (AD). Application of the 1-Norm technique revealed a reduction in tissue inhomogeneity (lowering of 1-Norm) and a reduction in tissue stiffness due to freezing and thawing. This result is in agreement with a prior investigation by Schellenberger et al. [59] on a rat liver tissue, which had reported a reduction in the tissue stiffness due to freezing and thawing. Further, when 1-Norm was used to assess the changes in mechanical property inhomogeneity of mouse brain (5xFAD model) due to neurodegenerative disease, the investigation revealed an increase in the brain tissue inhomogeneity (higher values of 1-Norm due to AD) and a reduction in the overall stiffness of the brain, confirming with the findings of an earlier investigation by Majumdar et al which had noted a reduction in the brain stiffness due to AD [58]. Thus, the 1-Norm technique is not only capable of identifying and quantifying the changes in mechanical property inhomogeneity of biological tissues due to disease or injury, but additionally, 1-Norm may be used as an alternative MRE-based biomarker to stiffness, which relies on ill-posed wave inversion.

5.2 Prospects for future research

The current dissertation has developed, analyzed and experimentally validated a comprehensive finite element model of mechanical wave motion in healthy human parenchyma. In the future, this

model can be used to develop non-invasive, subject-based diagnosis techniques to detect the presence of pulmonary disorders such as pneumothorax, fibrosis, tumors and pneumonia. The use of FEA has enabled a unique visualization of cross-sectional images of wave propagation and scattering inside the lung parenchymae; such visualizations are not possible through conventional imaging modalities such as by MRE or by medical examination (using a stethoscope). In the future, such “maps” of mechanical wave propagation could be potentially used in combination with other non-invasive imaging modalities such as Ultrasound or MRI/ MRE, to obtain a better visualization of the tissue condition to aid in an accurate non-invasive diagnosis of disease and injury.

1-Norm has been introduced as a novel wavefront analysis technique which, in the future, can qualify as a diagnostic marker for pathological conditions and injuries that result in heterogeneous stiffness distribution, such as primary sclerosing cholangitis (PSC) [77] and Alzheimer’s disease (AD). Additionally, the 1-Norm technique presents an alternative MRE-based biomarker to stiffness, which relies on ill-posed wave inversion. In the future, more studies, including in vivo investigations on human subjects as well as validation using histopathology are needed to shed light on the capability of 1-Norm in being able to detect microscale changes in mechanical property inhomogenization in biological tissues. From a long-term perspective, 1-Norm may potentially qualify as a diagnostic biomarker for non-invasive detection of pathological conditions such as AD, PSC of the liver as well as in detecting musculoskeletal injuries.

APPENDIX A: Copyright clearance and permission to use all the content from our published journal article on human airway insonification (Chapter 2)

**SPRINGER NATURE LICENSE
TERMS AND CONDITIONS**

Feb 01, 2021

This Agreement between University of Illinois at Chicago -- Harish Palnitkar ("You") and Springer Nature ("Springer Nature") consists of your license details and the terms and conditions provided by Springer Nature and Copyright Clearance Center.

License Number	5000330470090
License date	Feb 01, 2021
Licensed Content Publisher	Springer Nature
Licensed Content Publication	Medical & Biological Engineering & Computing
Licensed Content Title	Sound transmission in human thorax through airway insonification: an experimental and computational study with diagnostic applications
Licensed Content Author	Harish Palnitkar et al
Licensed Content Date	Jul 14, 2020
Type of Use	Thesis/Dissertation
Requestor type	academic/university or research institute
Format	print and electronic
Portion	full article/chapter
Will you be translating?	no
Circulation/distribution	1 - 29
Author of this Springer Nature content	yes
Title	Novel perspectives in non-invasive diagnosis of ailments through analysis of mechanical wave motion
Institution name	University of Illinois at Chicago
Expected presentation date	Feb 2021

Requestor Location	University of Illinois at Chicago 2217 W Taylor St Apt 3r CHICAGO, IL 60612 United States Attn: University of Illinois at Chicago
Total	0.00 USD

APPENDIX B: Comparison of results of insonification experimentation on 3 healthy human subjects versus computational simulation

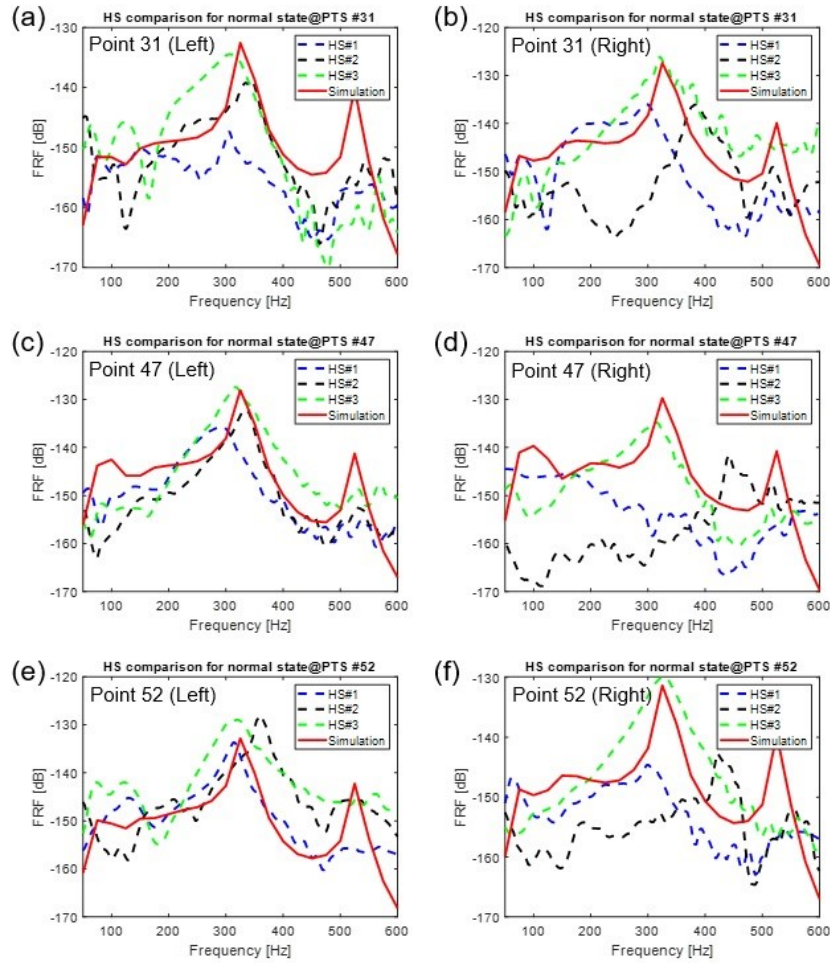


Figure 37. Plot showing the variation of frequency response function (FRF) with mechanical frequency for the three healthy human subjects (dashed curves) versus computational simulation (red curve).

APPENDIX C: Copyright clearance and permission to use all the content from our published journal article on 1-Norm (Chapter 3)



 Home

 Help

 Email Support

 Harish Palnitkar ▾



An investigation into the relationship between inhomogeneity and wave shapes in phantoms and ex vivo skeletal muscle using Magnetic Resonance Elastography and finite element analysis

Author: Harish Palnitkar, Rolf O. Reiter, Shreyan Majumdar, Phillip Lewis, Margaret Hammersley, Ramille N. Shah, Thomas J. Royston, Dieter Klatt

Publication: Journal of the Mechanical Behavior of Biomedical Materials

Publisher: Elsevier

Date: October 2019

Published by Elsevier Ltd.

Journal Author Rights

Please note that, as the author of this Elsevier article, you retain the right to include it in a thesis or dissertation, provided it is not published commercially. Permission is not required, but please ensure that you reference the journal as the original source. For more information on this and on your other retained rights, please visit: <https://www.elsevier.com/about/our-business/policies/copyright#Author-rights>

CITED LITERATURE

- [1] H. Palnitkar *et al.*, “Sound transmission in human thorax through airway insonification: an experimental and computational study with diagnostic applications,” *Med. Biol. Eng. Comput.*, vol. 58, pp. 2239–2258.
- [2] H. Palnitkar *et al.*, “An investigation into the relationship between inhomogeneity and wave shapes in phantoms and ex vivo skeletal muscle using Magnetic Resonance Elastography and finite element analysis,” *J. Mech. Behav. Biomed. Mater.*, vol. 98, pp. 108–120.
- [3] T. K. Yasar, T. J. Royston, and R. L. Magin, “Wideband MR elastography for viscoelasticity model identification,” *Magn. Reson. Med.*, vol. 70, no. 2, pp. 479–489, 2013.
- [4] Y. Peng *et al.*, “Sound transmission in porcine thorax through airway insonification,” *Med. Biol. Eng. Comput.*, vol. 54, no. 4, pp. 675–689, 2016.
- [5] Y. Peng, Z. Dai, H. A. Mansy, R. H. Sandler, R. A. Balk, and T. J. Royston, “Sound transmission in the chest under surface excitation: an experimental and computational study with diagnostic applications,” *Med. Biol. Eng. Comput.*, vol. 52, no. 8, pp. 695–706, Aug. 2014.
- [6] Z. Dai, Y. Peng, B. Henry, H. Mansy, and T. Royston, “A Comprehensive Computational Model of Sound Transmission through the Porcine Lung,” *J. Acoust. Soc. Am.*, Nov. 2014.
- [7] B. Henry and T. J. Royston, “A multiscale analytical model of bronchial airway acoustics,” *J. Acoust. Soc. Am.*, vol. 142, no. 4, p. 1774, 2017.
- [8] D. a Rice, “Sound speed in pulmonary parenchyma,” *J. Appl. Physiol.*, vol. 54, no. 1, pp. 304–8, 1983.
- [9] N. B. Smith and A. Webb, *Introduction to Medical Imaging : Physics, Engineering and Clinical Applications*. 2010.
- [10] K. P. McGee, R. D. Hubmayr, and R. L. Ehman, “MR elastography of the lung with hyperpolarized ^3He ,” *Magn. Reson. Med.*, vol. 59, no. 1, pp. 14–18, 2008.
- [11] B. C. Goss, K. P. McGee, E. C. Ehman, A. Manduca, and R. L. Ehman, “Magnetic resonance elastography of the lung: technical feasibility,” *Magn. Reson. Med.*, vol. 56, no. 5, pp. 1060–6, Nov. 2006.
- [12] Y. K. Mariappan *et al.*, “Magnetic resonance elastography of the lung parenchyma in an in situ porcine model with a noninvasive mechanical driver: Correlation of shear stiffness with trans-respiratory system pressures,” *Magn. Reson. Med.*, vol. 67, no. 1, pp. 210–217, 2012.
- [13] Y. Liu, T. J. Royston, D. Klatt, and E. D. Lewandowski, “Cardiac MR elastography of the mouse: Initial results,” *Magn. Reson. Med.*, vol. 76, no. 6, pp. 1879–1886, 2016.
- [14] A. Romano, M. Scheel, S. Hirsch, J. Braun, and I. Sack, “In vivo waveguide elastography of white matter tracts in the human brain,” *Magn. Reson. Med.*, vol. 68, no. 5, pp. 1410–1422, 2012.
- [15] “Polytec PSV-500 Scanning Vibrometer: full field optical vibration measurement.” [Online]. Available: <https://www.polytec.com/us/vibrometry/products/full-field-vibrometers/psv-500-scanning-vibrometer/>.
- [16] Z. Dai, Y. Peng, H. A. Mansy, R. H. Sandler, and T. J. Royston, “Comparison of Poroviscoelastic Models for Sound and Vibration in the Lungs,” *J. Vib. Acoust.*, vol. 136, no. 5, p. 051012, 2014.

- [17] Z. Dai, Y. Peng, H. A. Mansy, R. H. Sandler, and T. J. Royston, "Experimental and computational studies of sound transmission in a branching airway network embedded in a compliant viscoelastic medium," *J. Sound Vib.*, vol. 339, pp. 215–229, 2015.
- [18] N. U. N. L. of Medicine, "Primary spontaneous pneumothorax," *NIH*, 2018. [Online]. Available: <https://ghr.nlm.nih.gov/condition/primary-spontaneous-pneumothorax>.
- [19] NIH US National Library of Medicine, "Idiopathic pulmonary fibrosis," *NIH*, 2018. [Online]. Available: <https://ghr.nlm.nih.gov/condition/idiopathic-pulmonary-fibrosis#statistics>.
- [20] "Pneumonia fact sheet," *World Health Organization*. [Online]. Available: <http://www.who.int/mediacentre/factsheets/fs331/en/>.
- [21] "Lung cancer fact sheet (American Lung Association)," *American Lung Assoc.*, 2018. [Online]. Available: <https://www.lung.org/lung-health-and-diseases/lung-disease-lookup/lung-cancer/resource-library/lung-cancer-fact-sheet.html>.
- [22] S. Choi *et al.*, "1D network simulations for evaluating regional flow and pressure distributions in healthy and asthmatic human lungs," *J. Appl. Physiol.*, 2019.
- [23] R. H. Habib, R. B. Chalker, B. Suki, and a C. Jackson, "Airway geometry and wall mechanical properties estimated from subglottal input impedance in humans.," *J. Appl. Physiol.*, vol. 77, pp. 441–451, 1994.
- [24] A. C. Jackson, R. H. Habib, B. Suki, S. A. Wood, and W. Mitzner, "Serial distribution of airway diameters from input impedance and computed tomography," *Ann. Biomed. Eng.*, vol. 23, no. 6, pp. 740–749, 1995.
- [25] H. Kitaoka, S. Koc, S. Tetsumoto, S. Koumo, H. Hirata, and T. Kijima, "4D model generator of the human lung, 'Lung4Cer,'" *Conf. Proc. ... Annu. Int. Conf. IEEE Eng. Med. Biol. Soc. IEEE Eng. Med. Biol. Soc. Annu. Conf.*, vol. 2013, pp. 453–456, 2013.
- [26] T. J. Royston, M. B. Ozer, S. Acikgoz, H. A. Mansy, and R. H. Sandler, "Advances in computational modeling of sound propagation in the lungs and torso with diagnostic applications," in *Vibration and Acoustics in Biomedical Applications: Imaging, Characterization and Diagnostics*, New York: ASME Press, 2008, pp. 215–246.
- [27] A. B. Dubois, A. W. Brody, D. H. Lewis, and B. F. Burgess, Jr., "Oscillation mechanics of lungs and chest in man," *J. Appl. Physiol.*, vol. 8, pp. 587–594, 1956.
- [28] M. Schanz, *Wave Propagation in Viscoelastic and Poroelastic Continua: A Boundary Element Approach*, vol. 4. Berlin: Springer, 2001.
- [29] M. H. Tawhai, "CT-based geometry analysis and finite element models of the human and ovine bronchial tree," *J. Appl. Physiol.*, vol. 97, no. 6, pp. 2310–2321, 2004.
- [30] K. Horsfield and G. Cumming, "Morphology of the bronchial tree in man," *Respir. Physiol.*, vol. 26, no. 2, pp. 173–182, 1968.
- [31] H. Kitaoka, "Construction of the Human Lung and Air Flow Analysis," *Forma*, vol. 27, pp. 21–27, 2012.
- [32] B. Henry and T. J. Royston, "A Multiscale Analytical Model of Bronchial Airway Acoustics," *J. Acoust. Soc. Am.*, vol. 142, no. 4, pp. 1774–80, 2017.
- [33] T. J. Royston, X. Zhang, H. A. Mansy, and R. H. Sandler, "Modeling sound transmission through the pulmonary system and chest with application to diagnosis of a collapsed lung," *J. Acoust. Soc.*

- Am.*, vol. 111, no. 4, pp. 1931–46, 2002.
- [34] G. R. Wodicka, K. N. Stevens, H. L. Golup, E. G. Carvalho, and D. C. Shannon, “A Model of Acoustic Transmission in the Respiratory System,” *IEEE Trans. Biomed. Eng.*, vol. 36, no. 9, pp. 925–934, 1989.
 - [35] “The Visible Human Project,” *The US National Library of Medicine*. [Online]. Available: <https://www.nlm.nih.gov/research/visible/animations.html>.
 - [36] T. Hughes, *The Finite Element Method: Linear Static and Dynamic Finite Element Analysis*, First. New Jersey: Prentice-Hall Inc., 2000.
 - [37] H. E. von Gierke, H. L. Oestreicher, E. K. Franke, H. O. Parrack, and W. W. von Wittern, “Physics of Vibrations in Living Tissues,” *J Appl Physiol*, vol. 4, no. 12, pp. 886–900, Jun. 1952.
 - [38] T. J. Royston, Z. Dai, R. Chaunsali, Y. Liu, Y. Peng, and R. L. Magin, “Estimating material viscoelastic properties based on surface wave measurements: a comparison of techniques and modeling assumptions,” *J. Acoust. Soc. Am.*, vol. 130, no. 6, pp. 4126–38, Dec. 2011.
 - [39] E. Garner, R. Lakes, T. Lee, C. Swan, and R. Brand, “Viscoelastic Dissipation in Compact Bone: Implications for Stress-Induced Fluid Flow in Bone,” *J. Biomech. Eng.*, vol. 122, no. 2, p. 166, Apr. 2000.
 - [40] R. S. Lakes, J. L. Katz, and S. S. Sternstein, “Viscoelastic properties of wet cortical bone—I. Torsional and biaxial studies,” *J. Biomech.*, vol. 12, no. 9, pp. 657–678, Jan. 1979.
 - [41] “Lung carcinoid tumor stages: early detection, diagnosis and staging,” *American Cancer Society*, 2018. [Online]. Available: <https://www.cancer.org/cancer/lung-carcinoid-tumor/detection-diagnosis-staging/staging.html>.
 - [42] R. Sinkus, M. Tanter, T. Xydeasc, S. Cathelineb, J. Bercoff, and M. Fink, “Viscoelastic shear properties of in vivo breast lesions measured by MR elastography,” *J. Magn. Reson. Imaging*, vol. 23, pp. 159–165, 2005.
 - [43] H. A. Mansy, T. J. Royston, R. A. Balk, and R. H. Sandler, “Pneumothorax detection using computerised analysis of breath sounds,” *Med. Biol. Eng. Comput.*, vol. 40, no. 5, pp. 526–532, 2002.
 - [44] H. A. Mansy, T. J. Royston, R. A. Balk, and R. H. Sandler, “Pneumothorax detection using pulmonary acoustic transmission measurements,” *Med. Biol. Eng. Comput.*, vol. 40, no. 5, pp. 520–525, 2002.
 - [45] H. A. Mansy *et al.*, “Pneumothorax effects on pulmonary acoustic transmission,” *J. Appl. Physiol.*, vol. 119, no. 3, pp. 250–257, 2015.
 - [46] R. Loomba *et al.*, “Magnetic resonance elastography predicts advanced fibrosis in patients with nonalcoholic fatty liver disease: A prospective study,” *Hepatology*, vol. 60, no. 6, pp. 1920–1928, 2014.
 - [47] R. Muthupillai, P. J. Rossman, D. J. Lomas, J. F. Greenleaf, S. J. Riederer, and R. L. Ehman, “Magnetic resonance imaging of transverse acoustic strain waves,” *Magn. Reson. Med.*, vol. 36, no. 2, pp. 266–274, 1996.
 - [48] D. Klatt *et al.*, “In vivo determination of hepatic stiffness using steady-state free precession magnetic resonance elastography,” *Invest. Radiol.*, vol. 41, no. 12, pp. 841–848, 2006.
 - [49] E. C. Clarke, S. Cheng, M. Green, R. Sinkus, and L. E. Bilston, “Using static preload with

- magnetic resonance elastography to estimate large strain viscoelastic properties of bovine liver,” *J. Biomech.*, vol. 44, no. 13, pp. 2461–2465, 2011.
- [50] D. Klatt, S. Papazoglou, J. Braun, and I. Sack, “Viscoelasticity-based MR elastography of skeletal muscle,” *Phys. Med. Biol.*, vol. 55, no. 21, pp. 6445–6459, 2010.
 - [51] K. Tan, L. Juge, A. Hatt, S. Cheng, and L. E. Bilston, “Measurement of large strain properties in calf muscles in vivo using magnetic resonance elastography and spatial modulation of magnetization,” *NMR Biomed.*, no. February, p. e3925, 2018.
 - [52] A. Arani *et al.*, “Cardiac MR elastography for quantitative assessment of elevated myocardial stiffness in cardiac amyloidosis,” *J. Magn. Reson. Imaging*, vol. 46, no. 5, pp. 1361–1367, 2017.
 - [53] D. Klatt, U. Hamhaber, P. Asbach, J. Braun, and I. Sack, “Noninvasive assessment of the rheological behavior of human organs using multifrequency MR elastography: A study of brain and liver viscoelasticity,” *Phys. Med. Biol.*, vol. 52, no. 24, pp. 7281–7294, 2007.
 - [54] J. L. Schmidt *et al.*, “Measurement of anisotropic mechanical properties in porcine brain white matter ex vivo using magnetic resonance elastography,” *J. Mech. Behav. Biomed. Mater.*, vol. 79, no. December 2017, pp. 30–37, 2018.
 - [55] F. Dittmann *et al.*, “Tomoelastography of the prostate using multifrequency MR elastography and externally placed pressurized-air drivers,” *Magn. Reson. Med.*, vol. 79, no. 3, pp. 1325–1333, 2018.
 - [56] A. Kolipaka, S. Schroeder, X. Mo, Z. Shah, P. A. Hart, and D. L. Conwell, “Magnetic resonance elastography of the pancreas: Measurement reproducibility and relationship with age,” *Magn. Reson. Imaging*, vol. 42, no. 2017, pp. 1–7, 2017.
 - [57] S. Hirsch, J. Braun, and I. Sack, *Magnetic Resonance Elastography: Physical background and Medical applications*, 1st ed. Berlin: Wiley-VCH, 2017.
 - [58] S. Majumdar and D. Klatt, “Longitudinal study of sub- - regional cerebral viscoelastic properties of 5XFAD Alzheimer ’ s disease mice using multifrequency MR elastography,” no. January, pp. 1–10, 2021.
 - [59] Angela Ariza de Schellenberger, Hannah Everwien, and Nils Haep, “Mechanical characterization of rat liver tissue in native, lysed and decellularized states by 0.5 T tabletop magnetic resonance elastography (MRE),” in *Proc Intl Soc Mag Reson Med*, 2018.
 - [60] G. J. Tortora, *Principles of Human Anatomy*, Ninth Edit. New York: John Wiley & Sons, Inc., 2002.
 - [61] M. A. Dresner, G. H. Rose, P. J. Rossman, R. Muthupillai, A. Manduca, and R. L. Ehman, “Magnetic resonance elastography of skeletal muscle,” *J. Magn. Reson. Imaging*, vol. 13, no. 2, pp. 269–276, 2001.
 - [62] S. Papazoglou, J. Rump, J. Braun, and I. Sack, “Shear wave group velocity inversion in MR elastography of human skeletal muscle,” *Magn. Reson. Med.*, vol. 56, no. 3, pp. 489–497, 2006.
 - [63] M. A. Green, G. Geng, E. Qin, R. Sinkus, S. C. Gandevia, and L. E. Bilston, “Measuring anisotropic muscle stiffness properties using elastography,” *NMR Biomed.*, vol. 26, no. 11, pp. 1387–1394, 2013.
 - [64] E. C. Qin *et al.*, “Combining MR elastography and diffusion tensor imaging for the assessment of anisotropic mechanical properties: A phantom study,” *J. Magn. Reson. Imaging*, vol. 37, no. 1, pp.

217–226, 2013.

- [65] R. Muthupillai and R. L. Ehman, *Magnetic resonance elastography*, vol. 2, no. 5. 1996.
- [66] K. F. Graff, *Wave motion in elastic solids*. New York: Dover Publications, 1975.
- [67] T. K. Yasar, T. J. Royston, and R. L. Magin, “Wideband MR elastography for viscoelasticity model identification,” *Magn. Reson. Med.*, vol. 70, no. 2, pp. 479–489, 2013.
- [68] A. Manduca *et al.*, “Magnetic resonance elastography: Non-invasive mapping of tissue elasticity,” *Med. Image Anal.*, vol. 5, no. 4, pp. 237–254, 2001.
- [69] T. E. Oliphant, A. Manduca, R. L. Ehman, and J. F. Greenleaf, “Complex-Valued Stiffness Reconstruction for Magnetic Differential Equation,” *Magn. Reson. Med.*, vol. 45, no. September 2000, pp. 299–310, 2001.
- [70] D. Klatt, T. K. Yasar, T. J. Royston, and R. L. Magin, “Sample interval modulation for the simultaneous acquisition of displacement vector data in magnetic resonance elastography: Theory and application,” *Phys. Med. Biol.*, vol. 58, no. 24, pp. 8663–8675, 2013.
- [71] M. Laronda *et al.*, “A bioprosthetic ovary created using 3D printed microporous scaffolds restores ovarian function in sterilized mice,” *Nat. Commun.*, 2017.
- [72] P. L. Lewis, R. M. Green, and R. N. Shah, “3D-printed gelatin scaffolds of differing pore geometry modulate hepatocyte function and gene expression,” *Acta Biomater.*, vol. 69, pp. 63–70, 2018.
- [73] Y. Liu, T. K. Yasar, and T. J. Royston, “Ultra wideband (0.5-16 kHz) MR elastography for robust shear viscoelasticity model identification,” *Phys. Med. Biol.*, vol. 59, no. 24, pp. 7717–7734, 2014.
- [74] T. J. R. Hughes, *The Finite Element Method: Linear Static and Dynamic Finite Element Analysis*, First edit. New Jersey: Prentice-Hall Inc., 2000.
- [75] D. Ghiglia and M. Pritt, *Two-Dimensional Phase Unwrapping: Theory, Algorithms, and Software*. New York: John Wiley & Sons, Inc., 1998.
- [76] S. Papazoglou, J. Braun, D. Klatt, and I. Sack, “Shear wave diffusion observed by Magnetic Resonance Elastography,” in *New Developments in the Visualization and Processing of Tensor Fields*, D. H. Laidlaw and A. Vilanova, Eds. Berlin: Springer-Verlag, 2012, pp. 157–168.
- [77] S. Pruthi and M. F. Picco, “Primary sclerosing cholangitis,” *Mayo clinic website*, 2019. [Online]. Available: <https://www.mayoclinic.org/diseases-conditions/primary-sclerosing-cholangitis/symptoms-causes/syc-20355797>. [Accessed: 23-Mar-2019].
- [78] S. Mattana, S. Caponi, F. Tamagnini, D. Fioretto, and F. Palombo, “Viscoelasticity of amyloid plaques in transgenic mouse brain studied by Brillouin microspectroscopy and correlative Raman analysis,” *J. Innov. Opt. Health Sci.*, vol. 10, no. 6, 2017.
- [79] H. Oakley *et al.*, “Intraneuronal β -amyloid aggregates, neurodegeneration, and neuron loss in transgenic mice with five familial Alzheimer’s disease mutations: Potential factors in amyloid plaque formation,” *J. Neurosci.*, vol. 26, no. 40, pp. 10129–10140, 2006.
- [80] M. Shabihkhani *et al.*, “The procurement, storage, and quality assurance of frozen blood and tissue biospecimens in pathology, biorepository, and biobank settings,” *Clin. Biochem.*, vol. 47, no. 4–5, pp. 258–266, 2014.
- [81] “Alzheimer’s disease,” *Mayo Foundation for Medical Education and Research*. [Online].

Available: <https://www.mayoclinic.org/diseases-conditions/alzheimers-disease/symptoms-causes/syc-20350447>.

- [82] M. C. Murphy *et al.*, “Decreased brain stiffness in Alzheimer’s disease determined by magnetic resonance elastography,” *J. Magn. Reson. Imaging*, vol. 34, no. 3, pp. 494–498, 2011.
- [83] J. L. Molinuevo *et al.*, “White matter changes in preclinical Alzheimer’s disease: A magnetic resonance imaging-diffusion tensor imaging study on cognitively normal older people with positive amyloid β protein 42 levels,” *Neurobiol. Aging*, vol. 35, no. 12, pp. 2671–2680, 2014.
- [84] Z. Dai, Y. Peng, H. A. Mansy, R. H. Sandler, and T. J. Royston, “Comparison of Poroviscoelastic Models for Sound and Vibration in the Lungs,” *J. Vib. Acoust.*, vol. 136, no. 5, p. 051012, Jan. 2014.
- [85] H. A. Mansy, T. J. Royston, R. A. Balk, and R. H. Sandler, “Pneumothorax detection using computerised analysis of breath sounds,” *Med. Biol. Eng. Comput.*, vol. 40, no. 5, pp. 526–532, Sep. 2002.

VITA

Education

- PhD, Mechanical Engineering, Acoustics & Vibrations Lab, **University of Illinois (Chicago)**. GPA: 3.8/4.0, May 2021.
- Master of Technology, Mechanical Engineering, **Indian Institute of Technology Madras**. CGPA: 8.7/10, June 2011.
- BE (Honors), Mechanical Engineering, **Birla Institute of Technology & Science, Pilani, India**. CGPA: 8.3/10, June 2009.

Research experience

PhD research candidate, Acoustics & Vibration Laboratory (Mechanical Engineering UIC)

Aug 2014 – May 2021

- **Research theme:** Use of mechanical vibrations to induce controlled wave motion in soft biological tissues; use of non-invasive, non-contact techniques to measure and analyze this wave motion to detect and numerically quantify the influence of inhomogeneities on wave scattering phenomenon.
- **Key technologies used in research:** Magnetic Resonance Elastography (MRE); Scanning Laser Doppler Vibrometer (SLDV); Finite Element Analysis (Comsol Multiphysics).
- **Research approach**
 - Use of **Magnetic Resonance Elastography (MRE)** to induce and measure the propagation of shear waves inside excised biological tissues. Developed a novel technique (called 1-Norm) to numerically quantify the magnitude of scattering of shear waves in 3D printed anisotropic phantoms and in excised biological tissues such as mouse brain (**Alzheimer's disease**), porcine lumbus muscle, porcine kidney and **human liver (in vivo)**.
 - Use of Scanning Laser Doppler Vibrometer (SLDV) to perform noninvasive measurements of surface waves traveling on the torso (posterior) of healthy human subjects to generate “maps” of breathing patterns of humans having a healthy pulmonary system.
 - Computational modeling (finite element analysis) of sound propagation and mechanical wave motion in healthy human and porcine lung parenchymae. The aim was to develop a novel non-invasive technique based on mechanical wave motion, to diagnose pulmonary pathologies such as pneumonia, fibrosis, pneumothorax and localized tumor.
- **Future work:** Extend the 1-Norm technique to in vivo applications (on human liver) in order to demonstrate the clinical relevance and feasibility of use on human organs.
- **Skills acquired:** 1. Experience with end-to-end design and implementation of MRE experiments on Agilent 9.4 T, Bruker 11.7 T and Table Top (0.5 T) MRI scanners, image reconstruction and analysis of the resulting shear wave displacements to investigate the effect of inhomogeneities on the scattering of mechanical waves in biological tissues. 2. Finite Element Analysis of mechanical wave motion in human lung parenchyma through development of subject specific computational models.
- **Long term research objective:** To develop 1-Norm as a biomarker to aid in non-invasive, subject-specific, detection and staging of disease and injury in human organs.

Master's thesis at Indian Institute of Technology Madras

Aug 2010 – May 2011

- Computational Modeling (FEA) & Structural Analysis of Automobile Gearbox to identify the root cause of noise & vibration.
- Investigating the influence of Fluid-Structure Interaction on noise propagation. Implementing passive noise control measures.

Work Experience (3 years)

Engineer/Technologist, General Electric (Renewables), Bangalore, India.

Oct 2013 – Jun 2014

- Computational Modeling (Structural Analysis) of Wind Turbine Main Gearbox to enable a quieter wind turbine operation.
- Component ownership, design and Product Lifecycle Management (PLM - Enova) of Wind Turbine Main Gearbox Oil Bag.

Engineer (Edison Engineering Development Program), GE Energy, India. Jun 2011 – Oct 2013

- Rotational assignments aimed at design and structural analysis of GE gas turbine components (turbine blades, shrouds, nozzles).
- FE modeling, pre- and post-processing, interpreting and presenting results to the Chief Engineer.
- Contributed in identifying novel avenues for cost savings by material change and life cycle enhancement of Gas turbine components.
- Development of communication and leadership skills through intensive training, workshops and interaction with GE leadership.

Teaching and Mentoring Experience at UIC and IIT Madras

- Led a team of Teaching Assistants to redesign “Computer Aided Design” (ME 347) to emphasize real life applications of CAD.
- Mentored 2 PhD and 2 MS students. Taught wave theory, computational modeling and MRI experimentation techniques.

Recent Publications

1. **Palnitkar, H.**, et al. *An investigation into the relationship between inhomogeneity and wave shapes in phantoms and ex-vivo skeletal muscle using Magnetic Resonance Elastography and Finite Element Analysis*. JMBBM. DOI: 10.1016/j.jmbbm.2019.06.007.
2. **Palnitkar, H.**, et al. *Sound transmission in human thorax through airway insonification: an experimental and computational study with diagnostic applications*. Medical and Biological Engineering and Computing (Springer). DOI: 10.1007/s11517-020-02211-y.
3. **Palnitkar, H.**, et al. *I-Norm: A novel non-invasive tool to quantify the effect of freezing and thawing on excised muscles and quantify the effect of Alzheimer’s Disease on brain inhomogeneity in Murine Subjects*. Manuscript under preparation (Feb. 2021).

International conferences

1. **Palnitkar, H.**, et al. *An investigation of the relationship between fiber dimensions and wave shapes of an anisotropic fiber phantom: preliminary results*. 1st International Workshop on MRE, Charité Universitätsmedizin Berlin. Nov. 2017.
2. **Palnitkar, H.**, et al. *An investigation of the relationship between fiber spacing and shapes of mechanical shear waves in composite anisotropic phantoms*. The 18th US National Congress for Theoretical and Applied Mechanics, Chicago, June 2018.
3. **Palnitkar, H.**, et al. *An investigation of the relationship between wave shapes and spacing between inhomogeneities in viscoelastic tissue-like phantoms*. Sixteenth International Tissue Elasticity Conference (ITEC), Avignon, France. Sep. 2018.
4. **Palnitkar H.**, et al. *I-Norm: A novel image processing technique to investigate the influence of inhomogeneities on the scattering of mechanical waves in soft biological tissues*. IEEE-EMBS Conference on Biomedical and Health Informatics. Chicago, May 2019.
5. Reiter, R., **Palnitkar, H.**, et al. *Tabletop MR Elastography (MRE): Preliminary Results towards an Assessment of Frozen Tissue Bank Samples*. Presented at International Society of Magnetic Resonance in Medicine 2019.
6. **Palnitkar, H.**, Klatt, D., and Royston, T. J. *I-Norm: quantifying mechanical wave scattering phenomenon*. Poster presentation at ASME International Mechanical Engineering Congress and Exposition (IMECE) at Salt Lake City, Utah. November 2019.
7. Royston, T. J., **Palnitkar, H.**, et al. *I-Norm: an investigation of mechanical wave propagation in ex vivo porcine kidney*. Presented at the Virtual Technical Meeting of the Society of Engineering Science, Oct. 2020.
8. **Palnitkar, H.**, et al. *I-Norm: Analyzing Changes in Mechanical Wave Motion in Soft Biological Tissue Caused by a Freeze and Thaw Cycle*. Poster presentation at the virtual ASME International Mechanical Engineering Congress and Exposition, Nov. 2020.

Awards and Recognition

- ASME Travel Award (USD 1000) and Best Computational Approach Award at IMECE, Salt Lake City, Utah. Nov. 2019.

- Faydor Litvin Graduate Honor Award for Excellence in Academics at University of Illinois at Chicago. Aug. 2014.
- “Clear presentation, Attention to Details” Award, Chief Engineer (GE Hot Gas Path Team), Detailed Design Review. Jun. 2012.
- Won the Eng@GE (Engineering at GE) Workshop Challenge of Robot Design & Programming, GE India. Jan. 2013.
- Among the Top 4 prize winners at the UIC 3MT (Three Minute Thesis) Competition. Mar 2019.

Skills

- **Experimentation Skills:** Magnetic Resonance Imaging (MRI and MRE); Scanning Laser Doppler Vibrometry; Vibratory response of elastic and viscoelastic materials subjected to harmonic excitation.
- **Analysis skills:** Multi-body Dynamics, Modal Analysis, Fluid-Structure Interaction, Thermal & Fatigue Analysis, Product Design.
- **FEA Software:** Comsol Multiphysics (Pressure Acoustics; Solid Mechanics); Ansys Workbench; Fluent; Gambit.
- **Programming:** Matlab and C. **CAD:** Pro-E, Solidworks. **PLM Tool:** ENOVIA.

Graduate Level Course Work

- Acoustics in Bioengineering; Biomedical Imaging; Elastography; Vibration, Acoustics, Noise Control; FEA; Rotor Dynamics.